LBNL-44779

ERNEST ORLANDO LAWRENCE
BERKELEY NATIONAL LABORATORY

Plasma-Based Accelerator Structures

Carl B. Schroeder

Accelerator and Fusion Research Division

December 1999

Ph.D. Thesis

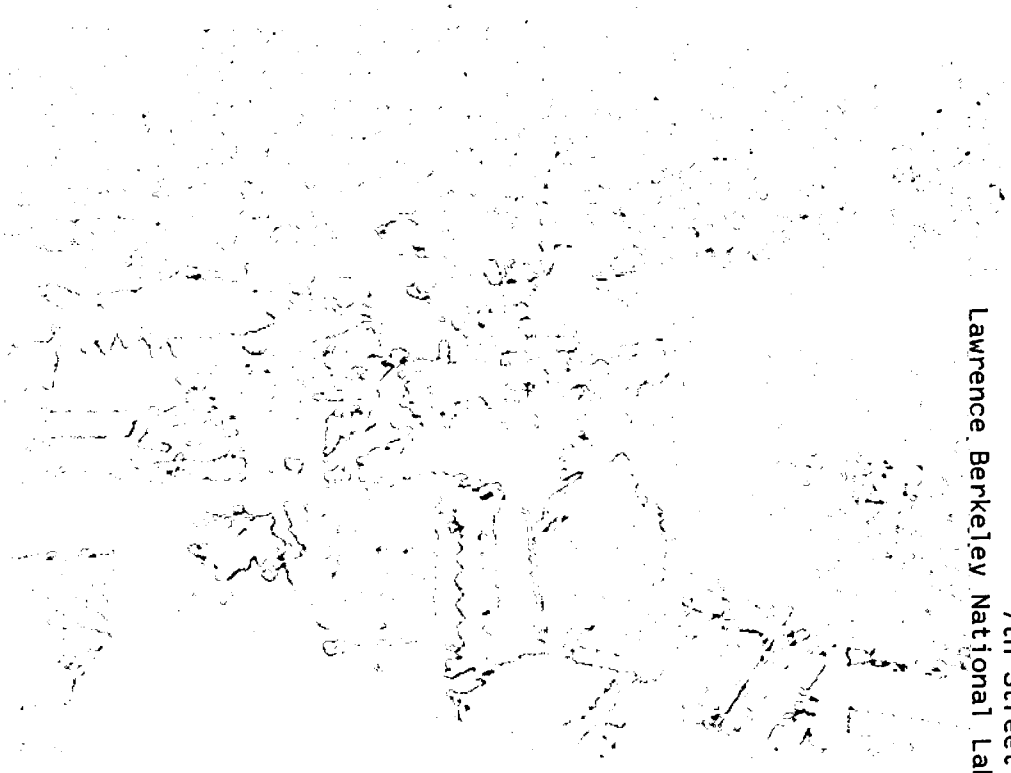

DISCLAIMER

LBNL-44779
CBP Note-328

Plasma-Based Accelerator Structures*

Carl B. Schroeder

Department of Physics
University of California
Berkeley, California 94720

and

Accelerator and Fusion Research Division
Lawrence Berkeley National Laboratory
University of California
Berkeley, California 94720

Ph.D. Thesis

December 1999

* This work was supported by the Director, Office of Science, Office of High Energy and Nuclear Physics, High Energy Physics Division, of the U. S. Department of Energy, under Contract No. DE-AC03-76SF00098.

Plasma-Based Accelerator Structures

by

Carl B. Schroeder

Abstract

Plasma-Based Accelerating Structures

by

Carl Bernhardt Schroeder

Doctor of Philosophy in Physics

University of California at Berkeley

Professor Jonathan S. Wurtele, Chair

Plasma-based accelerators have the ability to sustain extremely large accelerating gradients, with possible high-energy physics applications. This dissertation further develops the theory of plasma-based accelerators by addressing three topics: the performance of a hollow plasma channel as an accelerating structure, the generation of ultrashort electron bunches, and the propagation of laser pulses in underdense plasmas.

The excitation of plasma waves in a hollow plasma channel by a laser pulse or relativistic charged particle beam is analyzed. The mode frequencies and loss factors of the excited channel modes are calculated. The effects of non-ideal hollow plasma channels are discussed. Particle beam stability in a hollow plasma channel is examined. The dipole wakefield couples to the transverse displacement of the particle beam, which results in beam breakup. Single-bunch beam breakup growth lengths are derived for particle beam propagation in the weak-focusing and strong-focusing regimes. The effects of longitudinal wakefields on the beam energy spread is examined. Multi-bunch beam breakup is discussed and methods for reducing beam breakup are proposed and evaluated.

The production of ultrashort electron bunches by dephasing and trapping

background plasma electrons undergoing fluid oscillations in a plasma wave is studied. The plasma electrons are dephased by colliding two counter-propagating laser pulses which generate a slow phase velocity beat wave. The threshold laser pulse amplitudes, the optimal injection phase for trapping, and the trapping volume are calculated. The dynamics and quality of the generated electron bunches are examined. The analysis indicates that this optical injection scheme has the capability to produce relativistic femtosecond electron bunches with fractional energy spread of a few percent and normalized transverse emittance less than 1 mm mrad using 1 terawatt injection laser pulses.

The propagation of ultrashort high-power laser pulses in underdense plasmas is studied. Envelope equations are derived for optical beam parameters which include finite-radius and finite pulse length effects. Solutions of the envelope equations are presented for an adiabatic plasma response. For the general non-adiabatic plasma response, laser-plasma instabilities are examined and asymptotic instability growth rates are derived.

To my parents, Lothar and Marianne Schroeder,

my brother, Lothar, and my sister, Juliann.

Contents

List of Figures

List of Tables

Acknowledgements

The support of my many colleagues, family, and friends throughout my graduate career has been invaluable. There are many people who assisted me and positively influenced my life during this time who are not listed here, but I thank them none the less.

My great thanks go to Jonathan S. Wurtele, my research advisor, for training me to be a physicist. I am particularly indebted to him for being both a critical and encouraging supervisor, and for providing the environment for me to work on many interesting and diverse problems.

I wish to thank Wim P. Leemans for working with a graduate student theorist in his laboratory at the Center for Beam Physics, LBNL, and for always listening and taking seriously my ideas. I am particularly indebted to him for proposing the problem of optical beam injection, which inspired the work presented in Chapter 4.

I would like to express my thanks to Eric Esarey for introducing me to many interesting problems of laser-plasma interactions, and for many delightful months of physics. His ideas greatly influenced the work on laser propagation presented in Chapter 5.

I would like to thank David H. Whittum for our many all-day discussions of beam-plasma physics, and for his hospitality during my frequent visits to the Stanford Linear Accelerator Center.

I owe my appreciation to Roger W. Falcone and Michael A. Lieberman for taking the time to be on my committee and for reading this dissertation.

I wish to thank Allan N. Kaufman for teaching me the fundamental aspects of theoretical plasma physics and for taking the time to be on my qualifying examination committee.

I would like to thank Tom Katsouleas for all his hospitality during my stay at the University of Southern California and during my visit to Kardamyli, Greece.

I thank Peter Byung Lee, Paul Volfbeyn, and Brad Shadwick for many

enlightening discussions about physics and life.

I am grateful to Chaun S. Liu and Adil Hassam for introducing me to plasma physics when I was an undergraduate student in College Park, Maryland.

I would like to acknowledge all the administrative assistance provided by Anne Takizawa and Donna Sakima of the Berkeley Physics Department, and Olivia Wong and Joy Kono at the Center for Beam Physics.

My life in graduate school would have been much poorer without the company of my friends and fellow graduate students. I especially wish to thank Dan Durkin and Erik Gilson of Project Mellon.

I wish to express my gratitude to Sarah E. Houghtaling for all her encouragement during the writing of this dissertation.

The greatest debt I owe to my family for all the support they have given me throughout the many years of graduate school and for everything they have done for me before.

Chapter 1

Introduction

The reach of high-energy physics is limited by its instruments, accelerators, which are currently passive conducting structures attaining large accelerating fields by resonant excitation. At present, testing of new theories in high-energy physics requires the development of particle accelerators capable of producing particle beams with multi-TeV energies. In conventional accelerators based on radio-frequency technology, the size of the accelerating fields is limited by breakdown of the structure media. Breakdown occurs when the electric field is sufficiently large to allow emission of electrons from the walls of the accelerator cavity. Breakdown limits the maximum accelerating gradient of conventional accelerating structures to less than roughly 100 MV/m. In order to achieve TeV-energy particle beams in future colliders, without making the machine prohibitively large in size, a large accelerating gradient beyond what is achievable in conventional accelerating structures is required. Plasma-based accelerators are not limited by electrical breakdown. For two decades, the use of plasma as an accelerating medium has been investigated for the next generation of accelerators [1, 2, 3].

The basic idea behind plasma-based accelerators is to excite a longitudinal wave in a plasma with phase velocity near the speed of light. Injected charged particles can then gain energy from the large longitudinal electric field of the plasma

wave. The availability of radiation sources allows one to consider the excitation of plasma waves by a laser pulse. The plasma can act as a transformer, generating a large longitudinal electric field for acceleration from the large transverse field of a laser pulse.

In this chapter, an overview of the basic plasma-based accelerator concepts is presented. The mechanisms for plasma wave generation are reviewed, and the limitations of such accelerators are discussed. This will provide the motivation for the subsequent chapters and the theoretical work presented in this dissertation.

1.1 Overview of Plasma-Based Accelerator Concepts

The use of plasma as an accelerating medium requires the generation of an intense longitudinal plasma oscillation with phase velocity near the speed of light. Several schemes have been proposed for generating intense plasma waves for acceleration purposes. At present, the laser wakefield accelerator (LWFA), the plasma beat wave accelerator (PBWA), the self-modulated laser wakefield accelerator (SM-LWFA), and the plasma wakefield accelerator (PWFA) are the most widely investigated methods of plasma wave generation.

The LWFA excitation method, first proposed by Tajima and Dawson in 1979 [4], uses a single extremely intense ($\gtrsim 10^{18}$ W/cm^2) short (on the order of a plasma period, e.g., $\lesssim 1$ ps) laser pulse which travels through an underdense plasma ($\omega_p^2/\omega^2 \ll 1$, where ω_p is the plasma frequency and ω the laser frequency). The ponderomotive force (radiation pressure) associated with the laser pulse envelope expels electrons from the region of the laser pulse. If the laser pulse length is of order the plasma wavelength, the ponderomotive force of the laser will excite a large amplitude plasma wave with phase velocity v_φ approximately equal to the group velocity of the laser pulse $v_g \simeq c(1-\omega_p^2/\omega^2)^{1/2}$, which is near the speed of light for an underdense plasma. The LWFA plasma wave excitation mechanism is illustrated in Fig. 1.1. Recently, the measurement of plasma wave generation in a LWFA was

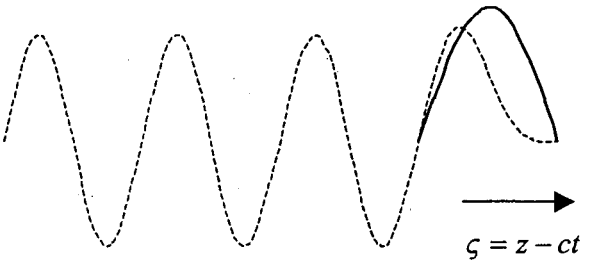

Figure 1.1: Schematic of LWFA (or PWFA), in which a short laser pulse (or charged particle beam) drives a plasma wave (dotted curve).

reported by researchers at Ecole Polytechnique [5], as well as acceleration of injected electrons [6].

The availability of compact terawatt laser systems, which has made it possible to produce the high-intensity short-duration laser pulses needed for experimental studies of the LWFA, was due to the development of chirped-pulse amplification (CPA) [7]. The technique of CPA, first demonstrated in 1988 [8], allows the generation of ultra-intense ($\gtrsim 10^{18}$ W/cm^2) subpicosecond laser pulses. In CPA, a low-energy (e.g., $\sim$ mJ) ultrashort pulse is temporally stretched by a pair of gratings. The stretched pulse is amplified and then recompressed by a second pair of matched gratings. The chirped long-duration pulse avoids undesirable high-field effects, such as nonlinear modification of the index of refraction (which can lead to self-focusing in the amplifying medium). The stretched pulse can therefore reach high energies (up to kJ) in the solid-state amplifiers. CPA can efficiently amplify subpicosecond pulses in solid-state media (e.g., ND:glass and Ti:sapphire) and has enabled laser systems to reach petawatt powers [9]. Multi-terawatt laser systems are now available in many laboratories.

The PBWA was proposed as an alternative to the LWFA and first studied experimentally for plasma wave excitation because the laser technology capable of producing high-intensity ultrashort pulses was not available in the early 1980's. In

the PBWA, two long pulse length, co-propagating lasers beams of frequencies ω_1 and ω_2 are focused in a plasma. The lasers beat against each other with a beat frequency close to the plasma frequency $\omega_p \simeq \omega_1 - \omega_2$, thereby resonantly driving a plasma wave. The phase velocity of the plasma wave $v_\varphi \approx 1 - \omega_p^2/(2\omega_1\omega_2)$ is approximately equal to the group velocity of the incident lasers in the limits $\omega_p^2/\omega_1^2 \ll 1$ and $\omega_p^2/\omega_2^2 \ll 1$. The ability of laser pulses to excite plasma waves with high gradients and with phase velocities near the speed of light was first shown in PBWA experiments by Clayton *et. al.* [10]. Subsequent PBWA experiments have observed acceleration of electrons from the background plasma [11] and injected into the plasma wave [12, 13]. There are several disadvantages of the PBWA excitation mechanism. The requirement of uniformity imposed on the plasma density in order to satisfy the resonance condition is difficult to achieve experimentally. Another disadvantage is saturation of the plasma wave amplitude. As the plasma wave grows, nonlinear effects will cause resonant detuning of the plasma wave from the beat wave leading to saturation and limiting the amplitude of the plasma wave [14].

The SM-LWFA relies on a laser-plasma instability to excite plasma waves. The SM-LWFA uses a high-intensity laser pulse propagating through a high-density plasma such that the laser pulse length is long compared to the plasma wavelength. The laser power is typically somewhat larger than the critical power for relativistic self-focusing $P > P_{\rm crit} \simeq 17(\omega/\omega_p)^2$ GW such that the laser can modify the index of refraction of the plasma to overcome diffraction [15]. In this high-density plasma regime, the laser pulse undergoes a self-modulation instability which causes the pulse to become axially modulated at the plasma period. The modulated laser pulse produces a large amplitude resonantly-driven plasma wave. Evidence of plasma wave generation in the high-density self-modulated regime was first detected by Coverdale *et. al.* [16]. The trapping and acceleration of electrons from the background plasma has also been demonstrated experimentally in SM-LWFA experiments at several laboratories [17, 18, 19, 20]. Accelerating gradients as large as 100 GV/m have been produced at the Rutherford Appleton Laboratory in the self-modulated regime [18].

	I [W/cm^2]	τ_L [ps]	λ [μm]	n_0 [cm^3]	$\Delta\gamma$ [MeV]	E_z [GV/m]
LWFA:						
KEK (Japan) [23]	10^{17}	1.0	1.05	10^{15}	5	0.7
LULI (France) [6]	4×10^{17}	0.4	1.05	2×10^{16}	1.6	1.5
PBWA:						
ILE (Japan) [11]	10^{13}	1000	9.6, 10.6	10^{17}	10	1.5
UCLA (USA) [12]	10^{14}	300	10.3, 10.6	10^{16}	28	2.8
LULI (France) [13]	10^{17}	90	1.05, 1.06	10^{17}	1.4	0.6
SM-LWFA:						
LLNL (USA) [16]	10^{18}	0.6	1.05	10^{19}	2	-
KEK (Japan) [17]	10^{17}	1.0	1.05	10^{19}	17	30
RAL (UK) [18]	10^{19}	0.8	1.05	10^{19}	44	100
CUOS (USA) [19]	4×10^{18}	0.4	1.05	3.6×10^{19}	> 1	-
NRL (USA) [20]	5×10^{18}	0.4	1.05	1.4×10^{19}	> 1	-

Table 1.1: Parameters and results for laser-driven plasma-based accelerator experiments. The laser intensity I, laser pulse duration τ_L, laser wavelength λ, plasma density n_0, energy gain of the accelerated particles $\Delta\gamma$, and accelerating gradient E_z are listed for each experiment.

Although the SM-LWFA has the advantage of enhanced accelerating gradients resulting from operation at higher plasma densities, it is subject to various instabilities (e.g., Raman scattering [21] and hose-modulation instability [22]) owing to the long laser pulse length. In addition, relativistic self-focusing will not be effective in the leading portion of the long-duration laser pulse due to the finite response time of the plasma, which is of the order of the plasma period $\sim \omega_p^{-1}$. This leads to erosion and diffraction of the leading edge of the laser pulse which will limit the acceleration length and therefore the energy gain of accelerated particles.

Table 1.1 summarizes the parameters and results for laser-driven plasma-based accelerator experiments. The laser pulse length used in the LWFA is short, and therefore laser-plasma instabilities detrimental to the propagation of long pulses (e.g., SM-LWFA) will be reduced. In addition, since the LWFA does not excite the

	γ_{drive} [MeV]	q_{drive} [nC]	$c\tau_b$ [mm]	n_0 [cm^{-3}]	$\Delta\gamma$ [MeV]	E_z [MV/m]
ANL (USA) [25]	21	4.0	2.1	10^{12}	0.2	5.0
KEK (Japan) [26]	500	10	3.0	10^{12}	30	30
KhFTI (Ukraine) [27]	2	0.4	17	10^{11}	0.5	0.25
SLAC (USA) [31]	3×10^4	3.2	0.6	10^{15}	-	-

Table 1.2: Parameters and results for beam-driven plasma-based accelerator experiments. The drive beam energy γ_{drive}, drive beam charge q_{drive}, drive beam length $c\tau_b$, plasma density n_0, energy gain of the accelerated particles $\Delta\gamma$, and accelerating field E_z are listed for each experiment.

plasma wave resonantly, it does not require the stringent tolerances on plasma non-uniformity, nor does it suffer from saturation, as in the PBWA. Therefore the LWFA is considered the most promising laser-driven plasma-based accelerator scheme.

Plasma-based accelerators in which the plasma wave is driven by charged particle beams are referred to as plasma wakefield accelerators. In the PWFA, the space-charge forces associated with a relativistic electron beam will displace plasma electrons and excite a plasma wave provided the beam terminates in a time shorter than the plasma period. PWFA experiments have been carried out demonstrating plasma wave generation and electron acceleration [24, 25, 26, 27]. Beam-driven plasma-based accelerator experiments are summarized in Table 1.2. In the PWFA, primary drive beam propagation through the plasma is of particular importance. Electron drive beams are subject to the two-stream instability [28] and the electron-hose instability [29]. Energy gain in the linear regime of the PWFA is also limited by the transformer ratio [30], which describes the self-induced decelerating field experienced by the drive beam as it propagates through the plasma.

1.1.1 Basic Equations for Plasma Wave Generation

This section describes the basic equations which model plasma wave generation. It is convenient to model the plasma as a fluid by taking moments of the Vlasov equation [32]. For a cold collisionless fluid, the electron plasma current is $\vec{J}_{\rm p} = -en_e c\vec{u}/\gamma$, where $-e$ is the electron charge and c is the speed of light. The electron plasma number density n_e and electron fluid momentum $m_e c\vec{u}$, where m_e is the electron rest mass, satisfy the continuity equation

$$\frac{\partial n_e}{\partial t} + c\nabla \cdot \left(n_e \frac{\vec{u}}{\gamma} \right) = 0 \tag{1.1}$$

and the fluid momentum equation

$$\left(\frac{\partial}{\partial t} + \frac{1}{\gamma}\vec{u} \cdot c\nabla \right) \vec{u} = c\nabla\phi + \frac{\partial \vec{a}}{\partial t} - \frac{1}{\gamma}\vec{u} \times (c\nabla \times \vec{a}) \ , \tag{1.2}$$

where $\gamma = (1+u^2)^{1/2}$ is the relativistic factor. Here $\phi = e\Phi/(m_e c^2)$ and $\vec{a} = e\vec{A}/(m_e c^2)$ are the normalized scalar Φ and vector $\vec{A}$ potentials of the electromagnetic fields in the plasma. Equation (1.2) can be rewritten as

$$\left(\frac{\partial}{\partial t} - \frac{1}{\gamma}\vec{u} \times c\nabla \times \right) (\vec{u} - \vec{a}) = c\nabla \left(\phi - \gamma \right) \ , \tag{1.3}$$

where the first term on the right-hand side represents the space-charge force $F_{\rm sc} = -m_e c^2 \nabla\phi$, and the second term is the generalized ponderomotive force

$$F_{\rm pm} = -m_e c^2 \nabla\gamma \ . \tag{1.4}$$

The electric E and magnetic B fields in the plasma can be represented by the vector and scalar potentials: $\vec{E} = -\nabla\Phi - c^{-1}\partial_t \vec{A}$ and $\vec{B} = \nabla \times \vec{A}$. In the Coulomb gauge $\nabla \cdot \vec{A} = 0$, the Maxwell equations [33] can be combined to yield

$$\left(c^2\nabla^2 - \frac{\partial^2}{\partial t^2} \right) \vec{a} = \omega_p^2 \frac{n_e}{n_0}\frac{\vec{u}}{\gamma} + \omega_p^2 \frac{n_b}{n_0}\frac{\vec{v}_b}{c} + \frac{\partial}{\partial t} c\nabla\phi \ , \tag{1.5}$$

$$c^2\nabla^2\phi = \omega_p^2 \left(\frac{n_e}{n_0} - 1 + \frac{n_b}{n_0} \right) \ , \tag{1.6}$$

where n_0 is the equilibrium number density of the plasma and $\omega_p = (4\pi e^2 n_0/m_e)^{1/2}$ is the plasma frequency. In Eqs. (1.5) and (1.6), the effects of an external electron beam with density n_b and velocity $\vec{v}_b$ are included.

Throughout this work, it is assumed that the ions remain stationary, since the ion response time [i.e., $\sim \omega_{pi}^{-1} = (4\pi e^2 n_i/M_i)^{-1/2}$, where M_i is the mass of the ions and n_i is the number density of the ions] is typically much greater than the driver duration. In addition, collisions and thermal effects are neglected throughout this work since the collision time is typically much greater than the driver duration, and the thermal velocity is typically much less than the quiver velocity of an electron in the fields.

For a laser pulse driver ($\vec{a} \neq 0$ and $n_b = 0$) propagating in an initially homogeneous plasma $\nabla n_0 = 0$, Eqs. (1.1), (1.2), (1.5), and (1.6) can be solved in the linear regime $a^2 \ll 1$ by a perturbation expansion of the fluid quantities in powers of the normalized vector potential of the laser field (i.e., $f = \sum f_n$, where f is any fluid quantity and $f_n \sim a^n$). The zeroth-order equations describe the equilibrium plasma: $n_e = n_0$, $\gamma_0 = 1$, and $\phi_0 = \vec{u}_0 = 0$. The first-order response of the plasma is the electron quiver motion in the laser field: $\vec{u}_1 = \vec{a}$ and $n_1 = \phi_1 = \gamma_1 = 0$. To second-order, Eqs. (1.1), (1.2) and (1.6) can be combined to yield

$$\left(\frac{\partial^2}{\partial t^2} + \omega_p^2\right)\frac{n_2}{n_o} = c^2\nabla^2\frac{a^2}{2} . \tag{1.7}$$

The right-hand side of Eq. (1.7) represents the second-order ponderomotive force of the laser pulse $F_{\rm pm} \simeq -m_e c^2 \nabla a^2/2$. The electric field generated by the second-order density perturbation given by Eq. (1.7) is

$$\vec{E}(\vec{r},t) = -\frac{m_e c^2}{e}\omega_p \int_0^t dt_1 \sin\left[\omega_p(t-t_1)\right]\frac{1}{2}\nabla a^2(\vec{r},t_1) . \tag{1.8}$$

Equation (1.8) implies that plasma waves are generated at the plasma frequency, and that the radial extent of the plasma wave is of order the transverse size of the laser (e.g., the laser spot size).

For the PWFA ($\vec{a} = 0$ and $n_b \neq 0$), Eqs. (1.1), (1.2) and (1.6) can be combined in the linear regime $n_b \ll n_0$, assuming an initially homogeneous plasma, to yield

$$\left(\frac{\partial^2}{\partial t^2} + \omega_p^2\right)\frac{n_2}{n_0} = -\omega_p^2\frac{n_b}{n_0} . \tag{1.9}$$

Equation (1.9) describes plasma wave generation by the space-charge forces of an electron beam. Assuming an ultra-relativistic $|\vec{v}_b| \simeq c$ azimuthally-symmetric drive beam, the axial electric field of the plasma wave behind the drive beam is [34]

$$E_z(r,\zeta) = \frac{4\pi e}{c^2}\omega_p^2 \int_\infty^\zeta d\zeta_1 \int_0^\infty dr_1 r_1 \cos\left[\frac{\omega_p}{c}(\zeta - \zeta_1)\right] I_0\left(\frac{\omega_p}{c}r_<\right) K_0\left(\frac{\omega_p}{c}r_>\right) n_b(\zeta_1, r_1) , \tag{1.10}$$

where $\zeta = z - ct$, I_0 and K_0 are the zeroth-order modified Bessel functions of the second kind, and $r_<$ and $r_>$ denote the smaller and larger of r and r_1 respectively. For the PWFA, plasma waves are generated at the plasma frequency and the radial extent is approximately given by the larger of the beam radius and the plasma skin depth c/ω_p.

From Eqs. (1.8) and (1.10), one can see that the accelerating gradient generated by the plasma wave will be of the order

$$E_z \simeq \left(\frac{cm_e\omega_p}{e}\right)\frac{n_2}{n_0} \simeq 96\text{V/m}\left(\frac{n_2}{n_0}\right) n_0^{1/2}(\text{cm}^{-3}) . \tag{1.11}$$

This field can be enormous compared to accelerating gradients found in conventional accelerators. For example, if a 10% plasma density perturbation is excited ($n_2/n_0 \simeq 0.1$) in a plasma with density $n_0 = 10^{18}$ cm^{-3}, then $E_z \simeq 10$ GV/m. This field is two orders of magnitude larger than what is achievable in conventional accelerators.

1.1.2 Limitations of Plasma-Based Accelerators

There are a number of mechanisms which limit the interaction length, and therefore the final energy of accelerated particles, that can be achieved using laser-plasma acceleration schemes. One such limitation is laser diffraction. In vacuum,

a laser undergoes Rayleigh diffraction [35] and the spot size evolves as $r_s = r_0[1 + (z/Z_R)^2]^{1/2}$, where r_0 is the laser spot size at focus and $Z_R = \pi r_0^2/\lambda$ is the Rayleigh length. Therefore, without some form of optical guiding, the laser-plasma interaction distance will be limited to a few Rayleigh lengths.

Another limit on the acceleration length comes from dephasing. Since the phase velocity of the excited plasma wave is somewhat smaller than the speed of light, velocity mismatch between the plasma wave and the accelerated particles will cause slippage, and the particles will eventually move out of phase with respect to the accelerating field of the plasma wave. Assuming the accelerating particles are moving with speed c and the phase velocity of the plasma wave is equal to the group velocity of the laser pulse, $v_\varphi \simeq v_g \simeq 1 - \omega_p^2/(2\omega^2)$, the distance for the particle to slip π in phase (i.e., to slip from an accelerating region to a decelerating region) is $L_{\text{dephase}} \simeq \lambda_p(\omega/\omega_p)^2$, where λ_p is the plasma wavelength.

Driver depletion can also limit the interaction length. As the drive laser pulse propagates through the plasma, it leaves behind a plasma wave. The energy of the plasma wave is provided by the driver, which is depleted. Driver depletion becomes more severe as the intensity of the laser increases owing to the fact that the amplitude of the generated longitudinal field is proportional to the power of the drive laser pulse, and therefore the energy in the plasma wave is proportional to a^4. Since the total energy in the driver is proportional to a^2, the depletion distance is inversely proportional to the laser pulse power. For a weakly relativistic pulse of size λ_p, the depletion length scales as $L_{\text{deplete}} \sim \lambda_p(\omega/\omega_p)^2/a^2 = L_{\text{dephase}}/a^2$. As this scaling indicates, for small a, the driver depletion length should be secondary to dephasing.

For typical parameters of laser-plasma accelerator experiments (e.g., Table 1.1), $Z_R \ll L_{\text{dephase}} < L_{\text{deplete}}$ and the weakening of the laser pulse intensity due to diffraction, which scales as the Rayleigh range Z_R, is the most severe limitation on the interaction length. To overcome this limitation, the use of a preformed plasma density channel to provide optical guiding has been proposed [36, 37].

1.2 Summary and Outline

Plasma-based accelerators have the ability to support large accelerating gradients. The laser wakefield accelerator is the most promising laser-driven mechanism for plasma wave generation. The most severe limitation to this plasma-based accelerator scheme is diffraction of the laser pulse. Therefore a successful plasma-based accelerator which utilizes a laser driver will require some form of optical guiding. A hollow plasma channel can provide guiding of the laser pulse, thereby extending the accelerator length and the energy gain of the accelerated particle beam. Chapter 2 of this dissertation examines the performance of a hollow plasma channel as an accelerating structure.

The use of a plasma channel will allow one to overcome diffraction. With optical guiding provided by a plasma channel, the accelerator length will be limited by the transverse stability of the accelerated beam. Chapter 3 addresses this issue by computing the characteristic growth lengths of the transverse beam breakup instability in various regimes for a particle beam propagating in a hollow plasma channel.

As the calculations presented in Sec. 1.1.1 indicate [cf. Eqs. (1.7) and (1.9)] the wavelength of the excited plasma wave scales as the plasma wavelength $\lambda_p = 2\pi c/\omega_p$. Therefore the usefulness of plasma-based accelerators depends on a method for producing electron bunches much shorter than the plasma wavelength. Chapter 4 examines a method of producing ultrashort electron bunches by dephasing and trapping background plasma electrons undergoing fluid oscillations in an excited plasma wave.

The self-consistent propagation of a laser pulse through a plasma is of particular importance to laser-driven acceleration schemes. For ultrashort laser pulses, such as those used in the LWFA scheme, finite pulse length effects will significantly influence the laser pulse propagation. In Chapter 5, the evolution of a laser pulse in an underdense plasma is presented including finite pulse length effects and the effects

of nonlinear plasma wave excitation. In addition to the limitations of laser-driven plasma-based accelerators discussed in Sec. 1.1.2, laser-plasma instabilities can significantly degrade the laser pulse driver and limit the interaction length. Laser-plasma instabilities are examined in Chapter 5.

The theoretical work presented in this dissertation is summarized in Chapter 6. Conclusions and prospects for future theoretical and computational work are offered. Possible experimental applications of the results of this work are discussed.

Chapter 2

Plasma Wave Excitation in a Hollow Plasma Channel

In this chapter, a hollow plasma channel is examined as an accelerating structure. The excitation of plasma waves in an externally preformed hollow plasma channel by a laser pulse or relativistic particle beam is analyzed in Sec. 2.2. The loss factors for the channel modes, which quantify the energetics of excitation, are calculated in Sec. 2.3. Section 2.4 discusses the effects of non-ideal hollow plasma channels, which includes sensitivity to errors in channel radius and plasma density. The hollow plasma channel is characterized in terms of the fundamental accelerator parameters: mode frequencies and loss factors. This characterization allows for the analysis of beam propagation and stability presented in Chapter 3.

2.1 Introduction

As was discussed in Chapter 1, diffraction is the most severe limitation for laser-driven plasma-based accelerators. Therefore, a successful design of a plasma-based accelerator which utilizes a laser driver must include some form of optical guiding. Two schemes for optical guiding are being explored for overcoming diffrac-

tion: relativistic self-focusing [15, 38] and plasma channel guiding [36, 39].

The mechanism for relativistic self-focusing relies on the energy dependence of the plasma frequency. The electron momentum will be larger where the laser pulse is more intense ($\vec{u} \simeq \vec{a} \propto I^{1/2}$, where I is the laser intensity) due to the quiver motion of the plasma electrons in the presence of the laser field. Therefore the plasma frequency will be lower in regions of intense laser fields owing to the relativistic mass increase. The result of this effect will be that the laser pulse will generate a nonlinear index of refraction

$$\eta \simeq 1 - \frac{1}{2\gamma}\frac{\omega_p^2}{\omega^2}\,, \tag{2.1}$$

where $\gamma \simeq (1+a^2)^{1/2}$. The index of refraction will be larger at the center of the pulse than at the pulse edges and therefore can guide a laser pulse. Analysis has shown that in steady-state, relativistic self-focusing can focus the laser pulse whenever the total laser pulse power is greater than the critical power [15] given by $P_{\rm crit} \simeq 17(\omega/\omega_p)^2$ GW.

Relativistically self-focused long laser pulses (i.e., pulse lengths much longer than the plasma wavelength) suffer from Raman forward and sidescatter instabilities [21]. These instabilities lead to break up of the pulse into small pulses of order the plasma wavelength and therefore limit the propagation distance of the laser pulse. For short laser pulses (i.e., pulse lengths of order the plasma wavelength), such as those used in the standard laser wakefield accelerator, relativistic self-focusing is substantially reduced. This is due to the generation of a plasma density perturbation by the ponderomotive force of the laser. For short pulses, the plasma frequency decrease from relativistic effects is balanced by this density perturbation [36]. Consequently, the index of refraction will have no transverse variation and the plasma cannot optically guide the short laser pulse.

An alternate method for overcoming laser diffraction, which has received a large amount of experimental effort [40, 41, 42, 43], is to use a plasma density channel to guide the laser pulse. This method uses a plasma channel that has a higher plasma

density outside the channel than inside the channel, $\partial n_e/\partial r > 0$, giving the plasma channel an index of refraction which decreases from the channel axis $\partial \eta/\partial r < 0$. A fixed plasma channel is analogous to an optical fiber and its guiding properties can be similarly analyzed. Plasma channels can be used to guide short pulses and have been studied analytically using axisymmetric models for a parabolic plasma density variation [36] and for hollow plasma channels [37].

Calculations show that a hollow plasma channel, in addition to optically guiding the laser pulse, supports a plasma wave with attractive properties for particle acceleration. The driver excites a surface mode in the plasma which extends into the channel. Unlike in a homogeneous plasma or parabolic channel, the transverse profile of the driver is decoupled from the transverse profile of the accelerating mode. Therefore, for a relativistic driver, the accelerating gradient of the fundamental mode is uniform and the focusing fields are linear [37]. In addition, the excited fields in a hollow plasma channel are fully electromagnetic, unlike the electrostatic fields excited in a homogeneous plasma. These properties make a hollow plasma channel well-suited as a structure for both particle beam and laser-driven wakefield accelerators.

Since the original demonstration of the guiding of a low-intensity laser pulse in a plasma channel at the University of Maryland [39], several research groups are examining experimental methods of plasma channel formation and guiding of high-intensity lasers [40, 41, 42, 43]. Methods of forming a plasma channel include: inverse bremsstrahlung heating of the plasma by a precursor laser pulse resulting in hydrodynamic expansion and channel formation [40, 42] and discharge ionization of a preformed capillary tube [44, 43]. Table 2.1 summarizes the parameters and results of plasma channel laser guiding experiments.

In this Chapter, an externally formed hollow plasma channel is characterized as an accelerating structure, independent of the structure excitation mechanism (laser or particle beam). The results provide the basic scalings for the plasma channel accelerator, including current limiting higher-order mode couplings. Instabilities which result from the beam-plasma coupling are discussed in Chapter 3.

	I [W/cm^2]	τ_L [fs]	λ [μm]	n_0 [cm^3]	r_{ch} [μm]	L_{guided} [cm]
UMCP (USA) [40]	5×10^{15}	500	0.565	7×10^{18}	30	2 (45 Z_R)
LBNL (USA) [42]	5×10^{17}	75	0.8	7×10^{18}	5	0.1 (8 Z_R)
NRL (USA) [43]	10^{17}	400	1.05	10^{18}	500	2 (22 Z_R)

Table 2.1: Parameters and results for plasma channel laser guiding experiments. The laser intensity I, the laser pulse duration τ_L, the laser wavelength λ, the plasma density n_0, the characteristic radius of the plasma channel r_{ch}, and the propagation length of the guided laser pulse L_{guided} (measured in centimeters and number of Rayleigh lengths) are listed for each experiment.

2.2 Mode Structure of the Hollow Plasma Channel

In this section, the excited fields in the hollow plasma channel are derived. This analysis assumes that the driver (beam current or laser pulse) remains unaltered during the evolution of the fields. To model the excitation of the hollow plasma channel, consider an equilibrium electron plasma density $n_e(r) = n_o\Theta(r - r_{\text{w}})$, where Θ is the Heaviside step function, r_{w} is the radius of the channel wall, and n_o is the number density of the plasma outside the channel. The ion plasma density is assumed to be equal to the equilibrium electron plasma density $n_i = n_e$. The ions are also assumed to remain motionless since the drive pulse duration is taken to be much shorter than the response time of the ions.

The wave equation for the electric field $\vec{E}$ can be obtained from the Maxwell equations,

$$\left(c^2\nabla^2 - \frac{\partial^2}{\partial t^2}\right)\vec{E} = 4\pi\frac{\partial}{\partial t}\vec{J} + 4\pi c^2\nabla\rho\,. \tag{2.2}$$

The current $\vec{J}$ and charge density ρ source terms in Eq. (2.2) can be separated into the contribution from the external driver and the contribution due to the plasma: $\vec{J} = \vec{J}_{\text{ext}} + \vec{J}_{\text{p}}$ and $\rho = \rho_{\text{ext}} + \rho_{\text{p}}$. Linearizing the fluid equations for a cold collisionless plasma [Eqs. (1.1) and (1.2)] provides an equation for the plasma response (assuming

a static equilibrium plasma density),

$$4\pi\frac{\partial}{\partial t}\vec{J}_{\rm p} = \omega_p^2\vec{E}\ . \tag{2.3}$$

By separating the source terms and using the fluid equation for the plasma current, Eq. (2.2) can be rewritten as

$$\left(c^2\nabla^2 - \frac{\partial^2}{\partial t^2} - \omega_p^2\right)\vec{E} = 4\pi\frac{\partial}{\partial t}\vec{J}_{\rm ext} + 4\pi c^2\nabla\left(\rho_{\rm ext} + \rho_{\rm p}\right)\ . \tag{2.4}$$

The magnetic field is obtained from Faraday's law $c\nabla\times\vec{E} = -\partial_t\vec{B}$,

$$\left(c^2\nabla^2 - \frac{\partial^2}{\partial t^2} - \omega_p^2\right)\vec{B} = -4\pi c\nabla\times\vec{J}_{\rm ext}\ . \tag{2.5}$$

For a hollow plasma channel, $\nabla\rho_{\rm p} = 0$ in all regions, and the wave equations Eqs. (2.4) and (2.5) become

$$\left(c^2\nabla^2 - \frac{\partial^2}{\partial t^2} - \omega_p^2\right)\vec{E} = 4\pi\frac{\partial}{\partial t}\vec{J}_{\rm ext} + 4\pi c^2\nabla\rho_{\rm ext}\ , \tag{2.6}$$

$$\left(c^2\nabla^2 - \frac{\partial^2}{\partial t^2} - \omega_p^2\right)\vec{B} = -4\pi c\nabla\times\vec{J}_{\rm ext}\ . \tag{2.7}$$

Note that if the term $\nabla\rho_{\rm p}$ is nonvanishing, then resonant absorption [45] is possible in the plasma channel walls and the excited fields can mode convert into an electrostatic Langmuir wave. This energy exchange between the electromagnetic fields in the channel and an electrostatic Langmuir wave in the plasma will damp the channel fields and lead to an effective quality factor of the plasma channel [46].

The source terms in the wave equations are determined by the external driver. For beam-driven excitation of the plasma channel, $\vec{J}_{\rm ext} = \vec{v}_b\rho_b$, where ρ_b is the beam charge density and $\vec{v}_b$ is the beam velocity. For excitation by a laser pulse, the current source is driven, to lowest-order, by the ponderomotive force of the laser pulse envelope (i.e., the gradient of the radiation pressure). The general ponderomotive force is given by Eq. (1.4). In the limit $a \ll 1$, the leading-order electron motion is the quiver velocity. To second-order, expansion of the momentum

equation Eq. (1.3) yields $\partial_t \vec{u}_2 = c\nabla(\phi_2 - a^2/2)$. Therefore, the current source driven by the ponderomotive force of the laser pulse, to second-order in the normalized vector potential of the laser, is

$$4\pi \frac{\partial}{\partial t} \vec{J}_{\rm ext} = \frac{m_e c^2}{e} \omega_p^2 \nabla \frac{a^2}{2} . \tag{2.8}$$

For the linear analysis presented in this chapter to be valid, surface plasma density perturbations should be small compared to the channel radius. This implies a laser pulse driver must satisfy $a^2 \ll 1$ (assuming the laser spot size is of order the channel radius $r_0 \sim r_{\rm w}$ and the laser pulse duration is of order the plasma period $\omega_p \tau_L \sim 1$), and a particle drive beam must satisfy $N_b \ll (\omega_p/c) r_{\rm w}^2/r_e$, where $r_e = e^2/(m_e c^2)$ is the classical electron radius and N_b is the number of electrons per bunch. For illustration, if $r_{\rm w} = 20$ μm and $n_0 = 7 \times 10^{16}$ cm^{-3}, then the linear theory will be valid for beams with $N_b \ll 7 \times 10^9$ electrons.

2.2.1 Channel Modes

In this section, the modes of the plasma channel synchronous with the driver are derived. The driver is assumed to be nonevolving and propagating axially with group velocity near the speed of light $c\beta \simeq c$. Explicity, the "frozen-field" approximation, axial variation at a fixed position is small and the modes are functions of the co-moving coordinate $\tau = t - z/(\beta c)$, is valid. In this analysis, the fields are decomposed into discrete azimuthal modes with mode index m and a Fourier transform in the co-moving coordinate τ is made such that solutions are of the form $\exp(-i\omega_m \tau + im\theta)$, with the mode frequencies ω_m. The boundary conditions across the channel wall are: continuity of the electric and magnetic field components $\epsilon_m \vec{E} \cdot \hat{r}$, $\vec{E} \times \hat{r}$, and $\vec{B}$, where $\epsilon_m = 1 - \omega_p^2(r)/\omega_m^2$ is the dielectric function of the plasma-vacuum structure.

To study the excited channel modes synchronous with the driver, let $\vec{E} = \hat{A}_m \vec{e}_m(r,\theta) \exp(-i\omega_m \tau)$ and $\vec{B} = \hat{A}_m \vec{b}_m(r,\theta) \exp(-i\omega_m \tau)$, where $\hat{A}_m$ are constants

determined by the excitation mechanism. With these definitions, the equation for the plasma wave electric field behind the drive pulse is

$$\left[c^2\nabla_\perp^2 - \omega_m^2(\beta^{-2} - \epsilon_m)\right]\vec{e}_m = 0\,, \tag{2.9}$$

where $\nabla_\perp$ is the transverse Laplacian. Note that only transverse modes (i.e., $\nabla\cdot\vec{E} = 0$) exist in the channel, and since there are no linear surface currents, the continuity of $\nabla\times\vec{E}$ requires the mode in the plasma to also be transverse.

For the fundamental mode $m = 0$, the solutions to the homogeneous wave equation Eq. (2.9) are

$$e_{0z} = \frac{ik_1c\beta}{\omega_0}\frac{I_0(k_1r)}{I_1(k_1r_w)} \tag{2.10}$$

$$e_{0r} = \frac{I_1(k_1r)}{I_1(k_1r_w)} \tag{2.11}$$

$$b_{0\theta} = \beta\frac{I_1(k_1r)}{I_1(k_1r_w)} \tag{2.12}$$

in the channel $r < r_w$, and

$$e_{0z} = -\frac{ik_2c\beta}{\omega_0\epsilon_0}\frac{K_0(k_2r)}{K_1(k_2r_w)} \tag{2.13}$$

$$e_{0r} = \frac{1}{\epsilon_0}\frac{K_1(k_2r)}{K_1(k_2r_w)} \tag{2.14}$$

$$b_{0\theta} = \beta\frac{K_1(k_2r)}{K_1(k_2r_w)} \tag{2.15}$$

in the plasma $r > r_w$, where I_m and K_m are m^{th}-order modified Bessel functions of the second kind and

$$k_1 = \frac{\omega_m}{c}\left(\beta^{-2} - 1\right)^{1/2} \tag{2.16}$$

$$k_2 = \frac{\omega_m}{c}\left(\beta^{-2} - 1 + \omega_p^2/\omega_m^2\right)^{1/2}\,. \tag{2.17}$$

Note that in the limit of an ultra-relativistic driver ($\beta \to 1$), $k_1 \simeq 0$ and $k_2 \simeq \omega_p/c$. The fundamental mode $m = 0$ frequency (eigenvalue equation) is

$$\omega_0 = \omega_p\Omega_0 = \omega_p\left[1 + \frac{k_2I_1(k_1r_w)K_0(k_2r_w)}{k_1I_0(k_1r_w)K_1(k_2r_w)}\right]^{-1/2}\,, \tag{2.18}$$

where $\Omega_m = \omega_m/\omega_p$ is the normalized frequency of the m^{th} mode.

The higher-order modes $m > 0$ of the excited plasma wave are

$$e_{mz} = \frac{k_1 c\beta}{\omega_m}\frac{I_m(k_1 r)}{I_m(k_1 r_w)} f(m\theta) \tag{2.19}$$

$$b_{mz} = \frac{k_1 c\beta}{\omega_m}\Upsilon\frac{I_m(k_1 r)}{I_m(k_1 r_w)} g(m\theta) \tag{2.20}$$

in the channel $r < r_w$, and

$$e_{mz} = \frac{k_2 c\beta}{\omega_m}\frac{K_m(k_2 r)}{K_m(k_2 r_w)} f(m\theta) \tag{2.21}$$

$$b_{mz} = \frac{k_2 c\beta}{\omega_m}\Upsilon\frac{K_m(k_2 r)}{K_m(k_2 r_w)} g(m\theta) \tag{2.22}$$

in the plasma $r > r_w$, where $f(m\theta) = \cos(m\theta)$ and $g(m\theta) = -\sin(m\theta)$ for even modes or $f(m\theta) = \sin(m\theta)$ and $g(m\theta) = \cos(m\theta)$ for odd modes. In Eqs. (2.20) and (2.22), Υ is

$$\Upsilon = \frac{2m}{\beta}\left(\frac{k_2^2 - k_1^2}{r_w^2 k_1^2 k_2^2}\right)\left[\frac{I_{m+1}(k_1 r_w) + I_{m-1}(k_1 r_w)}{k_1 r_w I_m(k_1 r_w)} + \frac{K_{m+1}(k_2 r_w) + K_{m-1}(k_2 r_w)}{k_2 r_w K_m(k_2 r_w)}\right]^{-1}. \tag{2.23}$$

The transverse fields for the higher-order modes can be computed directly from the axial components Eqs. (2.19)-(2.22) using the relations

$$\vec{e}_{m\perp} = \frac{ic\beta^2}{\omega_m(1-\epsilon_m\beta^2)}\left[\hat{z}\times\nabla_\perp b_{mz} - \beta^{-1}\nabla_\perp e_{mz}\right] \tag{2.24}$$

$$\vec{b}_{m\perp} = \frac{-ic\beta^2}{\omega_m(1-\epsilon_m\beta^2)}\left[\epsilon_m\hat{z}\times\nabla_\perp e_{mz} + \beta^{-1}\nabla_\perp b_{mz}\right]. \tag{2.25}$$

The eigenvalue equation for the higher-order modes is

$$\frac{4m^2}{\beta^2}\left(\frac{k_2^2 - k_1^2}{r_w^2 k_1^2 k_2^2}\right)^2 = \left[\frac{I_{m+1}(k_1 r_w) + I_{m-1}(k_1 r_w)}{k_1 r_w I_m(k_1 r_w)} + \frac{K_{m+1}(k_2 r_w) + K_{m-1}(k_2 r_w)}{k_2 r_w K_m(k_2 r_w)}\right]\times \left\{\frac{I_{m+1}(k_1 r_w) + I_{m-1}(k_1 r_w)}{k_1 r_w I_m(k_1 r_w)} + \frac{\epsilon_m\left[K_{m+1}(k_2 r_w) + K_{m-1}(k_2 r_w)\right]}{k_2 r_w K_m(k_2 r_w)}\right\}. \tag{2.26}$$

The solutions of Eq. (2.26) provide the higher-order mode frequencies ω_m.

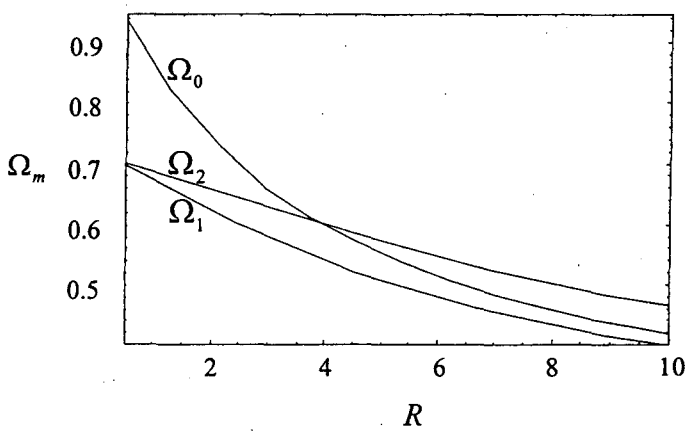

Figure 2.1: Normalized mode frequencies, $\Omega_m = \omega_m/\omega_p$, for $m = 0, 1, 2$ versus normalized channel radius $R = \omega_p r_w/c$ in the ultra-relativistic limit.

2.2.2 Ultra-Relativistic Limit

In the ultra-relativistic limit ($\beta \to 1$), the linearly excited mode frequencies of the hollow plasma channel Eqs. (2.18) and (2.26) become [47]

$$\omega_m = \omega_p \Omega_m = \omega_p \left[\frac{(1+\delta_{m0})(m+1)K_{m+1}(R)}{2(m+1)K_{m+1}(R) + RK_m(R)} \right]^{1/2} , \tag{2.27}$$

where $R = \omega_p r_w/c$ is the normalized channel radius and $\delta_{m0} = 1$ for $m = 0$ and zero otherwise. The three lowest-order mode frequencies plotted versus normalized channel radius are shown in Fig. 2.1.

The forces on a beam due to the excited fields have attractive properties for particle acceleration. The excited fundamental mode fields in the channel Eqs. (2.10)-(2.12) provide the axial and transverse forces

$$F_z \simeq -eA_0 \cos(\omega_0 \tau) , \tag{2.28}$$

$$F_r \simeq eA_0 (1 - \beta_z \beta) \frac{\omega_0}{2} r \sin(\omega_0 \tau) , \tag{2.29}$$

where A_0 is a constant determined by the excitation mechanism and $c\beta_z$ is the axial velocity of a witness charged particle beam. Inside the channel, in the ultra-

relativistic limit, the axial (accelerating) field is uniform with respect to transverse position as indicated by Eq. (2.28). Therefore electrons at different radii gain energy at the same rate, minimizing the energy spread due to the transverse extent of the beam. The transverse fields are linear with respect to the radial position as indicated by Eq. (2.29), which implies the root-mean-squared transverse normalized emittance will be conserved for any beam slice [48]. Note that the focusing due to the excited fundamental mode fields is typically small in the ultra-relativistic limit (i.e., $|F_r/F_z| \sim 1 - \beta_z\beta \ll 1$). In addition, there is a $\pi/4$ phase region where the fundamental channel mode both focuses transversely and accelerates longitudinally. These properties make the hollow plasma channel well-suited for an accelerating structure independent of excitation mechanism.

2.3 Energetics

The interaction of the beam with the accelerator environment can be quantified by a calculation of the loss factors [49]. The loss factor per unit length κ relates the accelerating gradient to the energy stored per unit length in the structure U by $\kappa = E_z^2/4U$. The loss factor κ is related to the more familiar quantity $[R/Q]$ (the shunt impedance per unit length divided by the quality factor) by $\kappa = \omega[R/Q]/4$. It is a purely geometrical factor of the structure independent of excitation mechanism. Since the loss factor is independent of the means of energy deposition, it is a figure of merit for comparisons of accelerating structures.

For an ultra-relativistic driver, the conserved electromagnetic energy density, from the Poynting equation, averaged over plasma wave phase is

$$\mathrm{u_{field}} = \frac{1}{16\pi}\left[(E_r - B_\theta)^2 + (E_\theta + B_r)^2 + E_z^2 + B_z^2\right] . \tag{2.30}$$

Using the fluid equation Eq. (2.3), the energy density stored in the plasma fluid motion can be expressed in terms of the fields as

$$\mathrm{u_{fluid}} = \frac{2\pi}{\omega_p^2}J_\mathrm{p}^2 = \frac{1}{16\pi}\Omega_m^{-2}\left(E_r^2 + E_\theta^2 + E_z^2\right) . \tag{2.31}$$

Performing the integral over the transverse coordinates of the field and fluid energy densities Eqs. (2.30) and (2.31) yields the total energy per unit length stored in the structure due to the excitation of the m^{th} mode

$$U_m = \int_0^\infty d^2\vec{r}_\perp (\mathrm{u_{field}} + \mathrm{u_{fluid}}) = \frac{c^2}{\omega_p^2} A_m^2 (1+\delta_{m0}) \frac{R^{2m+1} K_{m+1}(R)}{8\Omega_m^2 K_m(R)} \,. \tag{2.32}$$

Here A_m are constants determined by the excitation mechanism, and $A_m R^m$ is the peak axial electric field of the m^{th} mode at the channel radius. The energy stored in the fundamental mode U_0 is a lower bound on the amount of energy per unit length that must be deposited in the structure to produce a desired accelerating gradient A_0 in the channel.

Using Eq. (2.32), the loss factor per unit length for the m^{th} mode [47] is

$$\kappa_m = \frac{\omega_p^2}{c^2} \left[\frac{K_m(R)}{RK_{m+1}(R)}\right] \left[1 + \frac{RK_m(R)}{2(m+1)K_{m+1}(R)}\right]^{-1} , \tag{2.33}$$

where the axial electric fields of the higher-order modes have been evaluated at the channel radius. The $[R/Q]$ for the hollow plasma channel structure is

$$\left[\frac{R}{Q}\right]_0 = \frac{Z_o}{\lambda_p} \left[\Omega_0 \frac{2K_0(R)}{RK_1(R)}\right] \tag{2.34}$$

for the fundamental mode, and

$$\left[\frac{R}{Q}\right]_m = \frac{Z_o}{\lambda_p} \left[\frac{4K_m(R)}{RK_{m+1}(R)}\right] \left[2 + \frac{RK_m(R)}{(m+1)K_{m+1}(R)}\right]^{-1/2} \tag{2.35}$$

for the higher-order $m > 0$ modes, where $Z_o = 4\pi/c = 120\pi$ ohms is the impedance of free space.

For comparison, the fundamental mode of a scaled disk-loaded copper SLC structure [49] has a loss factor of $\kappa_0 \approx 2.1 \times 10^3 \lambda^{-2}(\mathrm{cm})$ V/(pC m), while the fundamental mode loss factor in a hollow plasma channel is

$$\kappa_0 = 3.6 \times 10^3 \lambda_0^{-2}(\mathrm{cm}) \left[\frac{K_0(R)}{RK_1(R)}\right] \frac{\mathrm{V}}{(\mathrm{pC\ m})} , \tag{2.36}$$

where $\lambda_0 = \Omega_0^{-1} 2\pi c/\omega_p$ is the accelerating wavelength. For a normalized channel radius of $R = 1$, the fundamental mode loss factor is $\kappa_0 = 2.5 \times 10^3 \lambda_0^{-2}(\mathrm{cm})$ V /(pC

m), somewhat larger than the conventional resonantly-excited conducting structure, which implies stronger beam loading and smaller stored energy per unit length for a given accelerating gradient. Note that a larger loss factor results not only in greater energy deposition, but also in larger wakefield excitation. The latter could result in instabilities and lead to greater energy spread, as studied in Chapter 3.

To further appreciate the implications of Eq. (2.33), consider a numerical example where, for simplicity, only the fundamental mode, with a wavelength $\lambda_0 = \Omega_0^{-1} 2\pi c/\omega_p \approx 146$ μm, is excited. For a channel radius $r_w \approx 20$ μm, $R \approx 1$ and the loss factor is $\kappa_0 \approx 12$ MV/(pC m). If a 10 GV/m accelerating gradient is desired, the energy stored in the structure is $U_0 = A_0^2/4\kappa_0 \approx 2$ J/m. Assuming the drive pulse is fed once per meter, one sees that the drive pulse energy must exceed 2 J, accounting for losses due to coupling to the accelerating mode.

The energy stored in the plasma structure U_m is equal to the energy deposited by the driver,

$$U_m = \frac{1}{c} \int d^3\vec{r} \vec{J}_{\rm ext} \cdot \vec{E}_m \, . \tag{2.37}$$

For an ultra-relativistic charge q at a radius r_b, with $r_b < r_w$, the total energy deposited in the plasma structure by the charge can be written as

$$U = \sum_m U_m = \sum_m \kappa_m (r_b/r_w)^{2m} q^2 \, . \tag{2.38}$$

This is the total energy loss in the sense that, unlike a conventional structure, there are no other synchronous modes supported by the structure. Furthermore, the relation $\beta^2 \epsilon_m < 1$ will always be satisfied for the plasma-vacuum structure since $\epsilon_m = 1 - \omega_p^2(r)/\omega_m^2 \leq 1$ and β is the driver group velocity. Therefore no energy will be lost radially in the hollow plasma channel through Cherenkov radiation [33].

2.4 Error Sensitivity

The promise of the hollow plasma channel depends on the ability to form such a structure. A realistic channel will have errors in the mode frequencies and

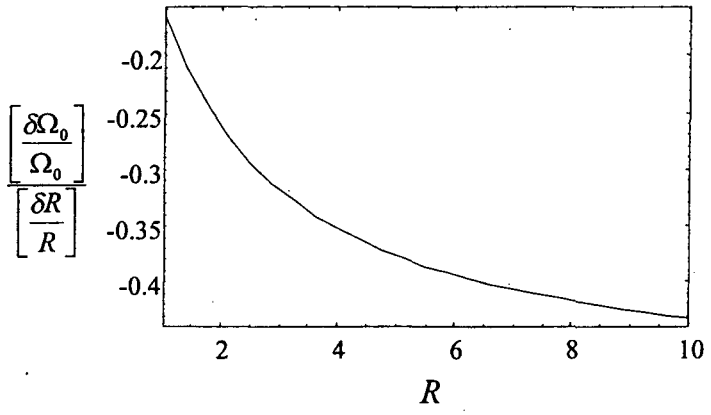

Figure 2.2: Fractional fundamental mode detuning normalized to fractional channel radius, versus normalized channel radius.

loss factors due to many effects, for example: variation in the plasma density, a finite plasma density in the channel n_c, or finite thickness of the plasma walls. Equation (2.27) implies that fractional errors in ω_p produces equal fractional errors in ω_m due to the leading ω_p term and a frequency error due to the variation in R. Errors in the channel radius also produce errors in R. The ratio of the fractional error in frequency $\delta\Omega_m/\Omega_m$ to the fractional error in channel radius $\delta R/R$ (assuming no fluctuations in plasma density) is

$$\left[\frac{\delta\Omega_m}{\Omega_m}\right]\left[\frac{\delta R}{R}\right]^{-1} = \frac{B^2}{4(m+1)}\left[1+\frac{RK_m(R)}{2(m+1)K_{m+1}(R)}\right]^{-1} - \frac{RK_m(R)}{2K_{m+1}(R)}. \quad (2.39)$$

Figure 2.2 shows the ratio of fractional error in fundamental mode frequency to the fractional error in channel radius. As the figure indicates, operating at a smaller channel radius yields tighter tolerances of frequency to errors in channel radius.

A finite plasma density inside the channel n_c will shift the mode frequencies. For the m^{th} mode, the mode frequency shift $\Delta\omega_m = \omega_m(n_c > 0) - \omega_m(n_c = 0)$ is

$$\frac{\Delta\omega_m}{\omega_m} = \frac{n_c}{n_o}\left[\frac{(1-\delta_{m0})(m+1)K_{m+1}(R) + RK_m(R)}{2(1+\delta_{m0})(m+1)K_{m+1}(R)}\right]. \quad (2.40)$$

Furthermore, an undesirable electrostatic mode may also be excited by the drive

pulse in a partially filled channel. This electrostatic mode will be a source of energy loss in the system. Nonlinear effects, such as self-trapping, become important at a lower field amplitude in a partially filled plasma channel. Self-trapping of electrons from the accelerator viewpoint is one source of "dark-current" [50] (electrons emitted from the structure), and may set a limit on the peak gradient.

The important problem of finite wall thickness leads to a quality factor of the plasma structure [46]. In our model, this figure is infinite. Numerical simulations which include finite wall thickness [51] suggest that the quality factor of the channel can be small due to resonant absorption in the walls of the channel.

2.5 Summary

In summary, the hollow plasma channel has been characterized in terms of the fundamental accelerator parameters: mode frequencies (eigenvalues) and loss factors (eigenfunctions) of the electromagnetic channel modes. With these results, one can quantify for the first time the performance of a high-energy machine based on this plasma structure. In order to reach TeV-energies, such a plasma-based accelerator would consist of many stages. With optical guiding provided by the plasma channel, the length of a single stage based on a hollow plasma channel structure would be fundamentally limited by the shorter of the the dephasing length and the driver depletion length, as discussed in Chapter 1. In practice, the length of a plasma-based accelerator may be limited by beam-plasma instabilities.

Plasmas provide strong coupling for acceleration of particle beams, quantified in the loss factors calculated in this chapter. At the same time this strong coupling extends to strong deflection and breakup of the beam. The barrier to a compact TeV-energy accelerator based on the hollow plasma channel structure will be transverse beam stability. Using the results derived in this chapter, beam-plasma instabilities in the hollow plasma channel are examined Chapter 3.

Chapter 3

Particle Beam Dynamics in a Hollow Plasma Channel

In this chapter, the stability of a charged particle beam propagating in a hollow plasma channel is examined using the results derived in Chapter 2. Section 3.2 addresses the coupling of the dipole wakefield excited in the plasma channel to the transverse displacement of the beam. Single-bunch beam breakup growth lengths are derived for beam propagation in in the weak-focusing and strong-focusing regimes. The effects of longitudinal wakefields on the beam energy spread are examined in Sec. 3.3. Multi-bunch beam breakup is discussed in Sec. 3.4, and methods for reducing beam breakup are proposed.

3.1 Introduction

As a charged particle beam travels through the plasma structure, it excites wakefield modes, and the modes in turn influence the beam propagation. Higher-order moments of the drive pulse distribution, present due to drive pulse shape or misalignment, will excite higher-order modes in addition to the fundamental (accelerating) mode. These higher-order modes can cause beam instabilities, limiting the

beam current.

The results presented in Chapter 2 can be used to model particle beam dynamics in a hollow plasma channel. The longitudinal and transverse forces on an ultra-relativistic beam due to its interaction with the plasma can be calculated from the convolution of the charge distribution of the beam with the wakefields $\vec{W} = \vec{E} + \hat{z} \times \vec{B}$ produced by all proceeding charges. The wakefields can be determined from the excited fields and using Eq. (2.37) to determine the field amplitude excited for a given source $\vec{J}_{\rm ext}$. The wakefields excited inside the hollow plasma channel by a ultra-relativistic point charge q, passing through the channel at radius r_b, with $r_b < r_{\rm w}$, and azimuthal angle $\theta = 0$ are

$$\vec{W}_{\parallel} = -q \sum_m \hat{W}_{\parallel m}(\tau) r^m r_b^m \cos(m\theta) \hat{z} \,, \tag{3.1}$$

$$\vec{W}_{\perp} = q \sum_m \hat{W}_{\perp m}(\tau) r^{m-1} r_b^m [\hat{r} \cos(m\theta) - \hat{\theta} \sin(m\theta)] \,, \tag{3.2}$$

with the wakefunctions,

$$\hat{W}_{\parallel m}(\tau) = \frac{2\kappa_m}{r_{\rm w}^{2m}} \cos[\Omega_m \omega_p \tau] \,, \tag{3.3}$$

$$\hat{W}_{\perp m}(\tau) = \frac{2m\kappa_m c}{r_{\rm w}^{2m} \Omega_m \omega_p} \sin[\Omega_m \omega_p \tau] \,. \tag{3.4}$$

Here Ω_m and κ_m the mode frequencies and loss factors given by Eqs. (2.27) and (2.33) respectively. Note that the Laplace transform of the wakefunctions Eqs. (3.3) and (3.4) yields the impedance of the plasma structure. These point charge wakefields Eqs. (3.1) and (3.2) can be used as Green functions to compute the longitudinal and transverse forces produced by an arbitrary beam charge distribution ρ_b, through a convolution of the distribution over the point charge response. The longitudinal wakefields will tend to cause energy spread within a beam, and the transverse wakefields will tend to cause beam breakup instabilities. Note that if the charge is near the axis of the channel, $r_b \ll r_{\rm w}$, then the longitudinal wakefield is dominated by the fundamental $m = 0$ mode and the transverse wakefield by the dipole $m = 1$ mode.

3.2 Transverse Instabilities

It is well-known in accelerator physics that interaction of the beam with the structure geometry can result in transverse instabilities coupled to the off-axis displacement of the beam centroid, or beam breakup instabilities [52, 53]. This section discusses beam breakup instabilities in a hollow plasma channel. A relativistic charged particle beam propagating off-axis with respect to the beamline will have a dipole moment. The axial current associated with this dipole moment will couple to the electric fields of the structure along the beamline. The associated transverse Lorentz force will give a kick to beam slices in the rear of the bunch, displacing them farther off-axis. In this way, an instability is obtained.

Consider the effect of a perturbation in the form of a small displacement of the beam centroid $X(z,\tau)$ in the transverse direction. The transverse displacement is expressed as a function of two variables: the propagation distance z and the distance from the head of the beam τ. The variable $\tau = t - z/v_b$ indexes beam slices where $v_b \simeq c$ is the axial beam velocity. The beam extends from $\tau = 0$ (the beam head) to $\tau = \tau_b$ (the beam tail). Beam electrons remain approximately at a fixed τ, as they advance in z along the length of the accelerator.

From the Lorentz force equation, assuming the beam is monoenergetic, the evolution of the transverse displacement of the beam due to the dipole transverse wakefield is

$$\left[\frac{\partial}{\partial z}\gamma(z)\frac{\partial}{\partial z} + \gamma(z)k_\beta^2(z)\right] X(z,\tau) = \int_0^\tau cI(\zeta)I_o^{-1}\hat{W}_{\perp 1}(\tau-\zeta)X(z,\zeta)d\zeta, \qquad (3.5)$$

where $I(\tau)$ is the beam current and $I_o = m_e c^3/e \approx 17$ kA is the Alfvén constant. The transverse dipole wakefunction $\hat{W}_{\perp 1}$ is given by Eq. (3.4) with $m = 1$ and determines the Lorentz force on an electron at τ as it arrives at z due to the fields generated by the beam segment at $\zeta < \tau$. The right-hand side of Eq. (3.5) is the cumulative force due to the transverse dipole wakefields of the proceeding charges in the beam. The transverse focusing force in the channel from a plasma wave (created by a drive

pulse) and from any external magnets can be described, in the linear approximation, by the betatron wavenumber $k_\beta(z)$. This model [i.e., Eq. (3.5)] is valid in the ultra-relativistic limit of the beam velocity, where phase slippage between particles in the bunch is small. Equation (3.5) can be solved in a variety of limits to study the single-bunch beam breakup instability [53].

3.2.1 Single-Bunch Beam Breakup

In this section, the asymptotic growth of the beam centroid is calculated for the case of a bunch much shorter than the natural periods of the wakefield (i.e., $\omega_p \tau_b \ll 1$). Assuming the beam density, which is proportional to the beam current, remains constant, Eq. (3.5) can be rewritten as

$$\left[\frac{\partial}{\partial z}\gamma(z)\frac{\partial}{\partial z} + \gamma(z)k_\beta^2(z)\right] X(z,\tau) = \int_0^\tau d\zeta G(\tau-\zeta)X(z,\zeta)\ , \tag{3.6}$$

where the Green function G is given by the excited wakefield,

$$G(\tau) = c\frac{I}{I_o}\hat{W}_{\perp 1}(\tau) = \left(\frac{I}{I_o}\frac{2\kappa_1\omega_p}{R^2\Omega_1}\right)\sin(\omega_1\tau) = G_1\sin(\omega_1\tau)\ . \tag{3.7}$$

In the limit of a short bunch, the wakefield response is approximately linear $G(\tau) \simeq (G_1\omega_1)\tau$.

If the growth length of the instability is much less than k_β^{-1} (i.e., the weak-focusing regime), then the term due to transverse focusing on the left-hand side of Eq. (3.6) can be neglected. This will typically be valid for ultra-relativistic beams propagating in hollow plasma channels without external focusing since the transverse focusing forces in the channel due to the excited fundamental mode fields will be small in the ultra-relativistic limit, as indicated by Eq. (2.29) with $(1-\beta_z\beta) \simeq 0$.

The growth of the transverse beam displacement can be solved by applying the Laplace transform of τ to both sides of Eq. (3.6),

$$\left[\frac{\partial}{\partial z}\gamma(z)\frac{\partial}{\partial z}\right]\tilde{X}(z,s) = \tilde{G}(s)\tilde{X}(z,s)\ , \tag{3.8}$$

where the tilde denotes the Laplace transform $\tilde{f}(s) = \mathcal{L}[f(\tau)] = \int_0^\infty f(\tau)\exp[-s\tau]d\tau$ for any function f. Assuming that the growth will be slow on the scale of the plasma period, an eikonal approximation can be applied to $\tilde{X}$ such that $\tilde{X}(z,s) = \chi_e(z,s)\exp[i\Phi_e(z,s)]$, where the amplitude $\chi_e(z,s)$ is slowly varying. With this definition, Eq. (3.8) yields the equations

$$\gamma\ddot{\chi}_e + \dot{\gamma}\dot{\chi}_e - \gamma\chi_e\dot{\Phi}_e^2 = \tilde{G}\chi_e\,, \tag{3.9}$$

$$2\gamma\dot{\chi}_e\dot{\Phi}_e + \gamma\ddot{\Phi}_e\chi_e + \dot{\gamma}\chi_e\dot{\Phi}_e = 0\,, \tag{3.10}$$

where the dots indicate partial differentiation with respect to z. Assuming the energy changes slowly during the period of the accelerating field and the eikonal approximation $|\dot{\chi}_e| \ll |\dot{\Phi}_e\chi_e|$ such that $\gamma\ddot{\chi}_e$ and $\dot{\gamma}\dot{\chi}_e$ are higher-order terms, then the solutions to Eqs. (3.9) and (3.10) are

$$\Phi_e(z,s) = \pm i\tilde{G}^{1/2}\int_0^z dz_1\gamma^{-1/2}(z_1)\,, \tag{3.11}$$

$$\chi_e(z,s) = \tilde{X}_0\left(\frac{\gamma_0\dot{\Phi}_0}{\gamma\dot{\Phi}_e}\right)^{1/2} = \tilde{X}_0\left(\frac{\gamma_0}{\gamma}\right)^{1/4}\,, \tag{3.12}$$

where $\gamma_0 = \gamma(z=0)$ is the initial beam energy, $\Phi_0 = \Phi_e(z=0,s)$, and $\tilde{X}_0 = \tilde{X}(z=0,s)$ is the Laplace transform of the initial displacement. Using Eqs. (3.11) and (3.12), the Laplace transform of the transverse displacement of the beam centroid is

$$\tilde{X}(z,s) = \tilde{X}_0\left(\frac{\gamma_0}{\gamma}\right)^{1/4}\exp\left[\pm\sqrt{\tilde{G}(s)}\int_0^z dz_1\gamma^{-1/2}(z_1)\right]\,. \tag{3.13}$$

Assuming an uniform initial transverse perturbation of the beam off axis X_0 such that the initial condition is $X(z=0,\tau) = X_0\Theta(\tau)$, where $\Theta(\tau)$ is the Heaviside step function, the Laplace transform of the initial displacement is $\tilde{X}_0 = \tilde{X}(z=0,s) = \mathcal{L}[X(z=0,\tau)] = X_0/s$. Inverting the Laplace transform of the transverse beam centroid displacement $X(z,\tau) = \mathcal{L}^{-1}[\tilde{X}(z,s)]$, Eq. (3.13) becomes

$$X(z,\tau) = X_0\left(\frac{\gamma_0}{\gamma}\right)^{1/4}\frac{1}{2\pi i}\int_{-i\infty}^{i\infty} ds\frac{1}{s}\exp\left[s\tau \pm \frac{\sqrt{G_1\omega_1}}{s}\int_0^z dz_1\gamma^{-1/2}(z_1)\right]\,. \tag{3.14}$$

In deriving Eq. (3.14), $\tilde{G}(s) = \mathcal{L}[G(\tau)] \simeq G_1\omega_1\mathcal{L}[\tau] = G_1\omega_1/s^2$ was used. Applying the method of steepest descents [54] to the integral in Eq. (3.14), one finds

$$X(z,\tau) \approx X_0 \left(\frac{\gamma_0}{\gamma}\right)^{1/4} \frac{\exp(\Lambda_w)}{\sqrt{8\pi\Lambda_w}}, \tag{3.15}$$

with the exponent

$$\Lambda_w = 2\left[\left(G_1\omega_1\tau^2\right)^{1/2} \int_0^z dz_1 \gamma^{-1/2}(z_1)\right]^{1/2}. \tag{3.16}$$

For an ultra-relativistic beam, the beam remains at approximately fixed τ. With fixed τ and $\omega_p\tau_b \ll 1$, the axial force Eq. (2.28) is constant along the beam and the energy growth is linear. Assuming linear energy growth $\gamma = \gamma_0 + gz$, where γ_0 is the initial energy and g is a constant accelerating gradient in beam energy, the exponent is

$$\Lambda_w = 2^{3/2}\left(\frac{G_1\omega_1\tau^2}{g^2}\right)^{1/4} \left(\gamma^{1/2} - \gamma_0^{1/2}\right)^{1/2}. \tag{3.17}$$

Asymptotically (for large z), the exponent Eq. (3.17) becomes

$$\Lambda_w \to 2^{3/2}\left(\frac{G_1\omega_1\tau^2 z}{g}\right)^{1/4} = \left(\frac{z}{L_w}\right)^{1/4}, \tag{3.18}$$

with the characteristic growth length

$$L_w = g\left(2^6 G_1\omega_1\tau^2\right)^{-1} = 2^{-7}\frac{I_o}{I}\frac{gR^2}{\kappa_1(\omega_p\tau)^2}. \tag{3.19}$$

This growth length will impose an upper bound on the accelerator length for a given $I\tau_b^2$ product. For example, in a plasma channel with plasma wavelength of 125 μm, channel radius of 20 μm, and accelerating gradient of 10 GV/m, a 3 fs beam with a charge of 1 pC will have an instability growth length of $L_w \approx 5$ mm. As Eq. (3.19) indicates the instability growth length can be increased by increasing R, which in turn will lower the loss factor of the structure for fixed plasma density.

The asymptotic growth of the transverse displacement of the beam centroid can also be determined for a particle beam which is traveling through an unexcited

hollow plasma channel and is therefore not accelerating (i.e., a coasting beam or drive beam). For a beam traveling through an unexcited structure ($g = 0$), the exponent Eq. (3.17) becomes

$$\Lambda_{\rm w} = 2\left(\frac{G_1\omega_1\tau^2}{\gamma_0}\right)^{1/4} z^{1/2} = \left(\frac{z}{L_{\rm wu}}\right)^{1/2}, \tag{3.20}$$

with the characteristic growth length

$$L_{\rm wu} = \frac{1}{4\tau}\left(\frac{\gamma_0}{G_1\omega_1}\right)^{1/2} = 2^{-5/2}\left[\frac{I_o}{I}\frac{\gamma_0 R^2}{\kappa_1(\omega_p\tau)^2}\right]^{1/2}. \tag{3.21}$$

As one can see from comparison of the growth lengths Eqs. (3.19) and (3.21), acceleration has a salubrious effect on the stability of the beam.

3.2.2 Single-Bunch Beam Breakup with External Focusing

For high-energy applications one may prefer not to operate in the weak-focusing regime $k_\beta L_{\rm w} \ll 1$; yet the transverse focusing in the hollow plasma channel due to the accelerating (fundamental) wakefield is weak for relativistic beams. In contrast, if external focusing (e.g., magnetic quadrupole lens) is applied in the plasma structure, the asymptotic growth of the transverse beam displacement is much reduced.

The asymptotic growth of the transverse centroid displacement of an accelerated and strongly focused beam can be determined by applying an eikonal approximation to Eq. (3.6), assuming the growth will be slow on the scale of a betatron period. Consider the slowly varying amplitude of the transverse centroid displacement $\chi(z,\tau)$ such that

$$X(z,\tau) = \left(\frac{\gamma_0\dot{\theta}_0}{\gamma\dot{\theta}_\beta}\right)^{1/2} \chi(z,\tau)\exp[i\theta_\beta(z)], \tag{3.22}$$

with the betatron phase

$$\theta_\beta(z) = \int_0^z dz_1 k_\beta(z_1) \tag{3.23}$$

and $\dot{\theta}_0 = \dot{\theta}_\beta(z=0)$. Substituting Eq. (3.22) into Eq. (3.6), assuming the eikonal approximation such that $|\dot{\gamma}| \ll |\gamma\dot{\theta}_\beta|$ and $|\dot{\chi}| \ll |\chi\dot{\theta}_\beta|$, and taking a Laplace transform in τ yields

$$\frac{\partial}{\partial z}\tilde{\chi}(z,s) = \frac{\tilde{G}}{2i\gamma\dot{\theta}_\beta}\tilde{\chi}(z,s)\,, \tag{3.24}$$

which has the solution

$$\tilde{\chi}(z,s) = \tilde{\chi}_0 \exp\left[\frac{\tilde{G}(s)}{2i}\int_0^z \frac{dz_1}{\gamma(z_1)\dot{\theta}_\beta(z_1)}\right]\,, \tag{3.25}$$

where $\tilde{\chi}_0 = \tilde{\chi}(z=0,s)$. Inverting the Laplace transform, the solution for the amplitude of the beam centroid is

$$\chi(z,\tau) = \frac{X_0}{2\pi i}\int_{-i\infty}^{i\infty}\frac{ds}{s}\exp\left[s\tau + \frac{\tilde{G}(s)}{2i}\int_0^z \frac{dz_1}{\gamma(z_1)\dot{\theta}_\beta(z_1)}\right]\,, \tag{3.26}$$

where the initial condition $\chi(z=0,\tau) = X_0\Theta(\tau)$ is assumed. The integral in Eq. (3.26) may be computed approximately by the method of steepest descents [54]. Using this method, one finds the transverse beam displacement is

$$X(z,\tau) \approx X_0 \frac{3^{1/4}}{2^{3/2}\pi^{1/2}}\left(\frac{\gamma_0\dot{\theta}_0}{\gamma\dot{\theta}_\beta}\right)^{1/2}\frac{\exp(\Lambda_s)}{\Lambda_s^{1/2}}\cos\left(\theta_\beta - \frac{\Lambda_s}{\sqrt{3}} + \frac{\pi}{12}\right)\,, \tag{3.27}$$

with the exponent

$$\Lambda_s = \frac{3^{3/2}}{4}\left[G_1\omega_1\tau^2\int_0^z\frac{dz_1}{\gamma(z_1)\dot{\theta}_\beta(z_1)}\right]^{1/3}\,. \tag{3.28}$$

In deriving Eq. (3.27), a short bunch was assumed $\omega_p\tau_b \ll 1$ such that $G(\tau) \simeq G_1\omega_1\tau$.

Considering linear energy growth $\gamma(z) = \gamma_0 + gz$ and assuming the betatron wavenumber has an energy dependence such that $k_\beta(z) = \dot{\theta}_\beta = \dot{\theta}_0(\gamma_0/\gamma)^\alpha$, the transverse beam displacement of a short bunch becomes

$$\frac{X(z,\tau)}{X_0} \approx \frac{3^{1/4}}{2^{3/2}\pi^{1/2}}\left(\frac{\gamma_0}{\gamma}\right)^{(1-\alpha)/2}\frac{\exp(\Lambda_s)}{\Lambda_s^{1/2}}\cos\left(\theta_\beta - \frac{\Lambda_s}{3^{1/2}} + \frac{\pi}{12}\right)\,, \tag{3.29}$$

with the betatron phase

$$\theta_\beta = \frac{\gamma_0^\alpha k_0}{g(1-\alpha)}\left(\gamma^{1-\alpha} - \gamma_0^{1-\alpha}\right) \tag{3.30}$$

and exponent

$$\Lambda_s = \frac{3^{3/2}}{2^{5/3}} \left[\frac{I}{I_o} \frac{\kappa_1 (\omega_p \tau)^2}{\alpha g \gamma_0^\alpha k_0 R^2} (\gamma^\alpha - \gamma_0^\alpha) \right]^{1/3} , \tag{3.31}$$

where $k_0 = k_\beta(z=0)$ is the initial betatron wavenumber at injection. Asymptotically, $\Lambda_s \to (z/L_s)^{\alpha/3}$, with the instability growth length

$$L_s = \frac{2^{5/\alpha}}{3^{9/2\alpha}} \left(\frac{I_o}{I} \right)^{1/\alpha} \left[\frac{\alpha g^{1-\alpha} \gamma_0^\alpha k_0 R^2}{\kappa_1 (\omega_p \tau)^2} \right]^{1/\alpha} . \tag{3.32}$$

For example, if $\alpha = 1/2$ (e.g., magnetic quadrupole lens), then the growth rate scales as $L_s \propto (I/I_o)^{-2} (\omega_p \tau)^{-4}$, which is a more favorable scaling than Eq. (3.19).

For a coasting or drive beam [i.e., no acceleration ($g = 0$)] traveling through an unexcited hollow plasma channel structure with strong external focusing, $\gamma(z) = \gamma_0$, $\theta(z) = k_\beta z$, and

$$\Lambda_s = \frac{3^{3/2}}{2^{5/3}} \left(\frac{G_1 \omega_1 \tau^2 z}{2 k_\beta \gamma_0} \right)^{1/3} = \left(\frac{z}{L_{su}} \right)^{1/3} , \tag{3.33}$$

where the characteristic growth length is

$$L_{su} = \frac{2^6 k_\beta \gamma_0}{3^{9/2} G_1 \omega_1 \tau^2} = \frac{2^5}{3^{9/2}} \frac{I_o}{I} \frac{k_\beta \gamma_0 R^2}{\kappa_1 (\omega_p \tau)^2} . \tag{3.34}$$

3.3 Longitudinal Instabilities

A beam loses energy when it traverses the hollow plasma channel accelerating structure owing to wakefields. This energy loss is called beam loading. Since the energy lost by a particle in the beam depends on its longitudinal position, the longitudinal wakefields Eq. (3.1) will cause an energy spread σ_γ within the beam. Energy spread constraints will therefore limit the beam current.

The energy change of an ultra-relativistic electron bunch propagating along the axis of the hollow plasma channel is described by the equation

$$\frac{\partial \gamma}{\partial z} = c I_o^{-1} E(\tau) - \int_0^\tau c I_o^{-1} I(\zeta) \hat{W}_{\parallel 0}(\tau - \zeta) d\zeta , \tag{3.35}$$

where $\hat{W}_{\|0}$ is the longitudinal fundamental mode wakefunction given by Eq. (3.3). Here $E(\tau) = A_0 \cos(\omega_0 \tau - \varphi_{\rm inj})$ is the accelerating gradient, with A_0 the peak axial electric field of an excited plasma wave (created by a drive pulse) and $\varphi_{\rm inj}$ the injection phase of the head of the bunch with respect to the plasma wave. For a delta function bunch $I(\tau) = q\delta(\tau)$ (i.e., a bunch much shorter than the period of the accelerating field $\omega_p \tau_b \ll 1$), one finds

$$\frac{\sigma_\gamma}{\gamma} \approx \frac{q\hat{W}_{\|0}(0)}{2E(0)} = \frac{q\kappa_0}{E(0)} \,. \tag{3.36}$$

For illustration, if an energy spread of order 0.1% is required in a plasma structure with $r_{\rm w} = 20$ μm, $R = 1$, and an accelerating gradient of 10 GV/m, then the beam-induced gradient should be held to $2\kappa_0 q \approx 20$ MV/m. The single-bunch charge q is then limited to 0.9 pC or 5×10^6 particles. In principle, the energy spread within a single bunch can be minimized and the charge limits increased by shaping the charge distribution of the bunch [55], although this may be difficult to achieve in practice.

3.4 Multi-bunch Beam Breakup

The longitudinal wakefields (beam loading) and transverse wakefields (beam breakup) constrain the charge in a single bunch. Therefore, to improve luminosity, a high-energy collider must operate with multiple bunches. The passage of intense bunches through the hollow plasma channel will leave behind wakefields which will influence subsequent bunches in a train. Each bunch in the train will experience the transverse dipole wakefield produced in the hollow plasma channel when the proceeding bunches are off axis. The evolution of the transverse position for the $n^{\rm th}$ bunch X_n in a bunch train is

$$\left(\frac{d}{dz}\gamma\frac{d}{dz} + \gamma k_{\beta n}^2\right) X_n = N_b r_e \sum_{j=1}^{n-1} \hat{W}_{\perp 1}\left((n-j)l\right) X_j(z) \,, \tag{3.37}$$

where N_b is the number of electrons per bunch, l is the bunch spacing, $r_e = e^2/(m_e c^2)$ is the classical electron radius, X_j is the displacement of the $j^{\rm th}$ bunch, and $\hat{W}_{\perp 1}$

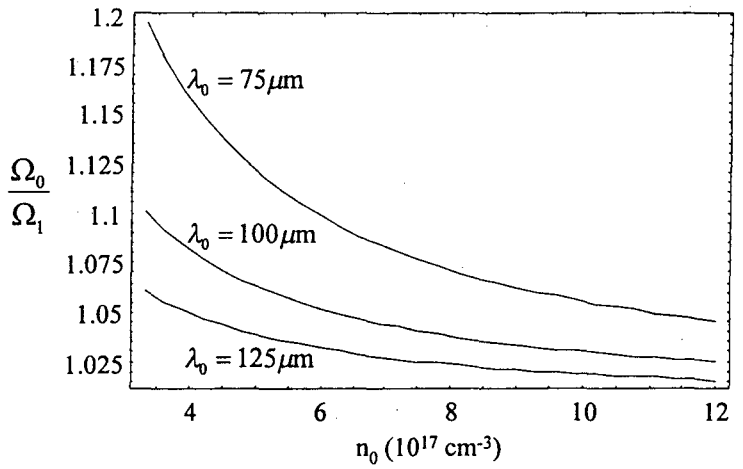

Figure 3.1: Ratio of dipole mode wavelength to fundamental mode wavelength Ω_0/Ω_1 versus plasma density for constant accelerating mode wavelengths $\lambda_0 = 75$ μm, 100 μm, and 125 μm.

is the transverse dipole wakefunction Eq. (3.4). Considering a two bunch model, the growth of the transverse position due to the trailing bunch coupling with the transverse wakefield of the head bunch in an excited hollow plasma channel ($g > 0$) without external focusing ($k_\beta \simeq 0$), scales as $X_2 \sim (z/L_{\rm m})$, with the characteristic growth length $L_{\rm m} = g[Nr_e\hat{W}_{\perp 1}(l)]^{-1}$. If external focusing is applied such that $k_\beta(z) = k_0(\gamma_0/\gamma)^\alpha$, then the growth of the transverse displacement of the second bunch scales as $X_2 \sim (z/L_{\rm mf})^{(3\alpha-1)/2}$, with the characteristic growth length $L_{\rm mf} = (\gamma_0/g)\{2\alpha k_0 g/[Nr_e\hat{W}_{\perp 1}(l)]\}^{2/(3\alpha-1)}$.

One possible method to reduce multi-bunch beam breakup growth is to tune the transverse dipole mode to place the bunches at the zero crossings [56] of the wakefunction Eq. (3.4). In other words, choose the bunch spacing l such that $\hat{W}_{\perp 1} \propto \sin(\Omega_1\omega_p l/c) = 0$. This will be possible if the ratio of the accelerating mode frequency to dipole mode frequency is tuned such that $q\Omega_0 = 2p\Omega_1$, where p and q are integers. Figure 3.1 shows the ratio of Ω_0/Ω_1 versus plasma density for several

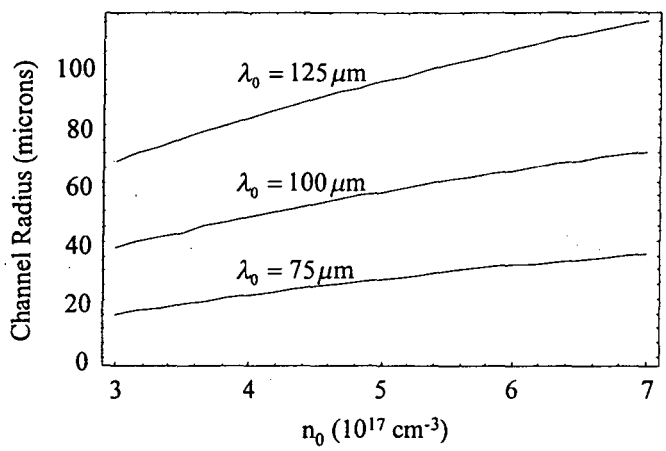

Figure 3.2: Channel radius as a function of plasma density which maintains constant accelerating frequency for fundamental mode wavelengths $\lambda_0 = 75$ μm, 100 μm, and 125 μm.

fixed values of the accelerating wavelength $\lambda_0 = \Omega_0^{-1} 2\pi c/\omega_p$.

Control of beam breakup can also be achieved by stagger-tuning [57, 58]. These results indicate a path to stagger-tuning for the plasma channel accelerator. The mode frequencies are functions of two independent experimental parameters: the channel radius and the plasma frequency. Therefore these two parameters can be varied such that the higher-order mode frequencies vary over the length of the accelerator while maintaining a constant fundamental (accelerating) mode frequency. This variation of the higher-order mode frequencies will avoid resonance with the dipole mode, which is responsible for beam breakup growth. Shown in Fig. 3.2 is the channel radius as a function of plasma density which maintains a constant accelerating frequency.

Regime	Exponent	Growth Length
Weak-focusing in excited channel	$\left(\frac{z}{L_{\rm w}}\right)^{1/4}$	$L_{\rm w} = 2^{-7}\frac{I_\varrho}{I}\frac{gR^2}{\kappa_1(\omega_p\tau)^2}$
Weak-focusing in unexcited channel	$\left(\frac{z}{L_{\rm wu}}\right)^{1/2}$	$L_{\rm wu} = 2^{-5/2}\left[\frac{I_\varrho}{I}\frac{\gamma_0 R^2}{\kappa_1(\omega_p\tau)^2}\right]^{1/2}$
Strong-focusing in excited channel	$\left(\frac{z}{L_{\rm s}}\right)^{\alpha/3}$	$L_{\rm s} = \frac{2^{5/\alpha}}{3^{9/2\alpha}}\left[\frac{I_\varrho}{I}\frac{\alpha\gamma_0^\alpha k_0 R^2}{g^{\alpha-1}\kappa_1(\omega_p\tau)^2}\right]^{1/\alpha}$
Strong-focusing in unexcited channel	$\left(\frac{z}{L_{\rm su}}\right)^{1/3}$	$L_{\rm su} = \frac{2^5}{3^{9/2}}\frac{I_\varrho}{I}\frac{k_\beta\gamma_0 R^2}{\kappa_1(\omega_p\tau)^2}$

Table 3.1: Exponents and growth lengths for single-bunch transverse beam breakup instabilities of a particle beam in a hollow plasma channel. Growth lengths are given for beam propagation in an excited channel (for an accelerating or witness beam) and in an unexcited channel (for a coasting or drive beam) in the weak-focusing (without external focusing) and strong-focusing (with external focusing) regimes.

3.5 Summary

In this chapter, the stability of a particle beam propagating in a hollow plasma channel was examined. Section 3.2 addressed the coupling of the dipole wakefield excited in the plasma channel to the transverse displacement of the beam. Single-bunch beam breakup was analyzed for accelerating and coasting beam propagation in a hollow plasma channel in the weak-focusing and strong-focusing regimes. The effects of longitudinal wakefields on energy spread (beam loading) were examined in Sec. 3.3. Multi-bunch transverse beam breakup was discussed in Sec. 3.4, and methods for reducing the multi-bunch beam breakup were proposed.

The exponents and characteristic growth lengths of the transverse beam centroid displacement due to single-bunch beam breakup instabilities are reviewed in Table 3.1. The table presents results for beam propagation in an excited hollow plasma channel (for an accelerating or witness beam) and in an unexcited hollow plasma channel (for a coasting or drive beam) in both the weak-focusing (without

external focusing) and strong-focusing (with external focusing) regimes. One can see from Table 3.1 that the most favorable scalings can be achieved for beams propagating in an excited hollow plasma channel in the strong-focusing regime.

With diffraction overcome by a plasma channel, the most severe limitation to the length of a single accelerator stage based on the hollow plasma channel structure is the transverse stability of the particle beam (i.e., $L_{\rm w} < L_{\rm dephase} < L_{\rm deplete}$ for typical parameters of plasma-based accelerator experiments). Such a plasma structure (a hollow plasma channel of length $\sim L_{\rm w}$) would be an extremely compact accelerator producing GeV-energy particle beams.

Chapter 4

Ultrashort Electron Bunch Generation

In this chapter, a laser-plasma-based relativistic electron source which uses laser-triggered injection of electrons is examined. The source generates ultrashort electron bunches by dephasing and trapping background plasma electrons undergoing fluid oscillations in an excited plasma wave. The plasma electrons are dephased by colliding two counter-propagating laser pulses which generate a slow phase velocity beat wave. In Sec. 4.2 the threshold laser pulse amplitudes, the optimal injection phase for trapping, and the trapping volume are calculated using a Hamiltonian approach. In Sec. 4.3 numerical simulation results from a three-dimensional particle transport code are presented which verify the analytic predictions and characterize the dynamics and quality of the generated electron bunches. This analysis indicates that the colliding laser pulse injection scheme has the capability to produce relativistic femtosecond electron bunches with fractional energy spread of order a few percent and normalized transverse emittance less than 1 mm mrad using 1 terawatt injection laser pulses.

4.1 Introduction

The characteristic scale length of the accelerating field (plasma wave) in a plasma-based accelerator is the plasma wavelength $\lambda_p(\mathrm{m}) = 2\pi c/\omega_p \simeq 3.3 \times 10^4\ n_e^{-1/2}(\mathrm{cm}^{-3})$. In such short wavelength accelerators (typically $\lambda_p \lesssim 100\ \mu\mathrm{m}$), production of electron beams with low momentum spread and good pulse-to-pulse energy stability requires femtosecond electron bunches to be injected with femtosecond synchronization with respect to the plasma wave. Although conventional electron sources (photocathode or thermionic guns) have achieved subpicosecond electron bunches [59, 60, 61], the requirements for injection into plasma-based accelerators are currently beyond the performance of these conventional electron sources.

Optical injection schemes which rely on laser-triggered injection of plasma electrons into a plasma wave have been proposed [62, 63] to generate the required femtosecond electron bunches. One method [62, 64] utilizes two laser pulses which propagate perpendicular to one another. One (injection) laser pulse intersects the plasma wave generated by the other (drive) laser pulse. The ponderomotive force due to the transverse gradient in the laser intensity of the injection laser pulse accelerates a fraction of the plasma electrons and allows them to be trapped by the plasma wave. One disadvantage of this method of dephasing background electrons is the high laser intensities ($> 10^{18}$ W/cm^2) required in the two laser pulses. Consequently, large space-charge waves are excited by the injection laser pulse which further complicates the injection process [64].

In this Chapter, an optical injection scheme [63, 65, 66] which uses three short laser pulses is examined. In this scheme, two low-intensity injection laser pulses are utilized as well as a pump laser pulse for plasma wave excitation. The pump laser pulse generates a plasma wave through its ponderomotive force, as in the standard laser wakefield accelerator. The two injection laser pulses, one pulse propagating in the forward direction behind the pump laser pulse and the other pulse counter-propagating to the pump laser pulse, collide at a predetermined phase of the plasma

wave. During this collision, the beating of the injection laser pulses generates a beat wave that interacts with a subset of the background plasma electrons. Under appropriate conditions, described in this chapter, some of the background plasma electrons attain sufficient momentum and phase-shift to be trapped by the plasma wave.

The trapping mechanism of this colliding laser pulse scheme is somewhat analogous to the self-trapping process that can occur in the self-modulated laser wakefield accelerator [67]. Self-trapped electrons with energies as high as 100 MeV have been observed in self-modulated laser wakefield accelerator experiments [17, 18, 68]. In addition to producing a large plasma wave via self-modulation, a long pulse length laser ($L > \lambda_p$, where L is the laser pulse length) decays into Raman backscattered light and a plasma wave. The backscattered light can beat with the pump pulse, generating a slow phase velocity beat wave, and accelerating background plasma electrons to sufficient energies so as to be trapped by the plasma wave [67, 69]. The drawback of using self-modulation of the pump laser pulse as an electron source is that it produces electron bunches with near 100% energy spread [17, 18, 68]. This is the case since the slow beat wave is not localized with respect to the phase of the plasma wave (i.e., the beat wave extends over distances much larger than the plasma wavelength). Furthermore, self-modulation relies on instabilities, i.e., trapping and acceleration occur in an uncontrolled manner.

In contrast to other optical injection schemes, the colliding laser pulse scheme has the potential to produce femtosecond electron bunches with low fractional energy spreads ($\sim 1\%$) using relatively low injection laser pulse intensities compared to the pump laser pulse $a_{\text{inj}}^2 \ll a_{\text{pump}}^2 \sim 1$. Furthermore since $L \lesssim \lambda_p$ for the three laser pulses considered in this scheme, Raman instabilities will be suppressed. The colliding pulse concept also offers detailed control of the injection process. The injection phase is determined by the relative timing between the forward propagating injection laser pulse and the pump laser pulse. The beat wave phase velocity is adjusted by varying the frequency detuning between the injection laser pulses, and the

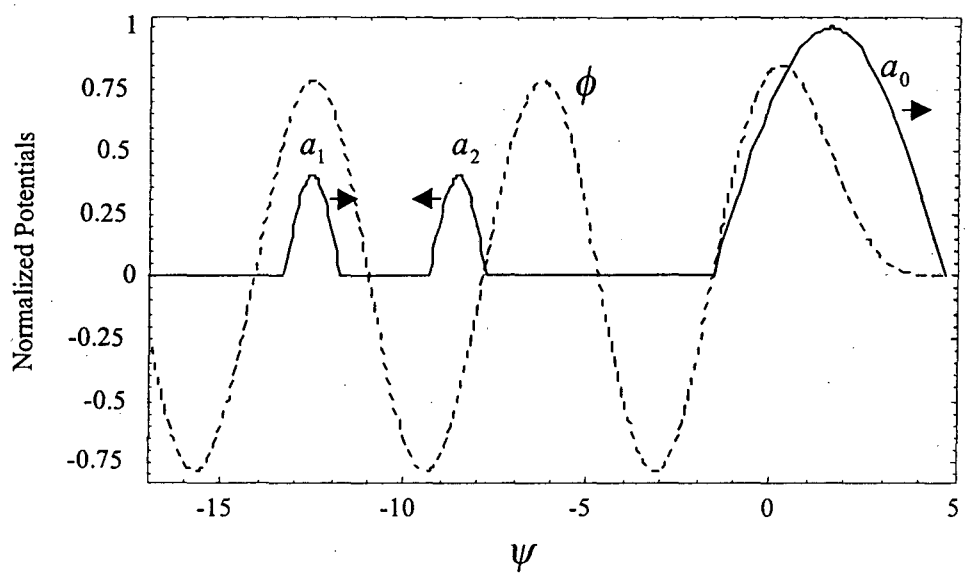

Figure 4.1: Normalized axial potential profiles of the pump laser pulse a_0, the plasma wave ϕ, the forward injection laser pulse a_1, and the backward injection laser pulse a_2.

number of trapped electrons can be controlled by the injection laser pulse intensities and durations.

4.2 Phase Space Analysis

The colliding laser pulse optical injection scheme employs three short laser pulses as illustrated in Fig. 4.1: an intense ($a_0^2 \lesssim 1$) laser pulse (denoted by subscript 0) for plasma wave generation, a forward propagating injection laser pulse (subscript 1), and a backward propagating injection laser pulse (subscript 2). The pump laser pulse generates a plasma wave with phase velocity near the speed of light $v_\varphi \simeq c$. The injection laser pulses collide some distance behind the pump laser pulse. When the injection laser pulses collide, they generate a beat wave with a phase velocity

$v_b = \Delta\omega/\Delta k \simeq \Delta\omega/2k_0$, where the frequency difference of the injection laser pulses is $\Delta\omega = \omega_1 - \omega_2$ and the wavenumber difference is $\Delta k = k_1 - k_2 \simeq 2k_0$ with $k_1 \simeq |k_2| \simeq k_0$. During the time when the two injection laser pulses overlap, the slow beat wave injects plasma electrons into the fast plasma wave for acceleration to high energies. Note that the polarizations of the injection laser pulses can be chosen to be orthogonal to the pump laser pulse such that there is no interaction between the pump laser pulse and the backward propagating injection laser pulse.

An example of the colliding laser pulse injection process is shown in Fig. 4.2, which presents simulation results of the evolution in longitudinal phase space of an initially uniform segment of electrons as they interact with the plasma wave and the beating injection laser pulses. This figure was generated using a particle transport code described in Sec. 4.3. Also shown is the separatrix (solid line) between the trapped and untrapped orbits of the plasma wave Hamiltonian. Figure 4.2 shows the electron distribution (a) before the collision of the injection laser pulses (in an untrapped orbit of the plasma wave), (b) during the collision of the injection laser pulses (crossing the plasma wave separatrix), (c) just after the collision (0.07 mm of propagation after the collision), and (d) the resulting energetic electron bunch (0.7 mm of propagation after the collision).

4.2.1 Plasma Wave Hamiltonian

The colliding laser pulse injection mechanism can be studied using a Hamiltonian approach. The electron motion in a one-dimensional plasma wave is described by the Hamiltonian

$$H(u_z, \psi) = \left(1 + u_z^2\right)^{1/2} - \beta_\varphi u_z - \phi(\psi) \,, \tag{4.1}$$

with the corresponding Hamilton equations

$$\frac{d\psi}{d\hat{t}} = \frac{\partial H}{\partial u_z} = \frac{u_z}{\sqrt{1+u_z^2}} - \beta_\varphi \tag{4.2}$$

$$\frac{du_z}{d\hat{t}} = -\frac{\partial H}{\partial \psi} = \frac{\partial \phi}{\partial \psi} \,, \tag{4.3}$$

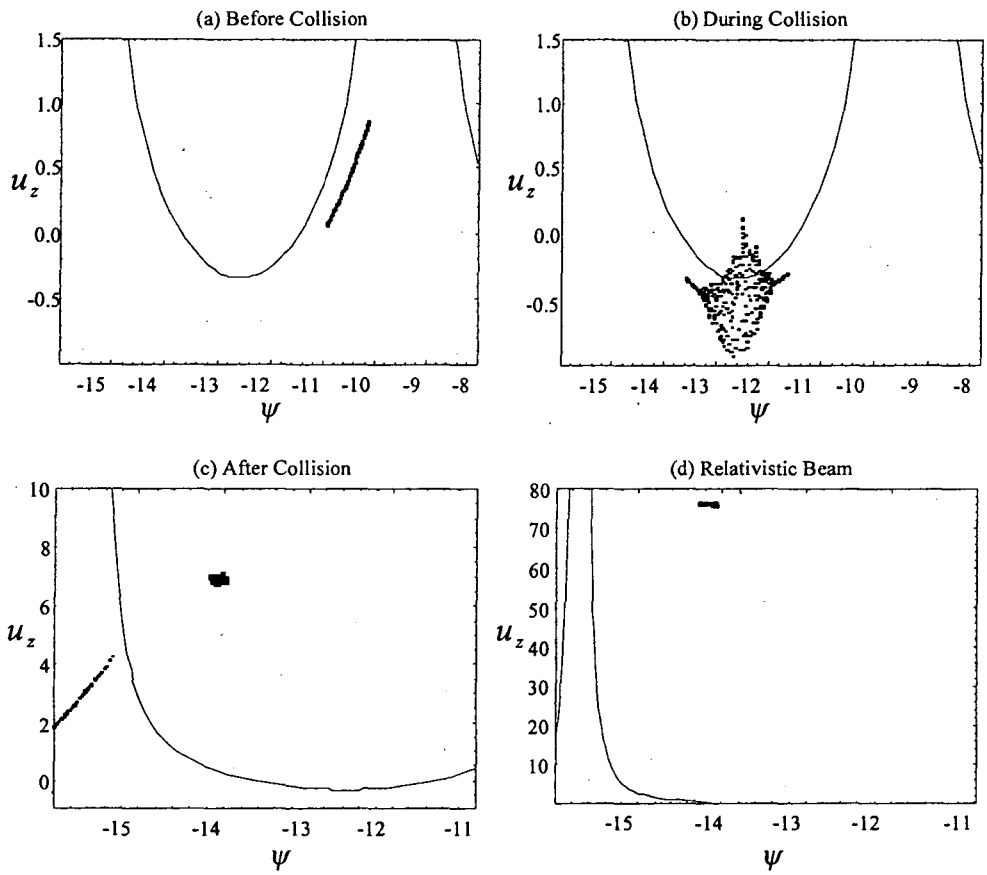

Figure 4.2: Electron distribution in longitudinal phase space (ψ, u_z) (a) before the collision of injection laser pulses ($\omega_p t = 36$), (b) during the collision of injection laser pulses ($\omega_p t = 39$), (c) just after the collision ($\omega_p t = 50$), and (d) an energetic electron beam ($\omega_p t = 150$). The separatrix between trapped and untrapped plasma wave orbits (solid line) is shown.

where $u_z m_e c$ is the electron axial momentum and $c\beta_\varphi$ is the plasma wave phase velocity, which is near the group velocity of the pump laser pulse $v_g \simeq c\beta_\varphi$. Here the independent variable $\hat{t} = \beta_\varphi^{-1}\omega_p t$ has been used. The scalar potential of the plasma wave is assumed to have the form $\phi(\psi) = \phi_o \cos\psi$, where the plasma wave phase is $\psi = \omega_p(z - \beta_\varphi ct)/(c\beta_\varphi)$ and the normalized plasma wave potential amplitude is $\phi_o = e\Phi_o/m_e c^2$. The amplitude of the plasma wave potential is determined by the pump laser pulse amplitude and shape. The normalized axial momentum in an orbit of the plasma wave ($H =$ constant) is

$$u_z = \beta_\varphi \gamma_\varphi^2 \left[H + \phi(\psi)\right] \pm \gamma_\varphi \sqrt{\gamma_\varphi^2 \left[H + \phi(\psi)\right]^2 - 1}\,, \tag{4.4}$$

where $\gamma_\varphi = (1 - \beta_\varphi^2)^{-1/2}$. Assuming the plasma is initially cold, the background electron fluid motion in the plasma wave is defined by the orbit $H = 1$.

The boundary between trapped and untrapped orbits is given by the separatrix orbit $H = H(u_z = \gamma_\varphi\beta_\varphi, \psi = \pi) = \gamma_\varphi^{-1} + \phi_o$. The maximum momentum of an electron in a trapped orbit of the plasma wave $u_{\max}$ is given by the maximum momentum of the separatrix $H(u_{\max}, 2\pi) = H(\gamma_\varphi\beta_\varphi, \pi)$,

$$u_{\max} = \beta_\varphi\gamma_\varphi\left(1 + 2\phi_o\gamma_\varphi\right) + \gamma_\varphi\left[\left(1 + 2\phi_o\gamma_\varphi\right)^2 - 1\right]^{1/2}\,. \tag{4.5}$$

In the limits $\gamma_\varphi\phi_o \gg 1$ and $\gamma_\varphi^2 \gg 1$, the maximum energy of an electron in a trapped orbit is $\gamma_{\max} \simeq 4\gamma_\varphi^2\phi_o$.

The one-dimensional Hamiltonian Eq. (4.1) neglects the effects of transverse focusing. A three-dimensional plasma wave will have a periodic radial field which is $\pi/2$ out of phase with the accelerating field. Therefore, there exists a $\pi/4$ region in phase where the fields due to the plasma wave are both focusing and accelerating. For an electron to be trapped and remain in this region where the transverse electric field due to the plasma wave will provide a focusing force, it must be in an orbit with $H \leq H(u_z = \gamma_\varphi\beta_\varphi, \psi = \pi/2) = \gamma_\varphi^{-1}$.

4.2.2 Beat Wave Hamiltonian

The colliding injection laser pulses lead to the formation of a beat wave with phase space buckets (separatrices) of width $2\pi/\Delta k \simeq \lambda_0/2$ (much shorter than those of the plasma wave field λ_p, i.e., $\lambda_0 \ll \lambda_p$ is assumed). The motion of the electron in the beat wave is described by the beat wave Hamiltonian

$$H_b(u_z, \psi_b) = \left[\gamma_\perp^2(\psi_b) + u_z^2\right]^{1/2} - \beta_b u_z \,, \tag{4.6}$$

with the corresponding Hamilton equations

$$\frac{d\psi_b}{d\hat{t}_b} = \frac{\partial H_b}{\partial u_z} = \frac{u_z}{(\gamma_\perp^2 + u_z^2)^{1/2}} - \beta_b \tag{4.7}$$

$$\frac{du_z}{d\hat{t}_b} = -\frac{\partial H_b}{\partial \psi_b} = \frac{1}{(\gamma_\perp^2 + u_z^2)^{1/2}} \frac{1}{2} \frac{\partial \gamma_\perp^2}{\partial \psi_b} \,, \tag{4.8}$$

where $\beta_b = \Delta\omega/c\Delta k \simeq (\lambda_2 - \lambda_1)/(\lambda_2 + \lambda_1)$ is the beat wave phase velocity, $\psi_b = \Delta k(z - \beta_b ct)$ is the beat wave phase, and the independent variable $\hat{t}_b = \Delta kct$ has been used. Here $\gamma_\perp^2(\psi_b) = 1 + \hat{a}_1^2 + \hat{a}_2^2 + 2\hat{a}_1\hat{a}_2 \cos\psi_b$ with $\hat{a}_1^2$ and $\hat{a}_2^2$ the slowly varying amplitudes of the forward and backward injection laser pulses averaged over the rapid phase oscillations. The separatrix orbit in phase space of the beat wave Hamiltonian has the value $H_b = H_b(u_z = \gamma_b\beta_b\gamma_\perp(0), \psi_b = 0) = \gamma_\perp(0)\gamma_b^{-1}$, where $\gamma_b = (1 - \beta_b^2)^{-1/2}$. The maximum (+) and minimum (−) normalized axial momenta of an electron in a beat wave orbit (extrema of the separatrix) are

$$u_{\text{beat}} = \gamma_b\beta_b\gamma_\perp(0) \pm 2\gamma_b(\hat{a}_1\hat{a}_2)^{1/2} \,. \tag{4.9}$$

The beat wave amplitude parameter $(\hat{a}_1\hat{a}_2)^{1/2}$ (the geometrical mean of the normalized vector potential amplitudes of the two injection laser pulses) is a critical parameter in the injection process. For $\hat{a}_1 = \hat{a}_2 = \hat{a}_{\text{inj}}$ the beat wave amplitude parameter $(\hat{a}_1\hat{a}_2)^{1/2} = \hat{a}_{\text{inj}} = eE_{\text{inj}}/(m_e c\omega_{\text{inj}})$ is the normalized root-mean-squared (rms), averaged over a laser period, electric field amplitude of the injection laser pulses.

From the beat wave Hamiltonian, it can be shown that the bounce period for an electron deeply trapped in the beat wave is given by

$$\tau_b = \left(\frac{2\pi}{c\Delta k}\right) \frac{\gamma_b^2 \gamma_\perp(\pi)}{\sqrt{\hat{a}_1 \hat{a}_2}} \,. \tag{4.10}$$

This bounce time is typically much shorter than the transit time $\sim \lambda_p/c$ of a plasma electron through a single period of the plasma wave. Since the transit time of an untrapped electron through a beat wave orbit $\sim \lambda_0/(2c)$ and the bounce time of a deeply trapped electron in a beat wave orbit τ_b are both much shorter than a plasma wave period, a separation of time scales is possible. This difference in time scales is due to the extremely small spatial scale $\lambda_0/2$ of the beat wave orbits in comparison to the plasma wave orbit λ_p. Therefore, on the time scale in which a single electron interacts with a beat wave orbit, it can be assumed that the electron experiences a constant electric field from the plasma wave. The effect of the plasma wave electric field on the phase space orbits is to distort the beat wave orbits.

Within a single period of the beat wave, the plasma wave electric field $E_z = -(m_e c^2/e)\partial_z \phi$ can be approximated as a constant. That is, for small phase excursions $|\Delta\psi| \ll 2\pi$ about ψ_o, $E_z(\psi) \simeq E_z(\psi_o)$, where ψ_o is the local plasma wave phase position of the beat wave bucket and $E_z(\psi_o)$ is the local value of the plasma wave axial electric field. The modification of the beat wave Hamiltonian Eq. (4.6) to include the presence of the plasma wave E_z can then be written as

$$H_b(u_z, \psi_b) = \left[\gamma_\perp^2(\psi_b) + u_z^2\right]^{1/2} - \beta_b u_z + \epsilon\psi_b \,, \tag{4.11}$$

where $\epsilon = eE_z(\psi_o)/(m_e c^2 \Delta k)$ is constant.

Equation (4.11) describes the distortion of the (u_z, ψ_b) phase space from symmetric islands ($\epsilon = 0$) to "fish-shaped" islands ($\epsilon \neq 0$) as shown in Fig. 4.3. When $\epsilon = 0$, the separatrix is symmetric in ψ_b about the stable fixed point, e.g., located at $\psi_b = -\pi$, with unstable fixed points located at $\psi_b = 0, -2\pi$. When $\epsilon \neq 0$, the separatrix is fish-shaped and the enclosed region of phase space is reduced (compared with $\epsilon = 0$) and lies inside the region $-2\pi < \psi_b < 0$. For example, when

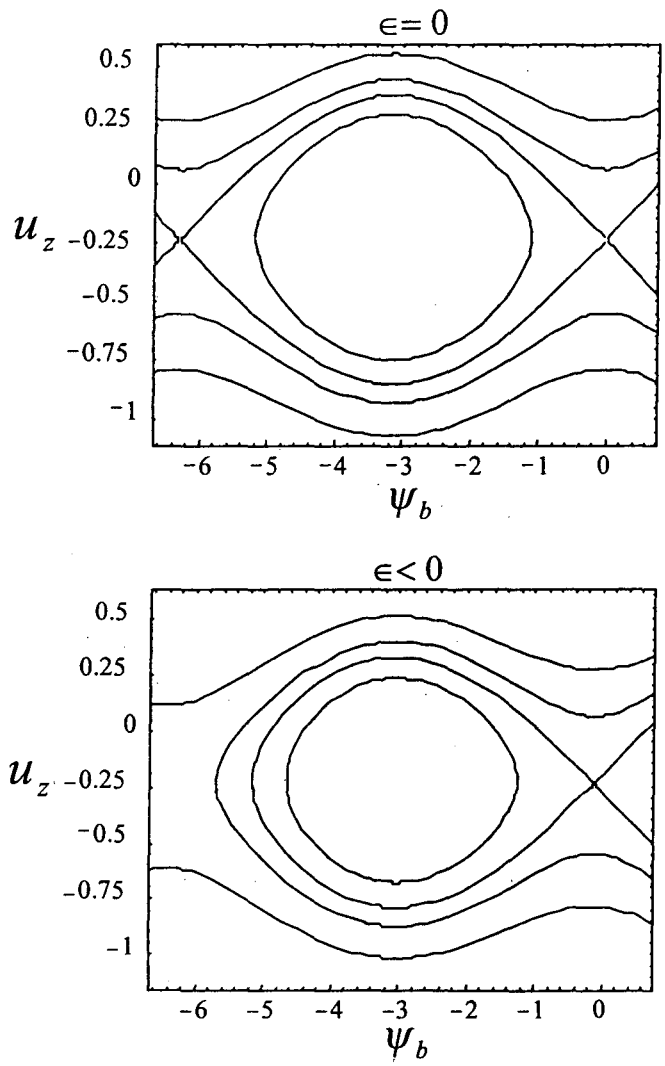

Figure 4.3: Distortion of the beat wave orbits in phase space (ψ_b, u_z) due to the presence of the plasma wave $\epsilon = eE_z(\psi_o)/(m_e c^2 \Delta k)$. With $\epsilon < 0$, the buckets open to the right.

$\epsilon < 0$, the "fish-tail" of the separatrix opens to the right, i.e., the unstable fixed point lies to the left of $\psi_b = 0$. In the limit $\pi|\epsilon|\gamma_b\gamma_\perp(0)/(2\hat{a}_0\hat{a}_1) < 1$, the maximum and minimum axial momenta for an electron on the separatrix are

$$u_{\rm beat} \simeq \beta_b\gamma_b\Big[\gamma_\perp(0) - \pi|\epsilon|\gamma_b\Big] \pm 2\gamma_b(\hat{a}_0\hat{a}_1)^{1/2}\left[1 - \frac{\pi|\epsilon|\gamma_b\gamma_\perp(0)}{2\hat{a}_0\hat{a}_1}\right]^{1/2} . \qquad (4.12)$$

Both the width and height of the separatrix decrease with increasing $|\epsilon|$ (i.e., increasing plasma wave amplitude).

The electron fluid momentum in the plasma wave is given by Eq. (4.4) with $H = 1$. For $\gamma_\varphi^2 \gg 1$, the normalized electron fluid momentum is

$$u_z \simeq -\frac{\phi_0\cos(\psi)}{[1+\phi_0\cos(\psi)]}\left[1 + \frac{\phi_0}{2}\cos(\psi)\right] . \qquad (4.13)$$

Trapping may occur by the following method. In the region $-\pi/2 < \psi < 0$, the plasma electrons are flowing backward ($u_z < 0$) and the electric field is accelerating ($E_z < 0$). If $E_z < 0$, then $\epsilon < 0$ and the beat wave orbits open to the right, as shown in Fig. 4.3. Consider an electron initially flowing backward, as it would in the region $-\pi/2 < \psi < 0$, thus initially residing below the beat wave separatrix. As Fig. 4.3 indicates, the orbits are open and can take an electron from below to above the beat wave separatrix. Such an electron would acquire a positive axial momentum which is sufficiently high to be trapped and accelerated by the plasma wave. The open phase space orbits provide a possible path by which the ponderomotive beat wave can lead to trapping of electrons in the plasma wave.

4.2.3 Trapping Threshold

The threshold injection laser pulse intensities required for trapping of background plasma electrons into the plasma wave can be estimated by considering the effects of the plasma wave and the beat wave individually and requiring resonance overlap (illustrated in Fig. 4.4). Specifically, that the maximum momentum of the beat wave separatrix exceeds the minimum momentum of the plasma wave separatrix and the minimum momentum of the beat wave separatrix is less than the fluid

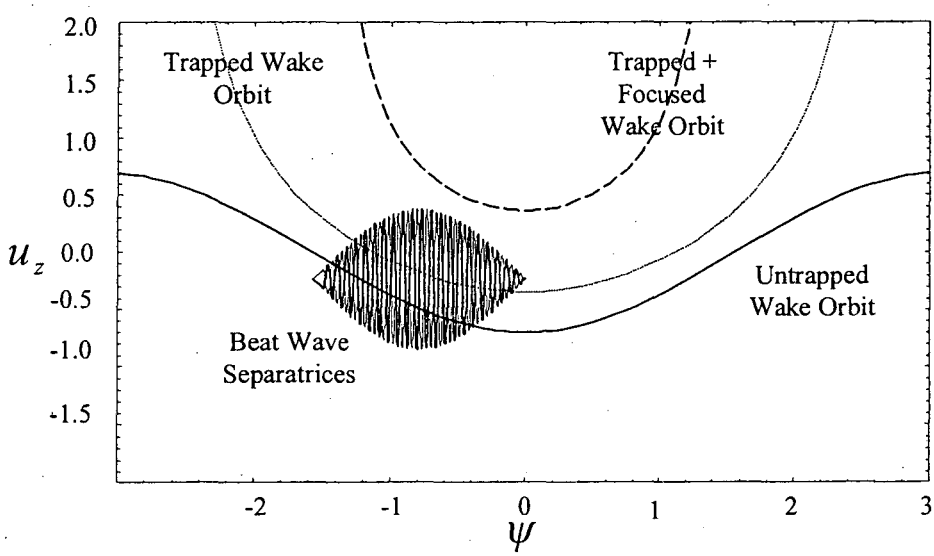

Figure 4.4: Phase space (ψ, u_z) showing the beat wave separatrices, an untrapped plasma wave orbit (solid line), a trapped plasma wave orbit (dotted line), and a trapped and focused plasma wave orbit (dashed line).

momentum of electrons in the plasma wave. With these requirements, the necessary conditions for trapping are

$$(u_{\rm beat})_{\rm max} \geq u_{\rm trap}, \tag{4.14}$$

$$(u_{\rm beat})_{\rm min} \leq u_{\rm untrap}\,. \tag{4.15}$$

The maximum and minimum momenta of an electron in a beat wave orbit are given in Eq. (4.9). The momentum of a plasma electron in an untrapped orbit of the plasma wave $u_{\rm untrap}$ is given by Eq. (4.4) with $H = 1$ (i.e., the background plasma fluid electrons). The momentum of an electron in a trapped orbit of the plasma wave $u_{\rm trap}$ is given by Eq. (4.4) with $H \leq \gamma_\varphi^{-1} + \phi_o$. For an electron in a trapped and focused orbit, $u_{\rm trap}$ is given by Eq. (4.4) with $H \leq \gamma_\varphi^{-1}$.

Solving for the minimum $(\hat{a}_1\hat{a}_2)^{1/2}$ which satisfies the conditions Eqs. (4.14) and (4.15) yields the threshold beat wave amplitude parameter for trapping plasma

electrons,

$$(\hat{a}_1\hat{a}_2)_{\rm th}^{1/2} = \frac{1-H}{4\gamma_b(\beta_\varphi - \beta_b)}\,, \tag{4.16}$$

and the optimal plasma wave phase for injection [plasma wave phase location where the threshold beat wave amplitude parameter Eq. (4.16) allows for trapping]

$$\cos\psi_{\rm opt} = \phi_o^{-1}\left[\gamma_b\left(1-\beta_\varphi\beta_b\right)\gamma_\perp(0) - \frac{1}{2}\left(1+H\right)\right]\,. \tag{4.17}$$

Here $H = \gamma_\varphi^{-1} + \phi_o$ for injection into a trapped plasma wave orbit and $H = \gamma_\varphi^{-1}$ for injection into a trapped and focused plasma wave orbit. In the limits $\gamma_\varphi^2 \gg 1$, $\beta_b \ll 1$, and $\hat{a}_i^2 \ll 1$, Eqs. (4.16) and (4.17) reduce to

$$4(\hat{a}_1\hat{a}_2)_{\rm th}^{1/2} \simeq (1+\beta_b)(1-H) \tag{4.18}$$

$$2\phi_o\cos\psi_{\rm opt} \simeq 1 - 2\beta_b - H\,, \tag{4.19}$$

with $H \simeq \phi_o$ for a trapped orbit and $H \simeq 0$ for a trapped and focused orbit. As an example, the parameters $\beta_b = -0.2$, $\gamma_\varphi = 50$, and $\phi_o = 0.7$ give a threshold of $(\hat{a}_1\hat{a}_2)_{\rm th}^{1/2} \simeq 0.2$ and an optimal injection phase of $\psi_{\rm opt} \simeq 0$ for injection into a trapped and focused orbit. Figure 4.5(a) shows the threshold beat wave amplitude parameter for trapping [Eq. (4.16) with $H = \gamma_\varphi^{-1} + \phi_o$] and Fig. 4.5(b) shows the optimal plasma wave phase for injection versus the beat wave phase velocity β_b for several plasma wave potential amplitudes. From Fig. 4.5(a) one sees that the larger the plasma wave, the smaller the injection laser pulse intensity required for trapping plasma electrons. The threshold for injection into a trapped and focused orbit is independent of plasma wave amplitude as indicated by Eq. (4.16) with $H = \gamma_\varphi^{-1}$. In the limit $\gamma_\varphi^2 \gg 1$, the threshold beat wave amplitude parameter for a trapped and focused orbit is $(\hat{a}_1\hat{a}_2)_{\rm th}^{1/2} \simeq 1/[4\gamma_b(1-\beta_b)] \leq 0.25$ for $\beta_b \leq 0$. Figure 4.5(a) also shows the threshold slightly decreases for decreasing β_b. Note that the estimate of the trapping threshold Eq. (4.16) will not be valid when the separation in time scales no longer applies, i.e., when $|\beta_b|$ is large enough such that $\tau_b \sim \lambda_p/c$, where τ_b is given by Eq. (4.10). Furthermore, validity of Eq. (4.17) requires $|\cos\psi_{\rm opt}| < 1$.

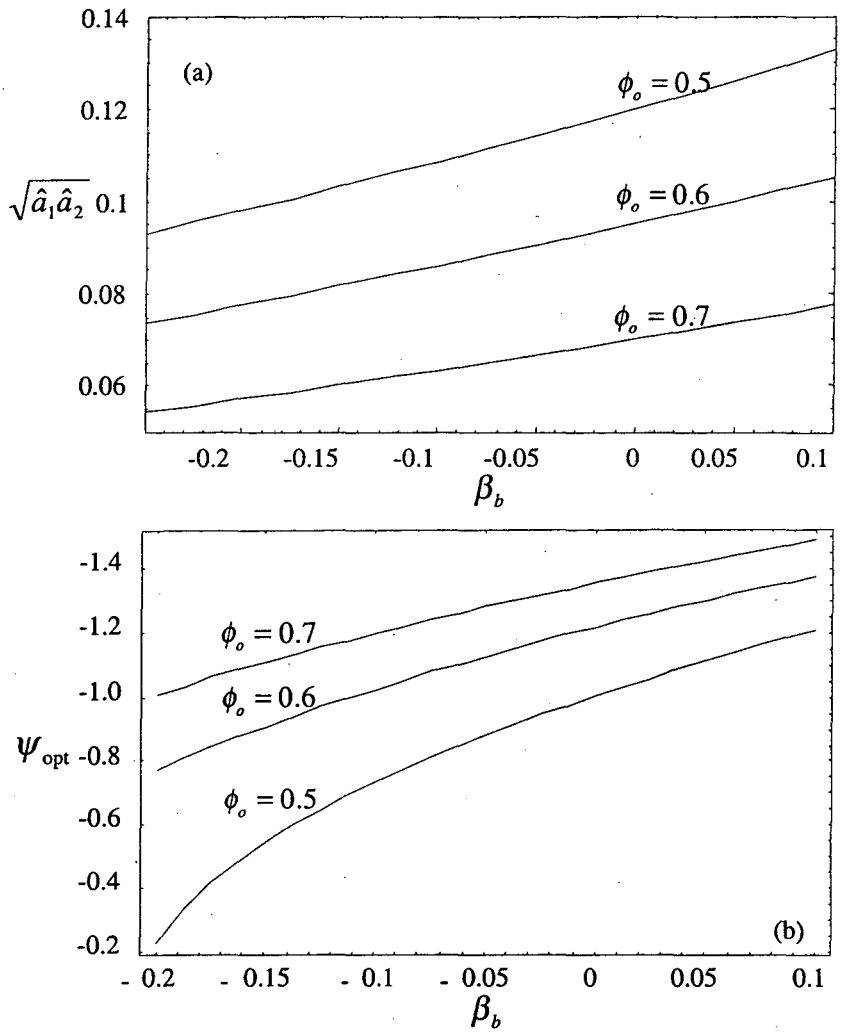

Figure 4.5: (a) The threshold beat wave amplitude parameter $(\hat{a}_1\hat{a}_2)_{\rm th}^{1/2}$ for trapping at the optimal injection phase versus beat wave phase velocity (for $\phi_o = 0.5$, 0.6, and 0.7). (b) The optimal plasma wave phase for injection $\psi_{\rm opt}$ versus beat wave phase velocity (for $\phi_o = 0.5$, 0.6, and 0.7).

Minimizing the injection pulse amplitudes [operating near the threshold amplitude given by Eq. (4.16)] will minimize the laser power $P_i \simeq 43(\hat{a}_i r_i/\lambda_i)^2$ GW required for trapping and is therefore important for the experimental realization of this optical injection scheme. For illustration, if the injection laser pulses have a wavelength of 0.8 μm and a spot size of 15 μm, then the injection laser pulse power required for trapping is $P_i \leq 1$ TW for $\hat{a}_i \leq 0.26$.

4.2.4 Trapping Volume

The region where trapping is possible (i.e., the plasma volume where the injection laser pulse amplitudes are greater than the threshold for moving an electron from an untrapped to a trapped orbit) can also be determined by examining the resonant overlap of phase space separatricies. Consider $(\hat{a}_1\hat{a}_2)^{1/2} > (\hat{a}_1\hat{a}_2)_{\rm th}^{1/2}$, where $(\hat{a}_1\hat{a}_2)_{\rm th}^{1/2}$ is defined by Eq. (4.16), such that the beat wave separatrix overlaps well both the untrapped plasma fluid orbit and the plasma wave separatrix. From Eq. (4.1), the momentum of trapped and untrapped electrons in the plasma wave satisfies the relations

$$H + \phi = \left[1 + u_{\rm trap}^2\right]^{1/2} - \beta_\varphi u_{\rm trap} \tag{4.20}$$

$$1 + \phi = \left[1 + u_{\rm untrap}^2\right]^{1/2} - \beta_\varphi u_{\rm untrap} \, , \tag{4.21}$$

where $H \leq \phi_o + \gamma_\varphi^{-1}$ for a trapped orbit and $H \leq \gamma_\varphi^{-1}$ for a trapped and focused orbit. To determine the region in plasma wave phase ψ where trapping is possible, consider the phase ψ_{t1}, where the maximum beat wave momentum equals the momentum of the plasma wave separatrix,

$$(u_{\rm beat})_{\rm max} = u_{\rm trap}(\psi_{t1}) \, , \tag{4.22}$$

and the phase ψ_{t2}, where the minimum beat wave momentum equals the fluid momentum,

$$(u_{\rm beat})_{\rm min} = u_{\rm untrap}(\psi_{t2}) \, . \tag{4.23}$$

The maximum and minimum momenta of the beat wave separatrix $u_{\rm beat}$ are given by Eq. (4.9). Applying these conditions Eqs. (4.22) and (4.23) to the plasma wave Hamiltonian relations Eqs. (4.20) and (4.21) yields

$$H + \phi(\psi_{t1}) = \left[1 + (u_{\rm beat})^2_{\rm max}\right]^{1/2} - \beta_\varphi (u_{\rm beat})_{\rm max} \tag{4.24}$$

$$1 + \phi(\psi_{t2}) = \left[1 + (u_{\rm beat})^2_{\rm min}\right]^{1/2} - \beta_\varphi (u_{\rm beat})_{\rm min} \, . \tag{4.25}$$

Solving for ψ_{t1} and ψ_{t2} yields

$$\cos\psi_{t1} = \phi_o^{-1}\left[\gamma_b\gamma_\perp(0)(1-\beta_\varphi\beta_b) - 2\gamma_b(\beta_\varphi - \beta_b)(\hat{a}_1\hat{a}_2)^{1/2} - H\right] \tag{4.26}$$

$$\cos\psi_{t2} = \phi_o^{-1}\left[2\gamma_b(\beta_\varphi - \beta_b)(\hat{a}_1\hat{a}_2)^{1/2} + \gamma_b\gamma_\perp(0)(1-\beta_\varphi\beta_b) - 1\right] \, . \tag{4.27}$$

Note that $|\psi_{t2}| \leq |\psi_{t1}|$ and $\psi_{t1} = \psi_{t2} = \psi_{\rm opt}$ when $(\hat{a}_1\hat{a}_2)^{1/2} = (\hat{a}_1\hat{a}_2)^{1/2}_{\rm th}$.

If the right-hand side (RHS) of Eq. (4.27) satisfies |RHS| < 1, then the plasma wave phase regions where trapping is possible are $-|\psi_{t1}| \leq \psi \leq -|\psi_{t2}|$ and $|\psi_{t2}| \leq \psi \leq |\psi_{t1}|$. If solutions to Eq. (4.27) do not exist [i.e., the RHS of Eq. (4.27) satisfies |RHS| > 1], then the minimum beat wave momentum is less than the fluid momentum for all plasma wave phases $(u_{\rm beat})_{\rm min} < u_{\rm untrap}(0)$, and the plasma wave phase region where trapping is possible is $-|\psi_{t1}| \leq \psi \leq |\psi_{t1}|$. These regions are correct for injection into a trapped orbit $H = \phi_o + \gamma_\varphi^{-1}$ [where solutions to Eq. (4.27) exist for typical parameters] and for injection into a trapped and focused orbit $H = \gamma_\varphi^{-1}$ [where the RHS of Eq. (4.27) satisfies |RHS| > 1 for typical parameters].

Assuming $k_p r_i > 1$, where r_i are the minimum spot sizes of the laser pulses, such that the radial motion of the electrons in the plasma wave remains small, the above one-dimensional Hamiltonian theory can be used to estimate the initial trapping volume. The plasma wave phase region where trapping is possible is a function of the radial position of the electrons via Eqs. (4.26) and (4.27) and the generalizations $\hat{a}_i(r) = \hat{a}_i \exp(-r^2/r_i^2)$ and $\phi_o(r) = \phi_o \exp(-2r^2/r_0^2)$. Here we have assumed Gaussian radial profiles of the laser pulses. Figure 4.6 shows the region $(\psi, r(\psi))$ where trapping of plasma electrons is possible for the parameters given in

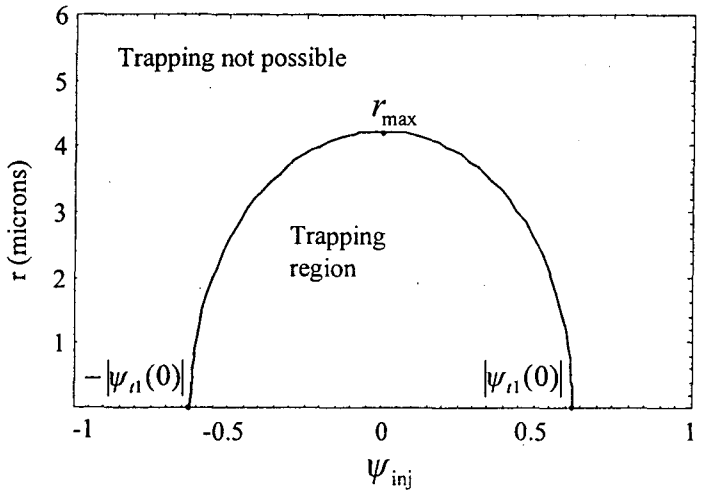

Figure 4.6: Region in (ψ, r) where trapping of plasma electrons is allowed for parameters in Table 4.1.

Table 4.1. In Fig. 4.6, the maximum radial position where trapping is possible $r_{\max}$ is $r_{\max} = 4.2$ μm, and the length of the phase region where trapping is possible $L_{\rm trap} = \omega_p^{-1} c(2|\psi_{t1}(0)|)$ is $L_{\rm trap} = 7.9$ μm. The volume where trapping is allowed can be calculated by

$$V_{\rm trap} = \int \pi r^2(\psi) d\psi \, . \tag{4.28}$$

The trapping volume for the case illustrated in Fig. 4.6 is $V_{\rm trap} \simeq 3.0 \times 10^{-10}$ cm^{-3}.

With the trapping region known, one can choose the injection laser pulse lengths to be greater than the phase region where trapping is possible, $L_i > L_{\rm trap}$, thereby maximizing the number of electrons trapped. Figure 4.7 shows the length of the plasma wave phase region $L_{\rm trap}$ (solid line) and the maximum radial position $r_{\max}$ (dashed line) versus beat wave amplitude parameter for the parameters in Table 4.1.

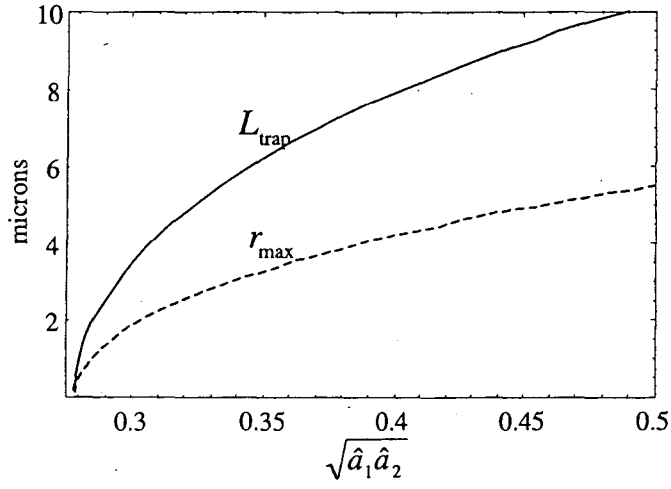

Figure 4.7: The length of the plasma wave phase region L_{trap} (solid line) and the maximum radial position r_{max} (dashed line) where trapping is possible versus beat wave amplitude parameter $(\hat{a}_1\hat{a}_2)^{1/2}$.

Plasma wavelength λ_p	40 μm
Pump laser strength $\hat{a}_0$	0.94
Plasma wave potential ϕ_o	0.7
Pump pulse length $L_0 = \lambda_p$	40 μm
Pump pulse wavelength λ_0	0.8 μm
Laser spot size $r_0 = r_1 = r_2$	15 μm
Injection laser pulse strength $\hat{a}_1 = \hat{a}_2$	0.4
Injection pulse length $L_1 = L_2 = \lambda_p/2$	20 μm
Injection pulse (forward) wavelength λ_1	0.83 μm
Injection pulse (backward) wavelength λ_2	0.80 μm

Table 4.1: Colliding pulse optical injection parameters used in the numerical simulations presented in Sec. 4.3.

4.3 Numerical Studies

To further evaluate the colliding laser pulse optical injection scheme and to test the analytic predictions for the trapping thresholds presented in Sec. 4.2, the motion of test particles in the combined plasma wave and laser fields was simulated by numerically solving the equations of motion for the electrons. In the numerical simulations, we assume the laser pulses are linearly polarized with fundamental Gaussian radial profiles and half-period cosine longitudinal envelopes. In the paraxial approximation ($\lambda_i \ll r_i$, where λ_i is the laser wavelength and r_i is the minimum laser spot size) the normalized vector potential of the laser pulses is $\vec{a}_i = \hat{e}_{\perp i} a_{\perp i} + \hat{e}_z a_{zi}$ where $\hat{e}_{\perp i}$ and $\hat{e}_z$ are unit vectors and the vector potential components are given by [70]

$$a_{\perp i} = \sqrt{2}\hat{a}_i \frac{r_i}{r_{si}} e^{(-r^2/r_{si}^2)} \cos\psi_i \tag{4.29}$$

$$a_{zi} = 2\sqrt{2}\hat{a}_i \frac{(\vec{x}\cdot\hat{e}_{\perp i}) r_i}{k_i r_{si}^3} e^{(-r^2/r_{si}^2)} \left(\sin\psi_i - \frac{z}{Z_{Ri}}\cos\psi_i\right) . \tag{4.30}$$

Here $\omega_i = 2\pi c/\lambda_i$ is the laser frequency, $r_{si}(z) = r_i(1 + z^2/Z_{Ri}^2)^{1/2}$ is the laser spot size, $Z_{Ri} = k_i r_i^2/2$ is the Rayleigh length, and $\psi_i = k_i(z - \beta_{\varphi i} ct) + zr^2/(r_{si}^2 Z_{Ri}) + z/Z_{Ri} - \tan^{-1}(z/Z_{Ri}) + \varphi_i$ is the phase with φ_i a constant. The phase velocity $c\beta_{\varphi i} = \omega_i/k_i$ and group velocity $c\beta_{gi}$ are given by $\beta_{\varphi i}^{-1} = \beta_{gi} = \pm[1 - \omega_p^2/\omega_i^2 - 4c^2/(r_i\omega_i)^2]^{1/2}$. The positive sign is taken for the pump laser pulse and forward propagating injection laser pulse, and the negative sign is taken for the backward propagating injection laser pulse. The longitudinal profile of the pump pulse is assumed to have the form $\hat{a}_0 = -a_0\Pi((2\psi - \pi)/4\pi)\cos[(2\psi - \pi)/4]$, where $\Pi(s)$ is a step function such that $\Pi(s) = 1$ for $|s| < 1/2$ and zero otherwise. The injection laser pulses are assumed to have longitudinal profiles of the form $\hat{a}_i = a_i\Pi(s_i)\cos(\pi s_i)$, where $s_i = (z - \beta_{gi} ct - z_i)L_i^{-1}$ with L_i the length of the injection laser pulses and z_i a constant.

The polarizations of the laser pulses are chosen to be $\hat{e}_{\perp 0} = \hat{x}$ and $\hat{e}_{\perp 1} = \hat{e}_{\perp 2} = \hat{y}$ such that $\vec{a}_0 \cdot \vec{a}_2 \simeq 0$ and thus there is no beating (no slow plasma wave generation) from the interaction of the pump laser pulse and the counter-

propagating injection laser pulse. The ponderomotive potential due to the beating of the injection laser pulses (averaged over the fast phase oscillations) is $\vec{a}_1 \cdot \vec{a}_2 = \hat{a}_1^2 + \hat{a}_2^2 + 2\hat{a}_1\hat{a}_2\cos(\psi_1 - \psi_2)$. The plasma waves produced by the injection laser pulses can be neglected ($\phi_1 \sim \phi_2 \ll \phi_0$) since the injection laser pulse amplitudes required for trapping are much less than the pump laser pulse amplitude and the pulse lengths of the injection laser pulses can be chosen to provide poor coupling between the plasma response and the injection laser pulses.

Assuming $a_0^2 < 1$, the plasma wave potential ϕ excited by the ponderomotive force generated by the pump laser pulse (to lowest-order in pump laser pulse amplitude) near the waist of the pump laser pulse ($z \ll Z_{R0}$) satisfies

$$\phi = \frac{\hat{a}_0^2}{4} e^{(-2r^2/r_0^2)} \left[1 + \sin\psi + \left(\frac{3\pi}{4} - \frac{\psi}{2}\right)\cos\psi\right] \tag{4.31}$$

inside the pump laser pulse, and

$$\phi = \frac{\pi\hat{a}_0^2}{4} e^{(-2r^2/r_0^2)} \cos\psi \tag{4.32}$$

after the pump laser pulse. The axial and radial components of the electric field due to the plasma wave potential after the pump laser pulse are

$$E_z = \frac{m_e c^2}{e}\frac{\omega_p}{c}\phi_0 e^{(-2r^2/r_0^2)}\sin\psi \tag{4.33}$$

$$E_r = \frac{m_e c^2}{e}\frac{4r}{r_0^2}\phi_0 e^{(-2r^2/r_0^2)}\cos\psi\,, \tag{4.34}$$

where $\phi_o = \pi\hat{a}_0^2/4$. The radial electric field will provide a focusing force for an electron at a plasma wave phase of $\cos\psi > 0$ and a defocusing force for $\cos\psi < 0$, as noted in Sec. 4.2.1.

The equations of motion for the plasma electrons (relativistic Lorentz equation for each electron) in the combined three-dimensional fields of the three lasers and the plasma wave were numerically integrated using an adaptive step-size Runge-Kutta method [71]. The plasma was assumed to be initially homogeneous and cold such that the test particles were loaded uniformly with no initial momentum. Unless

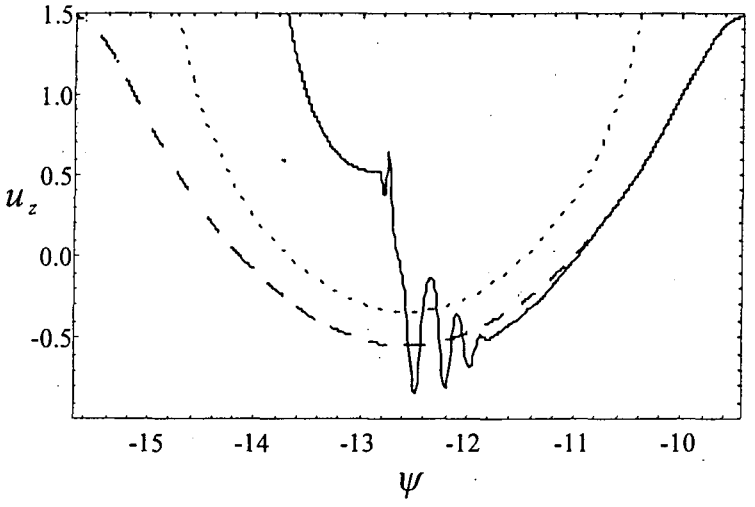

Figure 4.8: Phase space (ψ, u_z) orbit of test electron without the beating injection laser pulses (dashed line) and with the beating injection laser pulses (solid line). The separatrix between trapped and untrapped plasma wave orbits (dotted line) is shown.

otherwise stated, the parameters used in the numerical simulations are listed in Table 4.1.

4.3.1 Simulation Results

The orbit of a single test electron in longitudinal phase space (ψ, u_z) interacting with the combined fields of the lasers and the plasma wave is shown in Fig. 4.8. The dotted line shows the separatrix between trapped and untrapped orbits of the plasma wave Hamiltonian Eq. (4.1), the dashed line shows the orbit of the test electron without the beating injection laser pulses (an untrapped plasma wave orbit), and the solid line shows the orbit of the test electron interacting with the beating injection laser pulses. Figure 4.8 illustrates the phase-shift and momentum gain from the beating injection laser pulses allowing the test electron to move from an untrapped to a trapped plasma wave orbit.

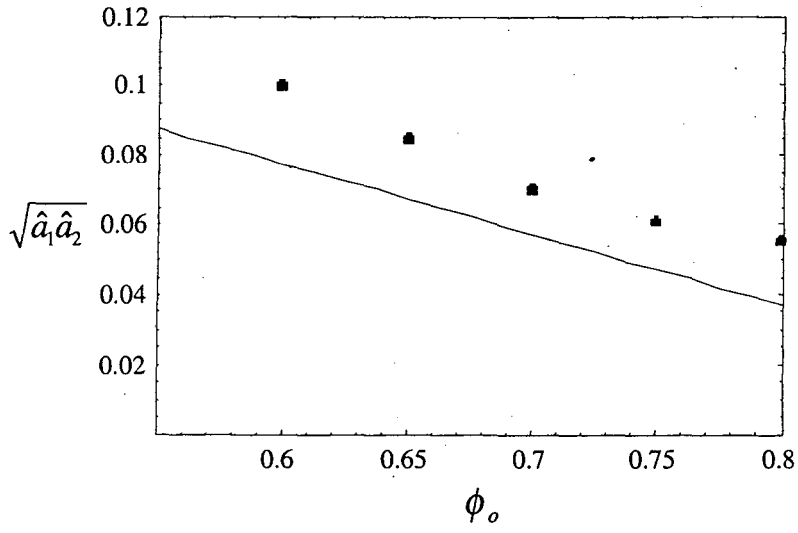

Figure 4.9: Threshold beat wave amplitude parameter for trapping $(\hat{a}_1\hat{a}_2)^{1/2}$ versus plasma wave potential amplitude. Solid line is Eq. (4.16) with $\phi_o = 0.7$ and $\beta_b = -0.2$. Points are numerical simulation results.

The particle transport code was used to test the analytic predictions made by the Hamiltonian analysis of the motion of electrons in the beat wave and the plasma wave presented in Sec. 4.2. The minimum injection laser pulse amplitude for injection of plasma electrons into a trapped orbit of the plasma wave is shown in Fig. 4.9. In Fig. 4.9, the solid line is the analytic estimation [Eq. (4.16), with $H = \gamma_\varphi^{-1} + \phi_o$ and $\beta_\varphi = -0.2$], and the points correspond to simulation results. A somewhat higher ($\sim 10\%$) laser pulse amplitude is needed for trapping in the simulation results than predicted by the analytic estimation. This is due to the nonconstant laser pulse profiles (longitudinal and transverse) used in the numerical simulations, i.e., the electrons experience a lower $(\hat{a}_1\hat{a}_2)^{1/2}$ before and after the collision of the maxima of the injection laser pulses and when the particles move off axis due to the transverse fields of the plasma wave.

To determine the optimal injection phase which minimizes the injection laser pulse amplitude required for trapping of background plasma electrons, the frac-

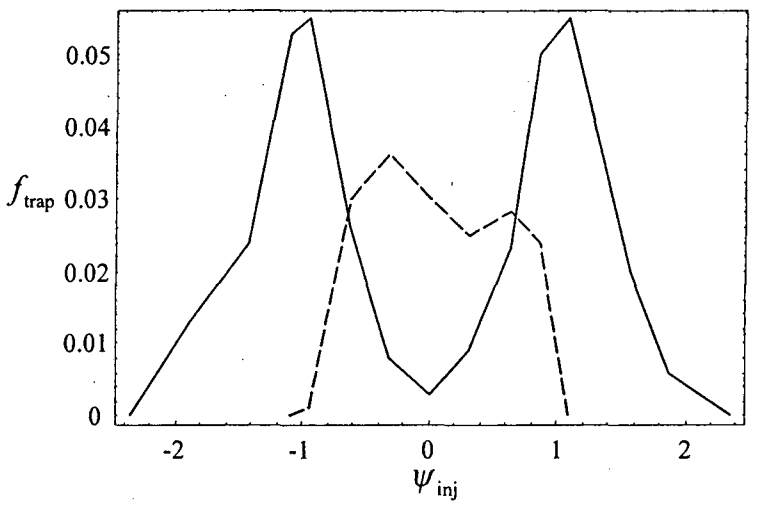

Figure 4.10: Fraction of loaded test electrons $f_{\rm trap}$ which become trapped and focused (dashed line) and the fraction of loaded test electrons which become trapped and defocused (solid line) after the colliding laser pulses versus plasma wave injection phase $\psi_{\rm inj}$.

tion of loaded test electrons which become trapped $f_{\rm trap}$ as a result of the colliding injection laser pulses was examined as a function of the injection phase $\psi_{\rm inj}$ (the plasma wave phase where the maxima of the injection laser pulses collide). Figure 4.10 shows the fraction of loaded electrons which become trapped and focused (dashed line) and the fraction which become trapped and defocused (solid line) versus the injection phase $\psi_{\rm inj}$. In Fig. 4.10, $f_{\rm trap}$ is defined as the fraction of electrons that become trapped which were loaded uniformly in a region of length $\pi/2$ in phase about $\psi_{\rm inj}$ and $r \leq 2$ μm (simulations show electrons loaded with $r > 2$ μm do not become trapped). The trapping fraction is peaked at $\psi_{\rm opt} \simeq \pm 1.0$ which agrees well with the analytic predictions [Eq. (4.17) with $\beta_b = -0.2$ and $\phi_o = 0.7$]. The asymmetry in the trapping fraction shown in Fig. 4.10 is due to the distortion of the beat wave buckets from the presence of the plasma wave as described in Sec. 4.2.2. Significant trapping of electrons occurs in an injection phase region of $-1.5 \lesssim \psi_{\rm inj} \lesssim 1.5$.

This indicates that the two colliding injection laser pulses must be synchronized to the plasma wave with an accuracy of $\sim$ 10 fs, which is not a serious timing constraint for current laser technology.

4.3.2 Electron Bunch Dynamics

To further characterize the performance of an injector based on this colliding laser pulse concept, the dynamics of the trapped electron bunches were studied analytically and numerically. Figure 4.11 shows an example of simulation results of the evolution of a typical trapped and focused electron bunch generated by colliding the injection laser pulses at a plasma wave phase of $\psi_{\rm inj} = 0$.

The mean phase $\langle\psi\rangle$ (dashed line) and mean energy $\langle\gamma\rangle$ (solid line) of a trapped electron bunch versus interaction length are shown in Fig. 4.11(a). The interaction length $L_{\rm int}$ considered in these simulations is much less than the dephasing length $L_{\rm int} \ll L_{\rm dephase} \sim \lambda_p\gamma_\varphi^2$ (i.e., interaction times much shorter than the bounce time in a trapped plasma wave orbit) and less than the Rayleigh length $L_{\rm int} < Z_{R0}$. The figure shows the reduction of phase slippage as the bunch becomes relativistic and the linear growth of the mean energy of the bunch in this regime.

The rms phase spread σ_ψ (dashed line) and the rms energy spread σ_γ (solid line) of the trapped electron bunch versus interaction length are plotted in Fig. 4.11(b). Figure 4.11(b) shows growth of the rms energy spread; while the rms phase spread (or bunch duration, which is defined as $\omega_p^{-1}\sigma_\psi$) is constant once the bunch becomes relativistic. This is due to the absence of phase slippage for the interaction lengths considered [i.e., $\delta\psi = (\beta_z - \beta_\varphi)\omega_p\delta t \approx 0$ for $c\delta t \ll \lambda_p\gamma_\varphi^2$].

These simulations can be understood by considering the longitudinal equations of motion for the electron bunch in the ultra-relativistic limit

$$\frac{d\gamma}{d\hat{t}} = \frac{c}{\omega_p}\vec{\beta}\cdot\frac{\partial\phi}{\partial\vec{x}} \simeq -\phi_0\sin\psi, \tag{4.35}$$

$$\frac{d\psi}{d\hat{t}} = \beta_z - \beta_\varphi \simeq 0\,, \tag{4.36}$$

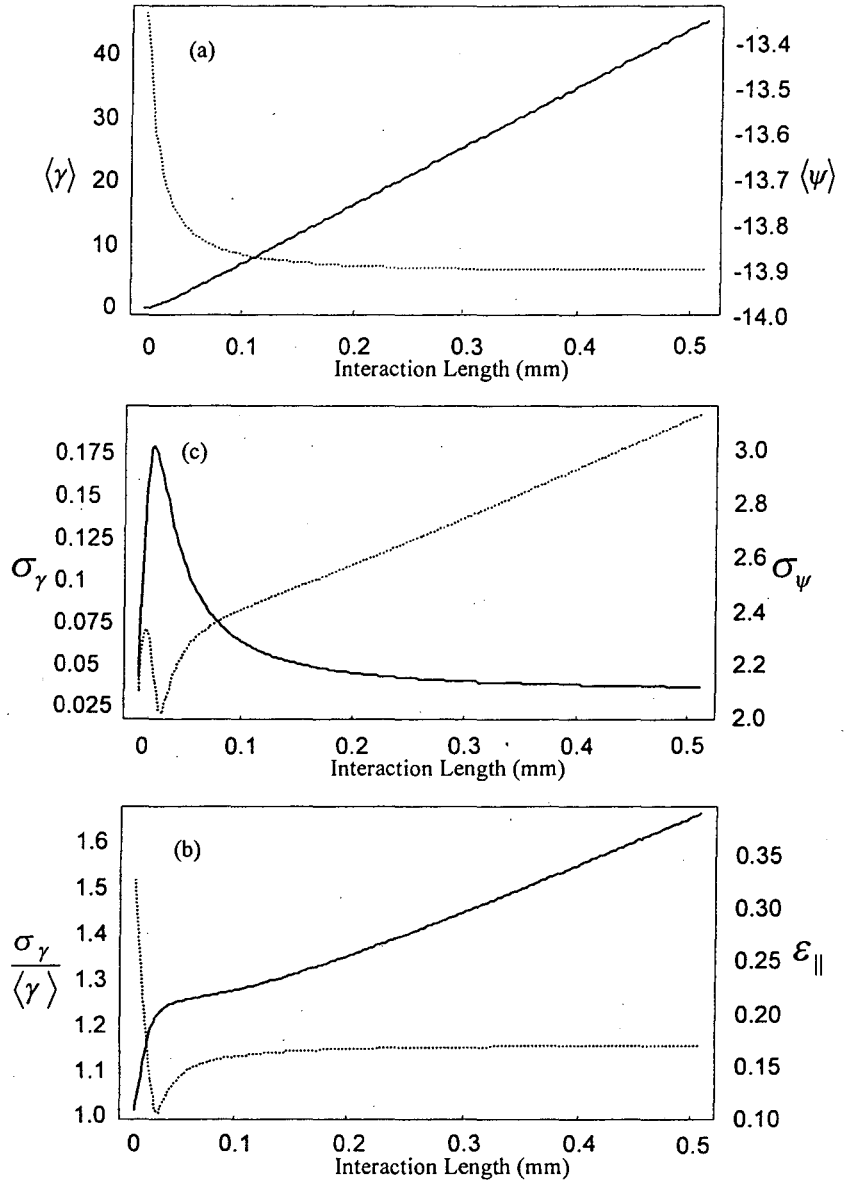

Figure 4.11: Longitudinal dynamics of trapped electron bunch: (a) mean phase $\langle\psi\rangle$ (dashed line) and mean energy $\langle\gamma\rangle$ (solid line), (b) rms phase spread σ_ψ (dashed line) and rms energy spread σ_γ (solid line), and (c) fractional energy spread $\sigma_\gamma/\langle\gamma\rangle$ (solid line) and longitudinal rms emittance $\varepsilon_\parallel$ (10^{-9} eV sec) (dashed line).

where $\hat{t} = \omega_p t$. Since the interaction lengths are much shorter than the dephasing length, the phase slippage can be taken to be zero $d\psi/dt \simeq 0$. With these assumptions, Eqs. (4.35) and (4.36) have solutions

$$\gamma = \gamma_0 - \phi_0 \hat{t} \sin\psi_0, \tag{4.37}$$

$$\psi = \psi_0 . \tag{4.38}$$

With zero (or constant) phase slippage, the rms phase spread $\sigma_\psi^2 = \langle\psi^2\rangle - \langle\psi\rangle^2$ is constant,

$$\frac{d\sigma_\psi}{d\hat{t}} = \frac{1}{\sigma_\psi}\left[\left\langle\psi\frac{d\psi}{d\hat{t}}\right\rangle - \langle\psi\rangle\left\langle\frac{d\psi}{d\hat{t}}\right\rangle\right] = 0 . \tag{4.39}$$

If a Gaussian distribution in plasma wave phase of the trapped electrons is assumed,

$$\frac{dN}{d\psi_0} = \frac{1}{\sqrt{2\pi\sigma_\psi^2}} \exp\left[\frac{-(\psi_0 - \langle\psi_0\rangle)^2}{2\sigma_\psi^2}\right] , \tag{4.40}$$

where the expectation value of an arbitrary function $f(\psi_0)$ is

$$\langle f(\psi_0)\rangle = \int \frac{dN}{d\psi_0} f(\psi_0) d\psi_0 , \tag{4.41}$$

then, from Eq. (4.37), the mean energy of the electron bunch is

$$\langle\gamma\rangle = \langle\gamma_0\rangle - \phi_0 \hat{t} e^{-\sigma_\psi^2/2} \sin\langle\psi_0\rangle . \tag{4.42}$$

Assuming the initial conditions γ_0 and ψ_0 are uncorrelated (statistically independent) such that $\langle\gamma_0\psi_0\rangle = \langle\gamma_0\rangle\langle\psi_0\rangle$, the rms energy spread $\sigma_\gamma^2 = \langle\gamma^2\rangle - \langle\gamma\rangle^2$ is

$$\sigma_\gamma^2 = \sigma_{\gamma_0}^2 + \frac{1}{2}\phi_0^2\hat{t}^2\left(1 - e^{-\sigma_\psi^2}\right)\left(1 + e^{-\sigma_\psi^2}\cos[2\langle\psi_0\rangle]\right) . \tag{4.43}$$

Equations (4.42) and (4.43) predict the linear growth in mean energy and the non-conservation of the rms energy spread of the electron bunch that is shown in Fig. 4.11.

Using Eqs. (4.42) and (4.43), the fractional energy spread of the trapped electron bunch is

$$\frac{\sigma_\gamma}{\langle\gamma\rangle} = \frac{\pm\sqrt{\sigma_{\gamma_0}^2 + \frac{1}{2}\phi_0^2\hat{t}^2\left(1 - e^{-\sigma_\psi^2}\right)\left(1 + e^{-\sigma_\psi^2}\cos[2\langle\psi_0\rangle]\right)}}{\langle\gamma_0\rangle - \phi_0\hat{t}e^{-\sigma_\psi^2/2}\sin\langle\psi_0\rangle} , \tag{4.44}$$

with the asymptotic value (for large $\hat{t}$)

$$\frac{\sigma_\gamma}{\langle\gamma\rangle} \rightarrow \frac{\sqrt{\frac{1}{2}\left(1-e^{-\sigma_\psi^2}\right)\left(1+e^{-\sigma_\psi^2}\cos[2\langle\psi_0\rangle]\right)}}{e^{-\sigma_\psi^2/2}\sin\langle\psi_0\rangle} . \tag{4.45}$$

Figure 4.11(c) shows that the fractional energy spread of the trapped electron bunch asymptotes to a constant value as indicated by Eq. (4.45). For $\sigma_\psi \ll 1$, Eq. (4.45) simplifies to

$$\frac{\sigma_\gamma}{\langle\gamma\rangle} \simeq \sigma_\psi \cot\langle\psi_0\rangle . \tag{4.46}$$

The asymptotic form of the fractional energy spread Eq. (4.45) has a minimum value at a phase of $\langle\psi_0\rangle = -\pi/2$ (at the crest of the plasma wave), $[\sigma_\gamma/\langle\gamma\rangle]_{\min} = \sqrt{2}\sinh(\sigma_\psi^2/2) \simeq \sigma_\psi^2/\sqrt{2}$. As Eq. (4.45) indicates, the asymptotic fractional energy spread is independent of the wave amplitude, and is just a function of the phase and the rms phase spread, which is constant assuming zero (or constant) phase slippage. As shown in the numerical simulation Fig. 4.11, once the bunch becomes highly relativistic, $\langle\psi\rangle \simeq -13.9$ and $\sigma_\psi \simeq 0.17$. With these values, the asymptotic fractional energy spread predicted by Eq. (4.46) is $\sigma_\gamma/\langle\gamma\rangle \simeq 0.04$, in good agreement with Fig. 4.11(c).

The longitudinal rms emittance of the trapped electron bunch is $\varepsilon_\parallel$ (eV sec) $= m_e c^2 \omega_p^{-1}(\sigma_\gamma^2\sigma_\psi^2 - \sigma_{\gamma\psi}^2)^{1/2}$, where $\sigma_{\gamma\psi} = \langle\gamma\psi\rangle - \langle\gamma\rangle\langle\psi\rangle$. With the assumptions $\sigma_\psi \ll 1$ and a Gaussian distribution in phase Eq. (4.40), the normalized longitudinal rms emittance is

$$\varepsilon_\parallel = \frac{m_e c^2}{\omega_p}\left[\sigma_{\gamma_0}^2\sigma_\psi^2 + \frac{1}{2}\phi_0^2\hat{t}^2\sigma_\psi^6\sin\langle\psi_0\rangle\right]^{1/2} . \tag{4.47}$$

Equation (4.47) indicates the longitudinal rms emittance of the trapped electron bunch $\varepsilon_\parallel$ grows linearly for large $\hat{t}$. This non-conservation of longitudinal rms emittance is shown in the numerical simulation Fig. 4.11(c). The emittance growth is due to the fact that the bunch becomes relativistic at a plasma wave phase where the axial electric field, and therefore the energy gain, is a nonlinear function of plasma wave phase.

Near the axis $r/r_0 < 1$, the radial electric field of the plasma wave Eq. (4.34) is, to lowest-order, linear with respect to the radial coordinate. If the electron bunch is injected into the focusing region ($\cos\psi > 0$), the radial electric field will provide a focusing force with a focusing strength $k_r^2 = eE_r/(\gamma m_e c^2 r) \simeq [4\phi_o/(\gamma r_0^2)]\cos\psi$. In this regime, the evolution of the rms radius of the electron bunch will be described by the envelope equation [72]

$$\frac{d^2\sigma_r}{dt^2} + \frac{1}{\gamma}\frac{d\gamma}{dt}\frac{d\sigma_r}{dt} + c^2 k_r^2 \sigma_r = \frac{2c^2(I/I_A)}{\gamma^2\sigma_r} + \frac{\varepsilon_\perp^2 c^2}{\gamma^2\sigma_r^3}\,, \tag{4.48}$$

where $\sigma_r = [\langle r^2\rangle - \langle r\rangle^2]^{1/2}$ is the rms radius of the electron bunch, I is the beam current, $I_A = (m_e c^3/e)\beta\gamma$ is the Alfvén current, and $\varepsilon_\perp = \gamma(\sigma_r^2\sigma_{r'}^2 - \sigma_{rr'}^2)^{1/2}$ is the normalized transverse rms emittance where $\sigma_{r'}^2 = \langle (c^{-1}d_t r)^2\rangle - \langle c^{-1}d_t r\rangle^2$ and $\sigma_{rr'} = \langle r c^{-1}d_t r\rangle - \langle r\rangle\langle c^{-1}d_t r\rangle$. With linear focusing, the normalized transverse rms emittance is conserved for a monoenergetic beam. Figure 4.12 shows the transverse phase space $(\omega_p x/c, \gamma\beta_x)$ of the trapped and focused electron bunch presented in Fig. 4.2(c) just after the collision of the injection laser pulses (after 0.07 mm of propagation) and Fig. 4.2(d) after 0.7 mm of propagation. The slight increase in normalized transverse rms emittance shown in these figures is due to the nonlinear focusing force provided by the plasma wave. In principle, a collimator may be used to spatially filter the trapped bunch and reduce the transverse emittance.

The effects of space-charge within the trapped electron bunch were not included in these simulations. This omission can be justified by considering the ratio of space-charge to emittance terms in the beam envelope equation Eq. (4.48),

$$2\frac{I}{I_A}\frac{\varepsilon_\perp^2}{\sigma_r^2}\,. \tag{4.49}$$

For the electron bunches described in Sec. 4.3.3, $I \sim 0.4$ kA and the ratio of the space-charge term to the emittance term Eq. (4.49) is $\sim 10^{-3}$. Therefore the bunch is emittance dominated while the bunch remains in the plasma.

Space-charge forces should not be a concern longitudinally if the electric field due to space-charge forces within the bunch is much less than the axial electric

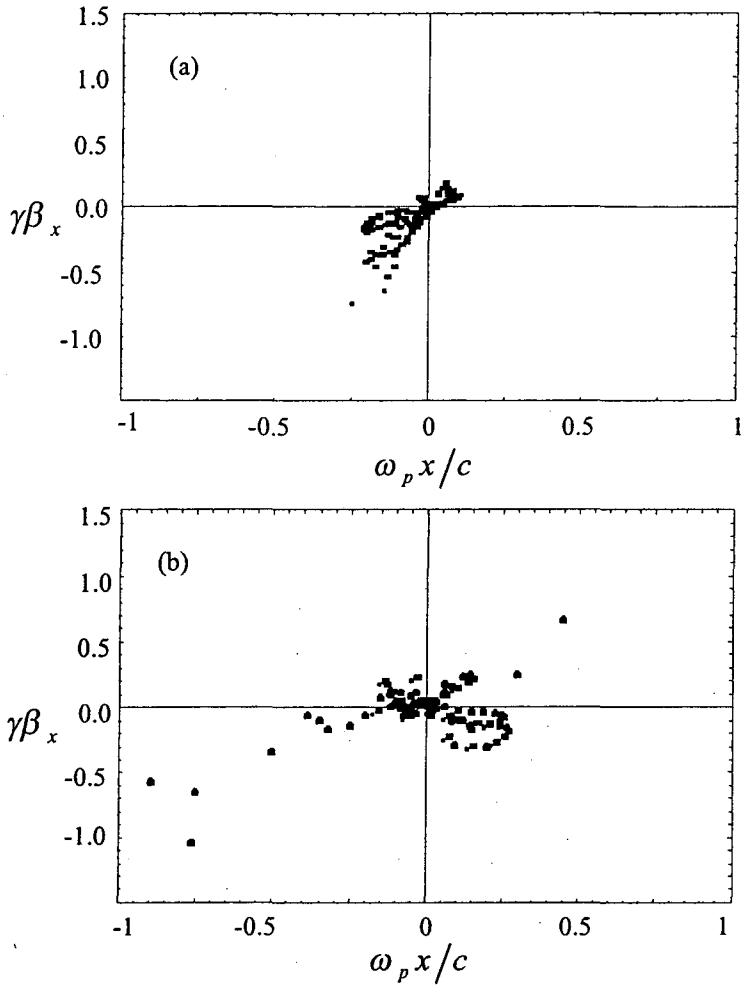

Figure 4.12: Transverse phase space distribution $(\omega_p x/c, \gamma\beta_x)$ of a trapped and focused electron bunch (a) just after the collision of the injection laser pulses (after 0.07 mm of propagation) and (b) after 0.7 mm of propagation.

field due to the plasma wave [73]. This will be satisfied when the ratio of beam density n_b to the plasma density n_e is $n_b/n_e \ll a_0^2/\sigma_\psi$. For the parameters under consideration in this Chapter, this condition is satisfied, and the longitudinal space-charge effects are small while the bunch remains in the plasma. Space-charge effects can become quite significant after the bunch leaves the plasma.

4.3.3 Electron Bunch Quality

The quality of the electron bunch can be examined as the beat wave amplitude parameter $(\hat{a}_1\hat{a}_2)^{1/2}$ is increased beyond the threshold value for injection into a trapped and focused orbit [Eq. (4.16), with $H \leq \gamma_\varphi^{-1}$]. Figure 4.13(a) shows the fraction of loaded test electrons which become trapped and focused (solid line) as a result of colliding the injection laser pulses at a plasma wave phase of $\psi_{\rm inj} = 0$ versus the beat wave amplitude parameter. The fraction of loaded test electrons is defined as in Sec. 4.3.1. The maximum value shown on Fig. 4.13(a) corresponds to a bunch number of $N_b \simeq 0.5 \times 10^7$ electrons for a plasma density of $n_e = 7 \times 10^{17}$ cm^{-3}.

As shown in Sec. 4.3.2, the rms phase spread (bunch duration) is constant for a highly relativistic bunch, the fractional energy spread is asymptotic, and the transverse normalized rms emittance is conserved for large pump laser spot size. Therefore, these measures of bunch quality were examined versus increasing beat wave amplitude parameter. Figure 4.13(a) shows the bunch duration of the trapped electron bunch (dashed line) versus the beat wave amplitude parameter. The asymptotic fractional energy spread $\sigma_\gamma/\langle\gamma\rangle$ (solid line) and the normalized transverse rms emittance $\varepsilon_\perp$ (dashed line) after 0.5 mm of propagation versus the beat wave amplitude parameter are shown in Fig. 4.13(b). These figures indicate the production of $\sim$ 1 fs election bunches with $\sim$ 1% fractional energy spread and $\sim$1 mm mrad normalized transverse rms emittance.

A dramatic example of the colliding pulse injection process is shown in Fig. 4.2 for $L_1 = L_2 = 10$ μm and $\hat{a}_1 = \hat{a}_2 = 0.32$ with $\psi_{\rm inj} = 0$ (other parameters as in

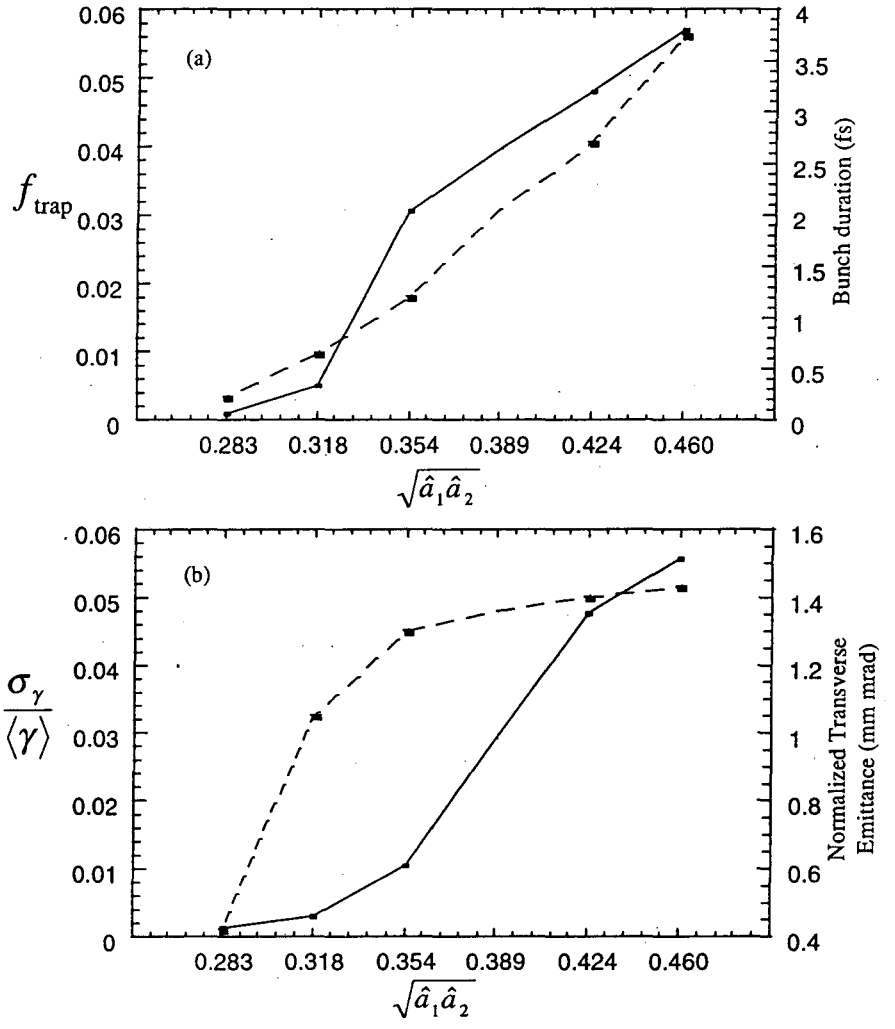

Figure 4.13: (a) Fraction of loaded test electrons which become trapped and focused after the colliding laser pulses (solid line) and bunch duration (fs) of trapped electron bunch (dashed line) versus beat wave amplitude parameter. (b) Asymptotic fractional energy spread $\sigma_\gamma / \langle\gamma\rangle$ (solid line) and normalized transverse rms emittance $\varepsilon_\perp$ (mm mrad) (dashed line) after 0.5 mm of propagation of trapped electron bunch versus beat wave amplitude parameter.

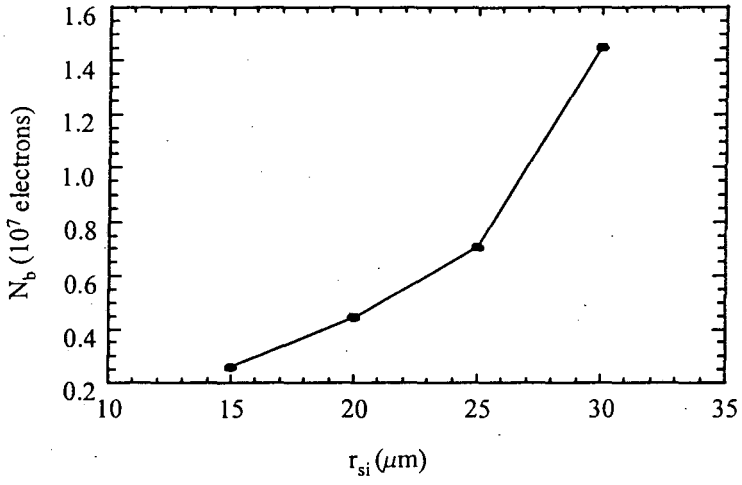

Figure 4.14: Number of trapped and focused electrons N_b versus spot size of laser pulses ($r_0 = r_1 = r_2$).

Table 4.1). Figure 4.2 shows longitudinal phase space (ψ, u_z) of the test electrons. As shown in Fig. 4.2(d), the results are dramatic: a 1 fs electron bunch with energy 39 MeV, fractional energy spread of 0.2%, and normalized transverse emittance $\simeq 0.9$ mm mrad. The bunch number is $N_b \simeq 2.6 \times 10^6$ electrons for a plasma density of $n_e = 7 \times 10^{17}$ cm^{-3}.

The number of trapped electrons can be increased by increasing the injection laser spot size (i.e., increasing the injection laser pulse power). Figure 4.14 shows that the number of trapped and focused electrons increases for increasing spot size of the laser pulses (other parameters the same as Fig. 4.2). For $r_0 = r_1 = r_2 = 30$ μm ($P_1 = P_2 \simeq 6$ TW), the number of trapped electrons increases to $N_b \simeq 14.5 \times 10^6$ electrons.

4.4 Summary

In this Chapter, we have explored the generation of ultrashort electron bunches by using colliding laser pulses to dephase background plasma electrons undergoing fluid oscillations in a plasma wave. A variation of this scheme, which relies on the same trapping mechanism, is to remove the forward propagating injection laser pulse and to beat the pump laser pulse with the backward propagating injection laser pulse. Near the back of the pump pulse, a sufficiently large plasma wave will be generated to allow trapping of plasma electrons dephased by the slow wave created by the beating of the pump laser pulse and the backward propagating injection laser pulse. Alternatively, colliding pulse injection could be done using several forward propagating injection pulses (which are properly phased) and a single counter-propagating injection pulse so that several adjacent plasma wave buckets could be filled with ultrashort electron bunches. Other variations on the colliding pulse injection concept can be readily envisioned.

In summary, the colliding laser pulse injection scheme investigated in this Chapter has the ability to produce relativistic femtosecond electron bunches with low fractional energy spread ($\sim 1\%$) and low normalized transverse emittance (~ 1 mm mrad). The colliding laser pulse scheme requires relatively low laser power compared to the pump laser pulse $a_1^2 \sim a_2^2 \ll a_0^2$, and allows for detailed control of the injection process through the injection phase (position of the forward injection laser pulse), the injection time (injection laser pulse lengths), the beat wave velocity (frequencies of the injection laser pulses), and the beat wave amplitude parameter (injection laser pulse intensities). These capabilities are critical for the experimental realization of laser-triggered injection and subsequently compact laser-plasma-based particle accelerators.

Chapter 5

Non-Paraxial Propagation of Ultrashort Laser Pulses in Plasmas

In this chapter, the non-paraxial propagation of ultrashort high-power laser pulses in underdense plasmas is examined. Envelope equations are derived for optical beam parameters which include finite-radius and finite laser pulse length effects. Solutions of the envelope equations are presented for an adiabatic plasma response. For an adiabatic plasma response, pulse energy conservation is shown and the nonlinear group velocity is calculated. In the low-power adiabatic limit, the effects of betatron oscillation damping, laser pulse self-steepening, and self-phase modulation are analyzed. Laser-plasma instabilities are examined for the general non-adiabatic plasma response. The coupling of forward Raman scattering and self-modulation instabilities are studied and the asymptotic growth rates of the instabilities are derived.

5.1 Introduction

As discussed in Chapter 1, advances in laser technology have produced compact ultrashort laser pulses with extremely high intensities. These high-intensity laser pulses are capable of generating plasma waves and have applications to laser-driven plasma-based accelerators (e.g., the laser wakefield accelerator). In addition to plasma-based accelerators, intense laser pulses have applications in areas such as harmonic generation [74, 75], short wavelength radiation sources [76, 77], and laser-fusion schemes [78]. These ultrashort high-intensity pulses can have durations of only a few optical cycles. In this regime, finite laser pulse length effects will influence the laser pulse propagation dynamics.

A laser pulse propagating in a plasma can be described by the Maxwell equations and the cold, collisionless fluid equations modeling the plasma [45]. Combining the Maxwell equations and the fluid equations, the wave equation for the transverse component of the normalized vector potential of the laser field $a_\perp$ in the Coulomb gauge $\nabla \cdot \vec{a} = 0$ is

$$\left(\nabla^2 - \frac{1}{c^2}\frac{\partial^2}{\partial t^2}\right) a_\perp = k_p^2 \left(\hat{n} + \delta\hat{n}\right) a_\perp \,, \tag{5.1}$$

where $k_p^2 = \omega_p^2/c^2 = 4\pi e^2 n_0/(m_e c^2)$, $\delta\hat{n}$ is the nonlinear plasma density perturbation due to plasma wave generation and relativistic effects, and $\hat{n} = n(r)/n_0$ is the contribution owing to any plasma inhomogeneities. For example, if the laser pulse is propagating in a preformed transversely-parabolic plasma density channel, then $\hat{n}$ can be expressed as

$$\hat{n}(r) = 1 + \frac{\Delta n}{n_0}\left(\frac{r}{r_c}\right)^2 \,, \tag{5.2}$$

where Δn is the plasma channel depth and r_c is a length characteristic of the plasma channel radius.

The nonlinear plasma density perturbation to second-order in the normal-

ized vector potential of the laser field is

$$\delta\hat{n} = \frac{n_2}{n_0} - \frac{a_\perp^2}{2} , \tag{5.3}$$

where n_2/n_0 is the plasma density perturbation owing to plasma wave generation and $-a_\perp^2/2$ is the effect of the relativistic energy increase of the plasma electrons in the presence of the laser field (cf. Sec. 1.1.1). In the limits $a_\perp^2 \ll 1$ and $k_p r_c \gg 1$, the nonlinear plasma density perturbation due to plasma wave generation n_2/n_0 is described by the equation

$$\left(\frac{\partial^2}{\partial t^2} + c^2 k_p^2\right) \frac{n_2}{n_0} = c^2 \nabla^2 \frac{a_\perp^2}{2} . \tag{5.4}$$

The right-hand side of Eq. (5.4) represents the normalized transverse current in the plasma driven by the ponderomotive force of the laser pulse. In the limits $k_p^2 r_0^2 \ll 1$, where r_0 is the minimum laser spot size (i.e., $r_0 \sim r_c$), and the laser group velocity is near the speed of light $\beta_{g0} \simeq 1$, Eq. (5.4) can be rewritten as

$$\left(\frac{\partial^2}{\partial \xi^2} + k_p^2\right) \delta\hat{n} = -k_p^2 \frac{a_\perp^2}{2} , \tag{5.5}$$

where $\xi = z - \beta_{g0} ct$. The solution to Eq. (5.5) is

$$\delta\hat{n} = -k_p \int_0^\xi d\xi_1 \sin\left[k_p (\xi - \xi_1)\right] \frac{1}{2} a_\perp^2(\xi_1) . \tag{5.6}$$

For long pulse length lasers, Eq. (5.6) reduces to $\delta\hat{n} \simeq -a_\perp^2/2$.

The propagation dynamics of long pulse length laser pulses (long compared to the laser wavelength) is adequately described by the well-known paraxial wave equation whose solutions are Laguerre-Gaussian functions [35]. If $a_\perp = \hat{a} \exp(ik\xi)$, with the assumptions $\beta_{g0} = 1$, $|\partial_z \hat{a}| \ll |k\hat{a}|$, and $|\partial_t \hat{a}| \ll |ck\hat{a}|$, then the left-hand side of Eq. (5.1) reduces to the paraxial wave equation operator

$$\left(\nabla_\perp^2 + 2ik\frac{\partial}{\partial z}\right) \hat{a} = k_p^2 \left(\hat{n} + \delta\hat{n}\right) \hat{a} . \tag{5.7}$$

In the paraxial approximation, the lowest-order diffraction effects are contained, but finite pulse length effects and higher-order diffraction effects are neglected. In

addition, the paraxial approximation assumes a fixed group velocity and is not capable of describing phenomena which require axial transport of laser energy and axial modulation of the laser power (e.g., forward Raman scattering). Conventional theories [79, 80] of intense finite-radius laser pulse propagation in plasmas assume the paraxial approximation. In this chapter, a nonlinear theory of non-paraxial laser pulse propagation is presented which is valid for ultrashort high-power [for $P \leq P_{\rm crit} \simeq 17(\omega/\omega_p)^2$] laser pulses in underdense plasmas.

5.2 Non-Paraxial Wave Equation

The wave equation Eq. (5.1) can be rewritten in terms of the independent variables: phase (or laser beam slice) $\xi = z - \beta_{g0} ct$ and propagation distance z. With the coordinate transformation $(z,t) \rightarrow (z,\xi)$, the wave equation Eq. (5.1) becomes

$$\left[\nabla_\perp^2 + 2\frac{\partial^2}{\partial\xi\partial z} + \left(1-\beta_{g0}^2\right)\frac{\partial^2}{\partial\xi^2} + \frac{\partial^2}{\partial z^2}\right] a_\perp = k_p^2\left(\hat{n}+\delta\hat{n}\right) a_\perp \,. \tag{5.8}$$

Let β_{g0} be the linear group velocity of a matched fundamental mode Gaussian pulse [81] such that $\gamma_{g0}^{-2} = 1-\beta_{g0}^2 = \omega_p^2/\omega^2 + 4c^2/(r_0^2\omega^2)$. Introducing a slowly-varying envelope $\hat{a}$ such that $\mathrm{a}_\perp = \hat{a}\exp(ikz - i\omega t)$, where ω is the central frequency and k is the central wavenumber, the wave equation Eq. (5.8) becomes

$$\left[\nabla_\perp^2 + 2\left(ik + \frac{\partial}{\partial\xi}\right)\frac{\partial}{\partial z} + \gamma_{g0}^{-2}\frac{\partial^2}{\partial\xi^2} + \frac{\partial^2}{\partial z^2}\right]\hat{a} = K^2\hat{a}\,, \tag{5.9}$$

where $K^2 = k_p^2(\hat{n}+\delta\hat{n}) - \gamma_{g0}^{-2}\omega^2/c^2$.

For short laser pulse length propagation, the operators on the left-hand side of Eq. (5.9) scale as: $\nabla_\perp \sim r_0^{-1}$, $\partial_z \sim Z_R^{-1}$, and $\partial_\xi \sim L^{-1}$, where L is the laser pulse length and $Z_R = kr_0^2/2$ is the Rayleigh length. The last term on the left-hand side of Eq. (5.9) $\partial_z^2\hat{a}$ is small provided $L \ll 2Z_R$. This is valid in the parameter regime of interest, and therefore the term $\partial_z^2\hat{a}$ will be neglected in the following analysis. For an underdense plasma, $\gamma_{g0}^{-2} \ll 1$ and the dispersive term $\gamma_{g0}^{-2}\partial_\xi^2\hat{a}$ can also be

neglected. This approximation will be valid when $2L/Z_R \gg [1 + 4/(kr_0)^2](k_p/k)^2$ is satisfied. Neglecting the dispersive term will also limit the validity of the results to a propagation length less than the characteristic dispersion length for pulse broadening, or $z \ll Z_{\text{disp}}$, where $Z_{\text{disp}} = \gamma_{g0}^2 kL^2/2$ is the characteristic dispersion length [81].

With these assumptions (i.e., for the parameter regime $k^2 r_0^2/4 \gg kL \gg k_p^2 r_0^2/4 > 1$), the wave equation Eq. (5.9) reduces to

$$\left[\left(\nabla_\perp^2 + 2ik\frac{\partial}{\partial z}\right) + 2\frac{\partial^2}{\partial\xi\partial z}\right]\hat{a} \simeq K^2\hat{a}\,. \tag{5.10}$$

This equation contains the first-order diffraction represented by the paraxial operator $(\nabla_\perp^2 + 2ik\partial_z)$. Finite laser pulse length effects are represented by the operator $(2\partial_{\xi z}^2)$, which is the leading-order correction to the paraxial wave equation. In this analysis, the operator ∂_z in the leading-order correction to the paraxial operator will be approximated by the paraxial expression for the operator $\partial_z \simeq (K^2 - \nabla_\perp^2)/(2ik)$. With this approximation, Eq. (5.10) becomes

$$\left(\nabla_\perp^2 + 2ik\frac{\partial}{\partial z}\right)\hat{a} \simeq \left[K^2 + \frac{i}{k}\left(K^2 - \nabla_\perp^2\right)\frac{\partial}{\partial\xi}\right]\hat{a} = S\,, \tag{5.11}$$

where S can be interpreted as the source terms of the paraxial wave equation. Equation (5.11) can be analyzed using the Source Dependent Expansion method.

5.2.1 Source Dependent Expansion

The Source Dependent Expansion (SDE) method [82] is a general method for solving the paraxial wave equation with nonlinear source terms [e.g., Eq. (5.11)]. In the SDE method, the laser field is expanded in a complete set of source-dependent orthogonal Laguerre-Gaussian functions

$$\hat{a} = \sum_m \hat{a}_m L_m(\chi)\exp\left[-(1 - i\alpha)\frac{\chi}{2}\right]\,, \tag{5.12}$$

where $L_m(\chi)$ are Laguerre polynomials of order m, $\chi = 2r^2/r_s^2$, and $\hat{a}_m$ are the complex mode amplitudes. Let $\hat{a}_0 = a_r \exp(i\theta)$, where a_r and θ are real. These

Laguerre-Gaussian functions are implicit functions of the propagation distance z and the slice of the pulse ξ through the laser field parameters: spot size r_s, wavefront curvature α, amplitude a_r, and phase θ. Note that the radius of curvature of the laser phase fronts R_c is given by the relation $R_c = kr_s^2/(2\alpha)$.

Substituting Eq. (5.12) into Eq. (5.11), performing the differential operations, multiplying both sides by $L_m \exp[-(1+i\alpha)\chi/2]$, and integrating over χ from 0 to ∞ results in the equation [82]

$$\left(\frac{\partial}{\partial z} + A_m\right)\hat{a}_m - imB\hat{a}_{m-1} - i(m+1)B^*\hat{a}_{m+1} = -iF_m \,, \tag{5.13}$$

where

$$A_m = \frac{\dot{r}_s}{r_s} + i(2m+1)\left[\frac{(1+\alpha^2)}{kr_s^2} - \alpha\frac{\dot{r}_s}{r_s} + \frac{\dot{\alpha}}{2}\right] \,, \tag{5.14}$$

$$B = -\alpha\frac{\dot{r}_s}{r_s} - \frac{(1-\alpha^2)}{kr_s^2} + \frac{\dot{\alpha}}{2} - i\left(\frac{\dot{r}_s}{r_s} - \frac{2\alpha}{kr_s^2}\right) \,, \tag{5.15}$$

and

$$F_m = \frac{1}{2k}\int_0^\infty d\chi L_m(\chi)\exp\left[-(1+i\alpha)\frac{\chi}{2}\right] S \,. \tag{5.16}$$

Here $\dot{f} = \partial f/\partial z$ denotes partial differentiation with respect to z for any function $f(z,\xi)$.

Although the SDE method is capable of describing an arbitrary laser field composed of an arbitrary number of source-dependent modes, the results in the following sections assume that the laser field is adequately described by a single source-dependent Laguerre-Gaussian mode. This approximation will not be valid when the laser power greatly exceeds the critical power P_{crit} for relativistic self-focusing since the laser beam is expected to filament into many higher order modes in this overcritical regime [83, 84].

To derive expressions describing the evolution of the laser field parameters of the $m = 0$ SDE mode, it is assumed that the coupling to, as well as the amplitude of, the higher-order $m > 0$ SDE modes are small. Note that a single source-dependent

mode is a superposition of many vacuum Laguerre-Gaussian modes. Assuming $|\hat{a}_0| \gg |\hat{a}_m|$ for $m \geq 1$, Eq. (5.13) with $m = 1$ yields

$$B = \frac{F_1}{\hat{a}_0} \tag{5.17}$$

and Eq. (5.13) with $m = 0$ yields

$$\left(\frac{\partial}{\partial z} + A_0\right) \hat{a}_0 = -iF_0 \,. \tag{5.18}$$

Equations (5.17) and (5.18) completely determine the evolution of the fundamental Gaussian SDE mode.

5.2.2 Envelope Equations

Using the SDE method, envelope equations for the laser field parameters can be derived which describe the laser pulse evolution. Substituting Eqs. (5.14) and (5.15) into Eqs. (5.17) and (5.18) yields the envelope equations

$$\frac{\dot{r_s}}{r_s} = \frac{2\alpha}{kr_s^2} - \Im[H] \tag{5.19}$$

$$\frac{\dot{a_r}}{a_r} = -\frac{2\alpha}{kr_s^2} + \Im[G] + \Im[H] \tag{5.20}$$

$$\dot{\alpha} = \frac{2\left(1+\alpha^2\right)}{kr_s^2} + 2\Re[H] - 2\alpha\Im[H] \tag{5.21}$$

$$\dot{\theta} = -\frac{2}{kr_s^2} - \Re[G] - \Re[H] \,, \tag{5.22}$$

where $\Re[f]$ and $\Im[f]$ denote the real and imaginary parts respectively of any function f. Here G and H are the $m = 0$ and $m = 1$ solutions of Eq. (5.16) respectively

$$G = \frac{F_0}{\hat{a}_0} = \frac{1}{2k\hat{a}_0}\int_0^\infty d\chi e^{-\chi} S \tag{5.23}$$

$$H = \frac{F_1}{\hat{a}_0} = \frac{1}{2k\hat{a}_0}\int_0^\infty d\chi \left(1-\chi\right) e^{-\chi} S \,. \tag{5.24}$$

The envelope equations Eqs. (5.19) and (5.20) can be combined to provide an evolution equation for the laser pulse power

$$\frac{\partial}{\partial z}\hat{P} = 2\hat{P}\Im[G] \,, \tag{5.25}$$

where $\hat{P} = P/P_{\rm crit} = k_p^2 a_r^2 r_s^2/16$ is the laser pulse power normalized to the critical power for relativistic self-focusing.

In computing G and H it is assumed that the plasma inhomogeneity $\hat{n}$ is given by Eq. (5.2) (i.e., a transversely-parabolic plasma density channel) and that the nonlinear plasma response $\delta\hat{n}$ is given by Eq. (5.5) (i.e., the nonlinear plasma density perturbation to second-order in the normalized vector potential of the laser field). Performing the integrals Eqs. (5.23) and (5.24) yields the functions

$$G^{(1)} = \frac{1}{k^2 r_c^2}\left[\left(2-\Delta_c\frac{r_s^2}{r_c^2}\right)\left(\theta'-k-i\frac{a_r'}{a_r}\right)+\left(1-\Delta_c\frac{r_s^2}{r_c^2}\right)\left(\alpha'-2i\frac{r_s'}{r_s}-2\alpha\frac{r_s'}{r_s}\right)\right] \quad (5.26)$$

$$H^{(1)} = \frac{1}{k^2 r_c^2}\left[\Delta_c\frac{r_s^2}{r_c^2}\left(\theta'-k-i\frac{a_r'}{a_r}\right)-\left(1-2\Delta_c\frac{r_s^2}{r_c^2}\right)\left(\alpha'-2i\frac{r_s'}{r_s}-2\alpha\frac{r_s'}{r_s}\right)\right] \quad (5.27)$$

$$G^{(2)} = \frac{1}{k^2 r_s^2}\left[(i-\alpha)\,\alpha\alpha'+\left(1+\alpha^2\right)\left(2\alpha\frac{r_s'}{r_s}-\theta'+i\frac{a_r'}{a_r}\right)\right] \quad (5.28)$$

$$H^{(2)} = \frac{1}{k^2 r_s^2}\left[\left(1+2\alpha^2+i\alpha\right)\alpha'-2\left(2\alpha^3+i+3i\alpha^2\right)\frac{r_s'}{r_s}-(1-i\alpha)^2\left(\theta'-i\frac{a_r'}{a_r}\right)\right] \quad (5.29)$$

$$G^{(3)} = -\frac{k_p^3}{4k^2}\int_0^\xi d\xi_1 \sin\left[k_p(\xi-\xi_1)\right]\frac{a_{r1}^2 r_{s1}^2}{\left(r_s^2+r_{s1}^2\right)}\left\{k-\theta'+i\frac{a_r'}{a_r}+\frac{2i}{a_{r1}}\frac{\partial a_{r1}}{\partial\xi_1}+\right.$$
$$\left.\frac{r_{s1}^2}{r_s^2+r_{s1}^2}\left[(i+\alpha)\frac{r_s'}{r_s}-\frac{\alpha'}{2}+2i\frac{r_s^2}{r_{s1}^3}\frac{\partial r_{s1}}{\partial\xi_1}\right]\right\} \quad (5.30)$$

$$H^{(3)} = -\frac{k_p^3}{4k^2}\int_0^\xi d\xi_1 \sin\left[k_p(\xi-\xi_1)\right]\frac{a_{r1}^2 r_{s1}^2 r_s^2}{\left(r_s^2+r_{s1}^2\right)^2}\left\{k-\theta'+\frac{ia_r'}{a_r}+\frac{2i}{a_{r1}}\frac{\partial a_{r1}}{\partial\xi_1}+\right.$$
$$\left.\frac{r_{s1}^2\left(r_s^2-r_{s1}^2\right)}{2r_s^2\left(r_s^2+r_{s1}^2\right)}\left[2(i+\alpha)\frac{r_s'}{r_s}-\alpha'+4i\frac{r_s^2}{r_{s1}^3}\frac{\partial r_{s1}}{\partial\xi_1}\right]\right\}, \quad (5.31)$$

with $G = G^{(1)} + G^{(2)} + G^{(3)}$ and $H = H^{(1)} + H^{(2)} + H^{(3)}$. Here the primes indicate partial differentiation with respect to phase ξ and $\Delta_c = \Delta n/\Delta n_c$ is the plasma channel depth normalized to the critical plasma density channel depth $\Delta n_c = (\pi r_e r_c^2)^{-1}$,

where $r_e = e^2/(m_e c^2)$ is the classical electron radius. Physically, the critical plasma density channel depth is the plasma channel depth required for optical guiding of a matched laser pulse, as discussed in Sec. 5.2.3. The notation $r_{s1} = r_s(z, \xi_1)$ and $a_{s1} = a_s(z, \xi_1)$ was used in Eqs. (5.30) and (5.31).

The envelope equations Eqs. (5.19)-(5.22) with source terms Eqs. (5.26)-(5.31) can be solved for the evolution of the laser field parameters of a laser pulse in a homogeneous plasma ($\Delta_c = 0$) or a parabolic plasma density channel ($\Delta_c \neq 0$).

5.2.3 Paraxial Limit

In the long laser pulse length limit, the partial derivatives with respect to ξ can be neglected (since $\partial_\xi \sim L^{-1}$) in Eqs. (5.26)-(5.31). In this limit, the envelope equations Eqs. (5.19) and (5.21) can be combined to yield

$$\ddot{r}_s = \frac{4}{k^2 r_s^3}\left[1 - \Delta_c\left(\frac{r_s}{r_c}\right)^4 - \hat{P}\right] + r_s \frac{k_p^2}{k^2}\int_0^\xi d\xi_1 \cos[k_p(\xi - \xi_1)]\frac{\partial}{\partial \xi_1}\frac{a_{r1}^2 r_{s1}^2}{\left(r_s^2 + r_{s1}^2\right)^2} \,. \quad (5.32)$$

This equation can be derived directly from the paraxial wave equation and describes the propagation of a long laser pulse in an underdense plasma [79]. The first and second terms on the right-hand side of Eq. (5.32) represent the vacuum diffraction and channel guiding respectively; while the third term on the right-hand side $-4\hat{P}/(k^2 r_s^3)$ represents relativistic self-focusing due to the index of refraction change caused by the relativistic energy increase of the electrons in presence of the laser pulse. The integral on the right-hand side of Eq. (5.32) represents the nonlinear coupling of the laser envelope to a plasma wave.

For long axially uniform laser pulses, plasma wave generation can be neglected, and Eq. (5.32) indicates that the condition for matched beam propagation (i.e., propagation with constant spot size) is

$$1 = \Delta_c \left(r_s/r_c\right)^4 + \hat{P} \,. \quad (5.33)$$

In a homogeneous plasma ($\Delta_c = 0$), guiding requires the power be equal to the critical power $\hat{P} = 1$, which is the condition for relativistic self-focusing [15]. As discussed

in Chapter 2, relativistic self-focused long laser pulses are subject to leading-edge erosion and self-modulation. For low laser power $\hat{P} \ll 1$, guiding of a matched laser pulse $r_s = r_c$ can be achieved by a plasma density channel with depth equal to the critical plasma density channel depth $\Delta_c = 1$ or $\Delta n = \Delta n_c = (\pi r_e r_c^2)^{-1}$ [36].

For short laser pulses ($L < k_p^{-1}$), the integral on the right-hand side of Eq. (5.32) reduces to $\simeq 4\hat{P}/(k^2 r_s^3)$, and therefore the plasma wave response will tend to cancel the relativistic self-focusing term. Consequently, relativistic self-focusing is ineffective in preventing diffraction in short pulses [36].

For propagation in vacuum ($k_p = 0$, $\hat{P} = 0$, and $\Delta_c = 0$), the solution to Eq. (5.32) yields the conventional vacuum mode $r_s = r_0[1 + (z/Z_R)^2]^{1/2}$ (assuming the initial conditions $r_s = r_0$ and $\dot{r}_s = 0$ at $z = 0$), which is the first order diffraction of a laser pulse in vacuum [35].

5.2.4 Adiabatic Plasma Response

In the regime where the plasma responds adiabatically (i.e., the pulse length is long compared to the plasma wavelength $L \gg k_p^{-1}$), the plasma response Eq. (5.6) reduces to $\delta\hat{n} \simeq -\hat{a}^2/2$ such that the wave equation Eq. (5.11) contains a cubic nonlinearity and coupling of the laser pulse to the plasma wave is neglected (e.g., forward Raman scattering is neglected). In this limit, Eqs. (5.30) and (5.31) reduce to

$$G^{(3)} = \frac{2\hat{P}}{k^2 r_s^2}\left[\theta' - k + \frac{\alpha'}{4} - (\alpha + 3i)\frac{r_s'}{2r_s} - 3i\frac{a_r'}{a_r}\right] \tag{5.34}$$

$$H^{(3)} = \frac{\hat{P}}{k^2 r_s^2}\left(\theta' - k - 3i\frac{a_r'}{a_r}\right) . \tag{5.35}$$

Inserting the imaginary part of G into the laser power envelope equation Eq. (5.25) yields

$$\frac{\partial}{\partial z}\hat{P} + \frac{\partial}{\partial \xi}\left(\delta\beta_g \hat{P}\right) = 0 , \tag{5.36}$$

where

$$\delta\beta_g = \frac{2}{k^2 r_c^2} - \frac{(1+\alpha^2)}{k^2 r_s^2} - \frac{\Delta_c}{k^2 r_c^2}\frac{r_s^2}{r_c^2} + \frac{3\hat{P}}{k^2 r_s^2} . \tag{5.37}$$

Therefore the local group velocity of the laser pulse is $\beta_g \simeq \beta_{g0} + \delta\beta_g(z,\xi)$. Note that in the linear limit $|a_r| \ll 1$, the group velocity for a matched pulse ($r_s = r_c$, $\alpha = 0$, and $\Delta_c = 1$) reduces to $\beta_g \simeq \beta_{g0}$. The power conservation equation Eq. (5.36) implies the total pulse energy is conserved,

$$\frac{\partial}{\partial z}\int d\xi \hat{P} = 0. \tag{5.38}$$

For the general non-adiabatic case, pulse energy is not conserved since the pulse energy is converted into plasma wave energy.

5.2.5 Low-Power Adiabatic Limit

Solutions to the envelope equations for the evolution of the laser field parameters in the low-power $\hat{P} \ll 1$ adiabatic regime can be examined by perturbing about the zero-power matched-pulse equilibrium: $\Delta_c = 1$ and $r_0 = r_c$. Let $r_s = r_0 + \delta r_s$, $\alpha = \delta\alpha$, $a_r = a_{r0}(\xi) + \delta a_r$, and $\theta = \delta\theta$, where $\delta f/f \sim \hat{P} \ll 1$ for any laser field parameter f.

Betatron Oscillation Damping

The envelope equations Eqs. (5.20) and (5.21) can be linearized and combined to yield an equation for the evolution of the spot size perturbation

$$\left[\left(\frac{\partial}{\partial z} - \frac{4}{k^2 r_0^2}\right)^2 + \frac{16}{k^2 r_0^4}\right] a_{r0}\frac{\delta r}{r_0} \simeq -\frac{4}{k^2 r_0^4}\hat{P} a_{r0}\,, \tag{5.39}$$

where $\hat{P} = \hat{P}(\xi) = k_p^2 r_0^2 a_{r0}^2(\xi)/16$ is the unperturbed initial axial power profile. Assuming the initial conditions $\delta r(z=0) = \delta r_0$ and $\delta r'(z=0) = 0$, Eq. (5.39) has the solution

$$\frac{\delta r_s}{r_0} = \frac{a_{r0}(\sigma)}{a_{r0}(\xi)}\left[\frac{\delta r_0}{r_0} + \frac{\hat{P}(\sigma)}{4}\right]\cos\left(\frac{2z}{Z_R}\right) - \frac{\hat{P}(\xi)}{4}\,, \tag{5.40}$$

where $\sigma = \xi + 4z/(k^2 r_0^2)$. For a Gaussian axial laser pulse power profile $\hat{P} = \hat{P}_0 \exp(-2\xi^2/L^2)$ with peak laser power $\hat{P}_0$, Eq. (5.40) becomes

$$\frac{\delta r_s}{r_0} = \left\{ \frac{\delta r_0}{r_0} \exp\left[-\left(\frac{2z\xi}{Z_\beta L} + \frac{z^2}{Z_\beta^2} \right) \right] + \frac{\hat{P}}{4} \exp\left[-3\left(\frac{2z\xi}{Z_\beta L} + \frac{z^2}{Z_\beta^2} \right) \right] \right\} \cos(k_\beta z) - \frac{\hat{P}}{4}, \tag{5.41}$$

where $Z_\beta = kLZ_R/2 = k^2 r_0^2 L/4$ is the betatron damping distance, and $k_\beta = 2/Z_R = 4/(kr_0^2)$ is the betatron wavenumber.

In the linear limit ($\hat{P} \simeq 0$), Eq. (5.41) describes the damping of betatron oscillations for a laser pulse mismatched ($\delta r_0 \neq 0$) in the plasma channel [81]. Asymptotically, these oscillations damp $\delta r_s \sim \exp(-z^2/Z_\beta^2)$ for fixed laser beam slice ξ, with a head-tail asymmetry. For finite powers, betatron oscillations arise even with no initial displacement $\delta r_0 = 0$, with the enhanced damping rate $\delta r_s \sim \exp(-3z^2/Z_\beta^2)$. This is the case since a pulse with $\hat{P} > 0$ is no longer matched when $r_0 = r_c$ in a channel with $\Delta_c = 1$. For large z, Eq. (5.41) reduces to $r_s/r_0 \simeq 1 - \hat{P}/4$. Recall that paraxial theory predicts that the local condition for matching a laser pulse within a plasma channel is given by Eq. (5.33), i.e., a matched radius of $r_s = r_c[\Delta_c^{-1}(1-\hat{P})]^{1/4}$. In the limit $\hat{P} \ll 1$ near equilibrium ($\Delta_c = 1$ and $r_0 = r_c$), the matched radius reduces to $r_s/r_0 \simeq 1 - \hat{P}/4$, which is the asymptotic behavior ($z \gg Z_\beta$) given by Eq. (5.41).

The physical mechanism for the damping present in Eq. (5.41) is phase-mixing. A finite pulse length will introduce a spread in laser wavenumber. Since the betatron wavenumber depends on the wavenumber spectrum of the laser pulse, a spread in wavenumber will lead to a spread in k_β (i.e., different frequencies will undergo betatron oscillations in the channel with different periods), and this will lead to phase-mixing and decoherence damping of the betatron oscillations.

Pulse Self-Steepening

For a matched pulse in the low-power adiabatic limit, Eq. (5.37) reduces to $\delta\beta_g \simeq 3\hat{P}/(kr_0)^2$ and the laser power evolution Eq. (5.36) is

$$\frac{\partial \hat{P}}{\partial z} + \frac{6\hat{P}}{k^2 r_0^2}\frac{\partial \hat{P}}{\partial \xi} \simeq 0 \,. \tag{5.42}$$

Equation 5.42 has the solution $\hat{P} = \hat{P}_i(\xi - 6\hat{P}z/(kr_0)^2)$, where $\hat{P}_i$ is the initial distribution in laser power [e.g., $\hat{P}_i(\xi) = \hat{P}_0 \exp(-2\xi^2/L^2)$ for an initial Gaussian distribution with peak laser power $\hat{P}_0$]. Physically, Eq. (5.42) describes the distortion of the laser pulse power profile (pulse self-steepening) owing to the fact that the local group velocity is dependent on the local power (i.e., the higher the local power, the higher the local group velocity, and the power is shifted forward within the laser pulse). In the absence of the dispersive pulse broadening due to the term $\gamma_{g0}^{-2}\partial_\xi^2 \hat{a}$ in Eq. (5.9), pulse steepening continues until a shock is formed (i.e., $\partial_\xi \hat{P} \to \infty$). This puts a limit on the validity of this theory to the propagation distance of shock formation. Shock formation occurs after a distance $z = Z_S$, where Z_S is the shock formation length [e.g., $Z_S = (e^{1/2}/6)kLZ_R/\hat{P}_0$ for a Gaussian axial laser pulse power distribution].

Self-Phase Modulation

Self-phase modulation (phase distortions) will also develop in the laser pulse. For a matched pulse in the low-power adiabatic limit, the envelope equation Eq. (5.22) reduces to

$$\frac{\partial}{\partial z}\delta\theta \simeq \frac{4}{kr_0^2}\left(\frac{\delta r_s}{r_0} - \frac{3}{4}\hat{P}\right) , \tag{5.43}$$

which results in local frequency shifts $\delta\omega/\omega = \delta\theta'/k$. Asymptotically ($z \gg Z_\beta$), Eq. (5.43) reduces to $\delta\dot{\theta} \simeq -2\hat{P}/Z_R$ [recall from Eq. (5.41), $\delta r_s/r_0 \simeq -\hat{P}/4$ for $z \gg Z_\beta$], which implies the asymptotic local frequency shifts $\delta\omega/\omega \simeq (2/3)\ln[\hat{P}/\hat{P}(z=0)]$.

5.2.6 Laser-Plasma Instabilities

Laser-plasma instabilities can limit the laser pulse propagation distance and degrade the performance of a laser-driven plasma-based accelerators. These instabilities for finite pulse length and finite-radius laser pulses can be examined by perturbing the full envelope equations Eqs. (5.19)-(5.22) about an optically-guided matched-pulse equilibrium: $1 = \hat{P} + \Delta_c$, $r_s = r_0 = r_c$, $a_r = a_0$, $\theta = 0$, and $\alpha = 0$, where a_0 and r_0 are constants (i.e., a flat-top axial laser pulse profile). Assuming a perturbation from equilibrium such that $r_s = r_0 + \delta r$, $a_r = a_0 + \delta a$, $\theta = \delta\theta$, and $\alpha = \delta\alpha$, Eqs. (5.19)-(5.21) can be linearized and combined to yield

$$\left[\left(\frac{\partial}{\partial z} - \frac{4\Delta_c}{k^2 r_0^2}\frac{\partial}{\partial \xi}\right)^2 + \frac{8(1+\Delta_c)}{k^2 r_0^4}\right]\left(1 + k_p^{-2}\frac{\partial}{\partial \xi^2}\right)\frac{\delta r}{r_0} = \frac{2\hat{P}_0}{k^2 r_0^2}\left[\left(\frac{\partial}{\partial z} - \frac{4\Delta_c}{k^2 r_0^2}\frac{\partial}{\partial \xi}\right)\frac{\partial}{\partial \xi} - \frac{4}{r_0^2}\right]\frac{\delta a}{a_0} \quad (5.44)$$

and

$$\left[\left(\frac{\partial}{\partial z} + \frac{3\hat{P}_0}{k^2 r_0^2}\frac{\partial}{\partial \xi}\right)\left(1 + k_p^{-2}\frac{\partial}{\partial \xi^2}\right) + \frac{4\hat{P}_0}{k^2 r_0^2}\frac{\partial}{\partial \xi}\right]\frac{\delta a}{a_0} = -\left[\left(\frac{\partial}{\partial z} + \frac{3\hat{P}_0}{k^2 r_0^2}\frac{\partial}{\partial \xi}\right)\left(1 + k_p^{-2}\frac{\partial}{\partial \xi^2}\right) + \frac{2\hat{P}_0}{k^2 r_0^2}\frac{\partial}{\partial \xi}\right]\frac{\delta r}{r_0}, \quad (5.45)$$

where $\hat{P}_0 = k_p^2 a_0^2 r_0^2/16$ is the initial normalized laser pulse power.

Considering modes resonant with the plasma wave such that the perturbed quantities have a phase dependence $\delta r = \delta\hat{r}\exp(ik_p\xi)$ and $\delta a = \delta\hat{a}\exp(ik_p\xi)$, with the eikonal approximations $|\partial\hat{r}/\partial\xi| \ll |k_p\delta\hat{r}|$ and $|\partial\hat{a}/\partial\xi| \ll |k_p\delta\hat{a}|$, Eqs. (5.44) and (5.45) become

$$\left(\frac{\partial^2}{\partial z^2} + k_\beta^2\right)\frac{\partial}{\partial \xi}\frac{\delta\hat{r}}{r_0} = i\hat{P}_0\frac{k_p}{Z_R^2}\frac{\delta\hat{a}}{a_0} \quad (5.46)$$

and

$$\left(\frac{\partial^2}{\partial z \partial \xi} + \frac{k_p^2\hat{P}_0}{kZ_R}\right)\frac{\delta\hat{a}}{a_0} = -\left(\frac{\partial^2}{\partial z \partial \xi} + \frac{k_p^2\hat{P}_0}{2kZ_R}\right)\frac{\delta\hat{r}}{r_0}, \quad (5.47)$$

where $k_\beta^2 = 2(1+\Delta_c)/Z_R^2$ is the generalized betatron wavenumber. In the one-dimensional limit (i.e., the limit of infinite spot size, $r_0 \to \infty$), Eq. (5.47) reduces

to

$$\left(\frac{\partial^2}{\partial z \partial \xi} + \Gamma_R^2\right) \frac{\delta \hat{a}}{a_0} = 0 \,, \tag{5.48}$$

where $\Gamma_R = a_0 k_p^2/(2\sqrt{2}k)$ is the well-known growth rate for Raman scattering in the four-wave regime [45]. Equation (5.48) describes conventional forward Raman scattering and has the solution [85]

$$\delta \hat{a} = \delta \hat{a}_0 I_0 \left(2\Gamma_R \sqrt{z|\xi|}\right) \,, \tag{5.49}$$

where I_0 is the zeroth-order modified Bessel function of the second kind and $\delta \hat{a}_0$ is the initial condition. In the two-dimensional paraxial limit, Eq. (5.47) reduces to $\delta \hat{a}/a_0 \simeq -\delta \hat{r}/r_0$ (i.e., the laser power is conserved in the paraxial limit), and Eq. (5.46) reduces to

$$\left[\frac{\partial}{\partial \xi}\left(\frac{\partial^2}{\partial z^2} + k_\beta^2\right) + i\hat{P}\frac{k_p}{Z_R^2}\right] \delta \hat{r} = 0 \,. \tag{5.50}$$

Equation (5.50) describes the conventional self-modulation instability [79, 86]. In the self-modulation instability, modulation of the laser pulse is produced through radial transport of laser energy; whereas, in the forward Raman scattering instability, laser modulation is produced via axial transport of laser energy. Therefore forward Raman scattering will dominate in the one-dimensional limit, i.e., when $k_p r_0 \gg k/k_p$ is satisfied.

For the general case, Eqs. (5.46) and (5.47) can be combined to yield

$$\left(\frac{\partial^2}{\partial \hat{\xi} \partial \hat{z}} + \hat{k}_p \hat{P}_0\right)\left[\left(\frac{\partial^2}{\partial \hat{z}^2} + \hat{k}_\beta^2\right)\frac{\partial}{\partial \hat{\xi}} + i\hat{P}\right] \delta \hat{r} = i\hat{k}_p \frac{\hat{P}_0^2}{2} \delta \hat{r} \,, \tag{5.51}$$

with the normalized quantities: $\hat{\xi} = k_p \xi$, $\hat{z} = z/Z_R$, $\hat{k}_p = k_p/k$, and $\hat{k}_\beta^2 = 2(1 + \Delta_c)$. Equation (5.51) describes the nonlinear coupling of the two laser-plasma instabilities: forward Raman scattering [21, 85] and self-modulation [79, 86]. Asymptotic expressions for the exponentiation in various spatial-temporal regimes can be solved using Eq. (5.51). Table 5.1 shows the asymptotic expressions for the number of e-folds N_e, where $\delta r \sim \exp(N_e)$. The table lists the growth rates of forward Raman

Instability	Regime	N_e = number of e-folds
S-SMI	$\hat{P}/(2\hat{k}_\beta) \ll \lvert\hat{\xi}\rvert/\hat{z} \ll 2\hat{k}_\beta^3/\hat{P}$	$(2\hat{P}\lvert\hat{\xi}\rvert\hat{z}/\hat{k}_\beta)^{1/2}$
I-SMI	$\hat{k}_\beta^3/(2\hat{P}) \ll \lvert\hat{\xi}\rvert/\hat{z} \ll 1/(2\hat{P}\hat{k}_p^3)$	$(1+i3^{-1/2})3^{3/2}2^{-5/2}(\hat{P}\lvert\hat{\xi}\rvert\hat{z}^2)^{1/3}$
L-SMI	$1/(\hat{P}\hat{k}_p^3) \ll \lvert\hat{\xi}\rvert/\hat{z}$	$(1+i3^{-1/2})3^{3/2}2^{-5/2}(\hat{P}\lvert\hat{\xi}\rvert\hat{z}^2/2)^{1/3}$
S-FRS	$\hat{k}_p\hat{P} \ll \lvert\hat{\xi}\rvert/\hat{z} \ll \hat{k}_p\hat{k}_\beta^4/\hat{P}$	$(4\hat{k}_p\hat{P}\lvert\hat{\xi}\rvert\hat{z})^{1/2}$
I-FRS	$2\hat{k}_p\hat{k}_\beta^4/\hat{P} \ll \lvert\hat{\xi}\rvert/\hat{z} \ll 2/(\hat{P}\hat{k}_p^3)$	$(2\hat{k}_p\hat{P}\lvert\hat{\xi}\rvert\hat{z})^{1/2}$
L-FRS	$1/(\hat{P}\hat{k}_p^3) \ll \lvert\hat{\xi}\rvert/\hat{z}$	$(4\hat{k}_p\hat{P}\lvert\hat{\xi}\rvert\hat{z})^{1/2}$

Table 5.1: Asymptotic growth rates for forward Raman scattering (FRS) and self-modulation instability (SMI) in the short (S), intermediate (I), and long (L) laser pulse length regimes.

scattering (FRS) and the self-modulation instability (SMI) in the short pulse length (S), intermediate (I), and long pulse length (L) regimes. Reduced growth rates are found in the long pulse length regime of the self-modulation instability and in the intermediate pulse regime of the forward Raman scattering instability. As Table 5.1 indicates, the self-modulation instability dominates the forward Raman scattering instability in the intermediate and short pulse length regimes assuming $\hat{k}_\beta\hat{k}_p < 1/2$. The forward Raman scattering instability dominates the self-modulation instability in the long pulse regime, although growth is significant only in the tail of the long pulse, i.e., for $|\hat{\xi}| \gg 1/(2\hat{k}_p^2\hat{P})$.

5.3 Summary

In summary, a nonlinear theory of finite-radius laser pulse propagation has been developed which includes finite pulse length and nonlinear effects. The results

presented in this chapter are valid for laser pulse propagation in parabolic plasma density channels as well as in homogeneous plasmas ($\Delta_c = 0$). Coupled laser envelope equations Eqs. (5.19)-(5.22) have been derived for the laser pulse parameters, and solutions indicate that finite pulse length effects can significantly modify the propagation of the laser field in an underdense plasma.

For an adiabatic plasma response, pulse energy conservation was shown and the nonlinear laser pulse group velocity calculated. In the low-power adiabatic limit, the effects of damped betatron oscillations due to phase-mixing, laser pulse self-steepening owing to nonlinear group velocity effects, and self-phase modulation were analyzed. For the general non-adiabatic plasma response, the nonlinear coupling of forward Raman scattering and the self-modulation instability was studied and the asymptotic growth rates were derived in various spatial-temporal regimes.

Chapter 6

Conclusions

In this chapter, the theoretical results presented in this dissertation are summarized. Possible future theoretical and computational work is considered. Practical applications and future experimental tests of the results presented in this work are discussed.

6.1 Summary

This dissertation essentially answers three questions:

1. What is the performance of an accelerating structure based on a hollow plasma channel?
2. Under what conditions is trapping of background plasma electrons in a plasma wave by a beat wave possible, and what is the quality of the resulting electron bunch?
3. What are the dynamics of ultrashort high-power laser pulses propagating in underdense plasmas?

The answer to Question 1 is quantified in the calculation of the mode frequencies (eigenvalues) and loss factors (eigenfunctions) of the electromagnetic modes

excited in the hollow plasma channel presented in Chapter 2. These accelerator parameters quantify the beam-structure interaction. The dynamics of charged particle beams propagating through a hollow plasma channel structure were analyzed in Chapter 3. Transverse beam breakup instability growth rates were calculated in the weak-focusing and strong-focusing regimes for both witness and drive particle beams.

Question 2 is answered in the Hamiltonian analysis and numerical simulations presented in Chapter 4. The laser-plasma parameters required for trapping background plasma electrons oscillating in a plasma wave using colliding laser pulses were derived. Numerical simulations were used to study the quality and dynamics of the generated electron bunches. This analysis indicates that the colliding laser pulse injection scheme has the capability to produce relativistic femtosecond electron bunches with fractional energy spread of order a few percent and normalized transverse emittance less than 1 mm mrad using 1 terawatt injection laser pulses.

The answer to Question 3 lies in the formulae of Chapter 5. In Chapter 5, a non-paraxial theory of laser pulse propagation is presented which includes finite pulse length and nonlinear effects. Finite pulse length effects become significant for the ultrashort laser pulses used in the laser wakefield accelerator. The evolution of the laser pulse was described by envelope equations for the laser pulse parameters. In the adiabatic plasma response regime, nonlinear group velocity corrections, betatron oscillation damping, pulse-steepening, and self-phase modulation were studied. For the general non-adiabatic plasma response, laser-plasma instabilities were examined, and growth rates for the forward Raman scattering and self-modulation instabilities were calculated.

6.2 Future Directions

This dissertation advances the theory of plasma-based accelerators as summarized in Sec. 6.1. Much further theoretical work can be done of course. In

particular, non-symmetric fully electromagnetic three-dimensional (or at least two-dimensional) particle-in-cell simulations of the interaction between the particle beam and the plasma channel can be done to further verify the analytical results of Chapters 2 and 3.

In the analysis of the generation of ultrashort electron bunches using colliding laser pulses presented in Chapter 4, the plasma wave was derived to first-order in laser intensity. For high-intensity laser pulses ($a \gtrsim 1$) this approximation is no longer valid, and nonlinear effects (e.g., quasistatic magnetic field generation [87]) will modify the plasma wave fields Eqs. (4.33) and (4.34). For large plasma waves, the transverse fields may blow-out a large fraction of plasma electrons. Therefore, incorporation of the ionic space-charge forces into the analysis will also be necessary in the high laser intensity regime.

The non-paraxial theory of laser pulse propagation presented in Chapter 5 is valid for the parameter regime of typical laser wakefield accelerator experiments. In particular, the theory is restricted to laser pulse propagation in underdense plasmas within the shock formation length. It is possible to extend the theory and relax these constraints by inclusion of the dispersive term $\gamma_{g0}^{-2}\partial_\xi^2\hat{a}$ as an additional source term in the paraxial wave equation Eq. (5.11). Numerical solution of the exact wave equation Eq. (5.1) can also be done, allowing comparisons with the analytic results presented in Chapter 5.

6.3 Prospects

To some extent the usefulness of this theoretical work is in laying the groundwork for proposing and planning practical experiments. Given the availability of terawatt lasers and the recent experimental advances in plasma channel production and laser guiding, particularly the experiments with plasma channels produced by capillary discharge [44, 43], there is every reason to proceed with practical experiments of an accelerator based on the hollow plasma channel structure. With

laser diffraction overcome through optical guiding provided by the plasma channel, the transverse stability of the accelerated particle beam may limit the length of an accelerator based on the hollow plasma channel structure. Such a plasma structure would be an extremely compact accelerator producing GeV-energy particle beams. A hollow plasma channel accelerating structure might also be envisioned as a single stage at the end of a conventional linear accelerator.

Plans to experimentally test and implement the optical injection method of ultrashort electron bunch generation described in Chapter 4 are currently underway at Lawrence Berkeley National Laboratory [88]. Such femtosecond electron bunches, injected into a plasma-based accelerator, could be used for high-energy physics applications. There are other possible applications for femtosecond electron bunches. Generation of femtosecond duration x-ray pulses can be done through Thomson scattering a high-intensity laser beam off such femtosecond relativistic electron beams [89]. Femtosecond x-ray pulses could have important applications to atomic and condensed matter research.

Laser technology advances, producing shorter laser pulse durations and higher laser intensities, have allowed for the experimental realization of laser-driven plasma-based accelerators such as the laser wakefield accelerator. Indeed ultrashort high-intensity laser pulses have many applications, in addition to plasma-based accelerators, for which the understanding of the physics of ultrashort laser pulse propagation in plasmas becomes critical. Some of these applications include harmonic generation [74, 75], short wavelength radiation sources [76, 77], and laser-fusion schemes [78]. Chapter 5 presents a theory of finite-radius laser pulse propagation in underdense plasmas that includes finite pulse length effects, which become significant in such ultrashort laser-plasma interactions.

In reviewing the work published on plasma-based accelerators in the last twenty years since the paper by Tajima and Dawson [4], one realizes the large amount of experimental and theoretical progress that has occured in this field. Although the challenges are still great, plasma-based accelerators hold the promise for the next

generation accelerators and for ever higher energy particle beams.

Bibliography

[1] J. S. Wurtele. "The role of plasma in advanced accelerators". *Phys. Fluids B*, 5(7):2363–2369, 1993.

[2] J. S. Wurtele. "Advanced accelerator concepts". *Phys. Today*, 47(7):33–40, July 1994.

[3] E. Esarey, P. Sprangle, J. Krall, and A. Ting. "Overview of Plasma-Based Accelerator Concepts". *IEEE Trans. Plasma Sci.*, PS-24(2):252–288, 1996.

[4] T. Tajima and J. Dawson. "Laser Electron Accelerator". *Phys. Rev. Lett.*, 43(4):267–270, 1979.

[5] J. R. Marqués, F. Dorchies, F. Amiranoff, P. Audebert, J. C. Gauthier, J. P. Geindre, A. Antonetti, T. M. Antonsen, P. Chessa, and P. Mora. "Laser wakefield: Experimental study of nonlinear radial electron oscillations". *Phys. Plasmas*, 5(4):1162–1177, 1998.

[6] F. Amiranoff, S. Baton, D. Bernard, B. Cros, D. Descamps, F. Dorchies, F. Jacquet, V. Malka, J. R. Marqués, G. Matthieussent, P. Miné, A. Modena, P. Mora, J. Morillo, and Z. Najmudin. "Observation of Laser Wakefield Acceleration of Electrons". *Phys. Rev. Lett.*, 81(5):995–998, 1998.

[7] D. Strickland and G. Mourou. "Compression of amplified chirped optical pulses". *Opt. Commun.*, 56(3):219–221, 1985.

[8] P. Maine, D. Strickland, P. Bado, M. Pessot, and G. Mourou. "Generation of ultrahigh peak power pulses by chirped-pulse amplification". *IEEE J. Quantum Electron.*, QE-24(2):398–403, 1988.

[9] M. D. Perry and G. Mourou. "Terawatt to petawatt subpicosecond lasers". *Sci.*, 264(5161):917–924, 1994.

[10] C. E. Clayton, C. Joshi, C. Darrow, and D. Umstadter. "Relativistic plasma wave excitation by collinear optical mixing". *Phys. Rev. Lett.*, 54(21):2343–2346, 1985.

[11] Y. Kitagawa, T. Matsumoto, T. Minamihata, K. Sawai, K. Matsuo, K. Mima, K. Nishihara, H. Azechi, K. A. Tanaka, H. Takabe, and S. Nakai. "Beat-wave excitation of plasma wave and observation of accelerated electrons". *Phys. Rev. Lett.*, 68(1):48–51, 1992.

[12] C. E. Clayton, M. J. Everett, A. Lal, D. Gordon, K. A. Marsh, and C. Joshi. "Acceleration and scattering of injected electrons in plasma beatwave accelerator experiments". *Phys. Plasmas*, 1(5):1753–1760, 1994.

[13] F. Amiranoff, D. Bernard, B. Cros, F. Jacquet, G. Matthieussent, P. Miné, P. Mora, J. Morillo, F. Moulin, A. E. Specka, and C. Stenz. "Electron acceleration in Nd-laser plasma beat-wave experiments". *Phys. Rev. Lett.*, 74(26):5220–5223, 1995.

[14] M. N. Rosenbluth and C. S. Liu. "Excitation of Plasma Waves by Two Laser Beams". *Phys. Rev. Lett.*, 29(11):701–705, 1972.

[15] G.-Z. Sun, E. Ott, Y. C. Lee, and P. Guzdar. "Self-focusing of short intense pulses in plasmas". *Phys. Fluids*, 30(2):526–532, 1987.

[16] C. Coverdale, C. B. Darrow, C. D. Decker, W. B. Mori, K.-C. Tzeng, K. A. Marsh, C. E. Clayton, and C. Joshi. "Propagation of intense subpicosecond

laser pulses through underdense plasmas". *Phys. Rev. Lett.*, 74(23):4659–4662, 1995.

[17] K. Nakajima, D. Fisher, T. Kawakubo, H. Nakanishi, A. Ogata, Y. Kato, Y. Kitagawa, R. Kodama, K. Mima, H. Shiraga, K. Suzuki, K. Yamakawa, T. Zhang, Y. Sakawa, T. Shoji, Y. Nishida, N. Yugami, M. Downer, and T. Tajima. "Observation of ultrahigh gradient electron acceleration by a self-modulated intense short laser pulse". *Phys. Rev. Lett.*, 74(22):4428–4431, 1995.

[18] A. Modena, Z. Najmudin, A. E. Dangor, C. E. Clayton, K. A. Marsh, C. Joshi, V. Malka, C. B. Darrow, and C. Danson. "Observation of Raman Forward Scattering and Electron Acceleration in the Relativistic Regime". *IEEE Trans. Plasma Sci.*, PS-24(2):289–295, 1996.

[19] R. Wagner, S. Y. Chen, A. Maksimchuk, and D. Umstadter. "Electron Acceleration by a Laser Wakefield in a Relativistically Self-Guided Channel". *Phys. Rev. Lett.*, 78(16):3125–3128, 1997.

[20] A. Ting, C. I. Moore, K. Krushelnick, C. Manka, E. Esarey, P. Sprangle, R. Hubbard, H. R. Burris, R. Fischer, and M. Baine. "Plasma wakefield generation and electron acceleration in a self-modulated laser wakefield accelerator experiment". *Phys. Plasmas*, 4(5):1889–1899, 1997.

[21] T. M. Antonsen and P. Mora. "Self-focusing and Raman scattering of laser pulses in tenuous plasmas". *Phys. Fluids B*, 5(5):1440–1452, 1993.

[22] P. Sprangle, J. Krall, and E. Esarey. "Hose-Modulation Instability of Laser Pulses in Plasmas". *Phys. Rev. Lett.*, 73(26):3544–3547, 1994.

[23] K. Nakajima, M. Kando, H. Ahn, H. Kotaki, T. Watanabe, T. Ueda, M. Uesaka, H. Nakanishi, A. Ogata, T. Kawakubo, and K. Tani. "Recent Results of Laser Wakefield Acceleration in KEK/U. Tokyo/JAERI". In S. Chattopadhyay,

J. McCullough, and P. Dahl, editors, *Advanced Accelerator Concepts: Seventh Workshop*, pages 83–95, New York, 1996. AIP.

[24] J. B. Rosenzweig, D. B. Cline, B. Cole, H. Figueroa, W. Gai, R. Konecny, J. Norem, P. Schoessow, and J. Simpson. "Experimental observation of plasma wakefield acceleration". *Phys. Rev. Lett.*, 61(1):98–101, 1988.

[25] J. B. Rosenzweig, P. Schoessow, B. Cole, W. Gai, R. Konecny, J. Norem, and J. Simpson. "Experimental measurement of nonlinear plasma wakefields". *Phys. Rev. A*, 39(3):1586–1589, 1989.

[26] H. Nakanishi, A. Enomoto, A. Ogata, K. Nakajima, D. Whittum, Y. Yoshida, T. Ueda, T. Kobayashi, H. Shibata, S. Tagawa, N. Yugami, and Y. Nishida. "Wakefield accelerator using twin linacs". *Nucl. Instrum. Meth.*, A328(3):596–598, 1993.

[27] A. K. Berezin, Ya. B. Fainberg, V. A. Kiselev, A. F. Linnik, V. V. Uskov, V. A. Balakirev, I. N. Onishchenko, G. L. Sidel'nikov, and G. V. Sotnikov. "Wake field excitation in plasma by a relativistic electron pulse with a controlled number of short bunches". *Plasma Phys. Rep.*, 20(7):569–602, 1994.

[28] D. H. Whittum. "Transverse two-stream instability of a beam with a Bennett profile". *Phys. Plasmas*, 4(4):1154–1159, 1997.

[29] D. H. Whittum, W. M. Sharp, S. S. Yu, M. Lampe, and G. Joyce. "Electron-hose instability in the ion-focused regime". *Phys. Rev. Lett.*, 67(8):991–994, 1991.

[30] R. D. Ruth, A. W. Chao, P. L. Morton, and P. B. Wilson. "A plasma wakefield accelerator". *Part. Accel.*, 17(3):171–189, 1985.

[31] R. Assmann, P. Chen, F.-J. Decker, R. Iverson, M. J. Hogan, S. Rokni, R. H. Siemann, D. Walz, D. H. Whittum, P. Catravas, S. Chattopadhyay, E. Esarey, W. P. Leemans, P. Volfbeyn, C. Clayton, R. Hemker, C. Joshi, K. Marsh, W. B.

Mori, S. Wang, T. Katsouleas, S. Lee, and P. Muggli. "Progress toward E-157: A 1 GeV plasma wakefield accelerator". In *Proceedings of the Particle Accelerator Conference*, pages 330–332, New York, 1999. IEEE.

[32] D. R. Nicholson. *Introduction to Plasma Theory*. Krieger Publishing Co., 1992.

[33] J. D. Jackson. *Classical Electrondynamics*. Wiley, 1975.

[34] R. Keinings and M. E. Jones. "Two-dimensional dynamics of the plasma wakefield accelerator". *Phys. Fluids*, 30(1):252–263, 1987.

[35] A. E. Siegman. *Lasers*. University Science Books, 1986.

[36] P. Sprangle, E. Esarey, J. Krall, and G. Joyce. "Propagation and guiding of intense laser pulses in plasmas". *Phys. Rev. Lett.*, 69(15):2200–2203, 1992.

[37] T. C. Chiou, T. Katsouleas, C. Decker, W. B. Mori, J. S. Wurtele, G. Shvets, and J. J. Su. "Laser wake-field acceleration and optical guiding in a hollow plasma channel". *Phys. Plasmas*, 2(1):310–318, 1995.

[38] K. Krushelnick, A. Ting, C. I. Moore, H. R. Burris, E. Esarey, P. Sprangle, and M. Baine. "Plasma Channel Formation and Guiding during High Intensity Short Pulse Laser Plasma Experiments". *Phys. Rev. Lett.*, 78(21):4047–4050, 1997.

[39] C. G. Durfee III and H. M . Milchberg. "Light pipe for high intensity laser pulses". *Phys. Rev. Lett.*, 71(15):2409–2411, 1993.

[40] C. G. Durfee III, J. Lynch, and H. M . Milchberg. "Development of a plasma waveguide for high-intensity laser pulses". *Phys. Rev. E*, 51(3):2368–2388, 1995.

[41] E. W. Gaul, S. P. Le Blanc, and M. C. Downer. "Efficient Excitation and Measurement of Plasma Channels". In W. Lawson, C. Bellamy, and D. F. Brosius, editors, *Advanced Accelerator Concepts: Eighth Workshop*, pages 377–383, New York, 1998. AIP.

[42] P. Volfbeyn, E. Esarey, and W. P. Leemans. "Guiding of laser pulses in plasma channels created by the ignitor-heater technique". *Phys. Plasmas*, 6(5):2269–2277, 1999.

[43] D. Kaganovich, A. Ting, C. I. Moore, A. Zigler, H. R. Burns, Y. Ehrlich, R. Hubbard, and P. Sprangle. "High efficiency guiding of terawatt subpicosecond laser pulses in a capillary discharge plasma channel". *Phys. Rev. E*, 59(5):R4769–R4772, 1999.

[44] Y. Ehrlich, C. Cohen, A. Zigler, J. Krall, P. Sprangle, and E. Esarey. "Guiding of High Intensity Laser Pulses in Straight and Curved Plasma Channel Experiments". *Phys. Rev. Lett.*, 77(20):4186–4189, 1996.

[45] W. Kruer. *The Physics of Laser Plasma Interactions.* Addison-Wesley, 1988.

[46] G. Shvets, J. S. Wurtele, T. C. Chiou, and T. C. Katsouleas. "Excitation of Accelerating Wakefields in Inhomogeneous Plasmas". *IEEE Trans. Plasma Sci.*, PS-24(2):351–362, 1996.

[47] C. B. Schroeder, D. H. Whittum, and J. S. Wurtele. "Multimode Analysis of the Hollow Plasma Channel Wakefield Accelerator". *Phys. Rev. Lett.*, 82(6):1177–1180, 1999.

[48] M. Reiser. *Theory and Design of Charged Particle Beams.* Wiley, 1994.

[49] P. Wilson. "Linear Accelerators for TeV Colliders". In C. Joshi and T. Katsouleas, editors, *Laser Acceleration of Particles*, pages 560–597, New York, 1985. AIP.

[50] R. Assmann, F. J. Decker, M. Seidel, R. H. Siemann, and D. H. Whittum. "Observation of dark-current signals from the S-band structures of the SLAC LINAC". In *Proceedings of the Particle Accelerator Conference*, New York, 1997. IEEE.

[51] B. A. Shadwick and J. S. Wurtele. "Numerical Studies of Wake Excitation in Plasma Channels". In *Proceedings of the European Particle Accelerator Conference*, pages 827–829, Bristol, 1998. IOP.

[52] A. Chao. *Physics of Collective Beam Instabilities in High Energy Accelerators.* Wiley, 1993.

[53] Y. Y. Lau. "Classification of Beam Breakup Instabilities in Linear Accelerators". *Phys. Rev. Lett.*, 63(11):1141–1144, 1989.

[54] G. Arfken. *Mathematical Methods for Physicists.* Academic Press, 1985.

[55] G. A. Loew and J. W. Wang. "Minimizing the energy spread within a single bunch by shaping its charge distribution". *IEEE Trans. Nucl. Sci.*, NS-32(5):3228–3230, 1985.

[56] K. A. Thompson and R. D. Ruth. "Controlling transverse multibunch instabilities in linacs of high-energy linear colliders". *Phys. Rev. D*, 41(3):964–977, 1990.

[57] D. G. Colombant and Y. Y. Lau. "Effects of frequency spreads on beam breakup instabilities in linear accelerators". *Appl. Phys. Lett.*, 55(1):27–29, 1989.

[58] N. M. Kroll, R. M. Jones, C. Adolphsen, K. L. F. Bane, W. R. Fowkes, K. Ko, R. H. Miller, R. D. Ruth, M. Seidel, and J. W. Wang. "Recent Results & Plans for the Future on SLAC Damped Detuned Structures (DDS)". In *Advanced Accelerator Concepts: Seventh Workshop*, pages 455–464, New York, 1996. AIP.

[59] P. Kung, H.-C. Lihn, H. Wiedemann, and D. Bocek. "Generation and measurement of 50-fs(rms) electron pulses". *Phys. Rev. Lett.*, 73(7):967–970, 1994.

[60] B. E. Carlsten and S. J. Russel. "Subpicosecond compression of 0.1-1 nc electron bunches with a magnetic chicane at 8 MeV". *Phys. Rev. E*, 53(3):R2072–R2075, 1996.

[61] X. J. Wang, X. Qui, and I. Ben-Zvi. "Experimental observation of high-brightness microbunching in a photocathode rf electron gun". *Phys. Rev. E*, 54(4):R3121–R3124, 1996.

[62] D. Umstadter, J. K. Kim, and E. Dodd. "Laser Injection of Ultrashourt Electron Pulses into Wakefield Plasma Waves". *Phys. Rev. Lett.*, 76(12):2073–2076, 1996.

[63] E. Esarey, R. F. Hubbard, W. P. Leemans, A. Ting, and P. Sprangle. "Electron Injection into Plasma Wake Fields by Colliding Laser Pulses". *Phys. Rev. Lett.*, 79(14):2682–2685, 1997.

[64] R. G. Hemker, K.-C. Tzeng, W. B. Mori, C. E. Clayton, and T. Katsouleas. "Computer simulation of cathodeless, high-brightness electron-beam production by multiple laser beams in plasmas". *Phys. Rev. E*, 57(5):5920–5928, 1998.

[65] C. B. Schroeder, P. B. Lee, J. S. Wurtele, E. Esarey, and W. P. Leemans. "Generation of ultrashort electron bunches by colliding laser pulses". *Phys. Rev. E*, 59(5):6037–6047, 1999.

[66] E. Esarey, C. B. Schroeder, W. P. Leemans, and B. Hafizi. "Laser-induced electron trapping in plasma-based accelerators". *Phys. Plasmas*, 6(5):2262–2268, 1999.

[67] E. Esarey, B. Hafizi, R. Hubbard, and A. Ting. "Trapping and Acceleration in Self-Modulated Laser Wakefields". *Phys. Rev. Lett.*, 80(25):5552–5555, 1998.

[68] C. I. Moore, A. Ting, K. Krushelnick, E. Esarey, H. F. Hubbard, B. Hafizi, H. R. Burris, C. Manka, and P. Sprangle. "Electron Trapping in Self-Modulated Laser Wakefields by Raman Backscatter". *Phys. Rev. Lett.*, 79(20):3909–3912, 1997.

[69] P. Bertrand, A. Ghizzo, S. J. Karttunen, T. J. H. Pättikangas amd R. R. E. Salomaa, and M. Shoucri. "Two-stage electron acceleration by simultaneous stimulated Raman backward and forward scattering". *Phys. Plasmas*, 2(8):3115–3129, 1995.

[70] A. Yariv. *Quantum Electronics.* Wiley, 1989.

[71] W. H. Press, B. P. Flannery, S. A. Teukolsky, and W. R. Vetterling. *Numerical Recipes: The Art of Scientific Computing.* Cambridge University Press, 1986..

[72] E. P. Lee and R. K. Cooper. "General envelope equation of cylindrically symmetric charged-particle beams". *Part. Accel.*, 7(2):83–95, 1976.

[73] T. Katsouleas, S. Wilks, P. Chen, J. M. Dawson, and J. J. Su. "Beam Loading in Plasma Accelerators". *Part. Accel.*, 22(1):81–99, 1987.

[74] E. Esarey, A. Ting, P. Sprangle, D. Umstadter, and X. Liu. "Nonlinear Analysis of Relativistic Harmonic Generation by Intense Lasers in Plasmas". *IEEE Trans. Plasma Sci.*, PS-21(1):95–104, 1993.

[75] H. M. Milchberg, C. G. Durfee III, and T. J. McIlrath. "High-order frequency conversion in the plasma waveguide". *Phys. Rev. Lett.*, 75(13):2494–2497, 1995.

[76] D. C. Eder, P. Amendt, L. B. DaSilva, R. A. London, B. J. MacGowan, D. L. Matthews, B. M. Penetrante, M. D. Rosen, S. C. Wilks, T. D. Donnelly, R. W. Falcone, and G. L. Strobel. "Tabletop x-ray lasers". *Phys. Plasmas*, 1(5):1744–1752, 1994.

[77] B. E. Lemoff, G. Y. Yin, C. L. Gordon III, C. P. J. Barty, and S. E. Harris. "Demonstration of a 10-Hz, femtosecond-pulse-driven XUV laser at 41.8 nm in Xe IX". *Phys. Rev. Lett.*, 74(9):1574–1577, 1995.

[78] M. Tabak, J. Hammer, M. E. Glinsky, W. L. Kruer, S. C. Wilds, J. Woodworth, E. M. Campbell, M. C. Perry, and R. J. Mason. "Ignition and high gain with ultrapowerful lasers". *Phys. Plasmas*, 1(5):1626–1634, 1994.

[79] E. Esarey, J. Krall, and P. Sprangle. "Envelope analysis of intense laser pulse self-modulation in plasmas". *Phys. Rev. Lett.*, 72(18):2887–2890, 1994.

[80] G. Shvets and J. S. Wurtele. "Instabilities of Short-Pulse Laser Propagation through Plasma Channels". *Phys. Rev. Lett.*, 73(26):3540–3543, 1994.

[81] E. Esarey and W. P. Leemans. "Nonparaxial propagation of ultrashort pulses in plasma channels". *Phys. Rev. E*, 59(1):1082–1095, 1999.

[82] P. Sprangle, A. Ting, and C. M. Tang. "Analysis of radiation focusing and steering in the free-electron laser by use of a source-dependent expansion technique". *Phys. Rev. A*, 36(6):2773–2781, 1987.

[83] P. E. Young and P. R. Bolton. "Propagation of Subpicosecond Laser Pulses through a Fully Ionized Plasma". *Phys. Rev. Lett.*, 77(22):4556–4559, 1996.

[84] T. W. Johnston, F. Vidal, and D. Fréchette. "Laser-plasma filamentation and the spatially periodic nonlinear schrödinger equation approximation". *Phys. Plasmas*, 4(5):1582–1588, 1997.

[85] C. D. Decker, W. B. Mori, T. Katsouleas, and D. E. Hinkel. "Spatial temporal theory of Raman forward scattering". *Phys. Plasmas*, 3(4):1360–1372, 1996.

[86] N. E. Andreev, V. I. Kirsanov, and L. M. Gorbunov. "Stimulated processes and self-modulation of a short intense laser pulse in the laser wake-field accelerator". *Phys. Plasmas*, 2(6):2573–2582, 1995.

[87] L. Gorbunov, P. Mora, and T. M. Antonsen. "Magnetic field of a plasma wake driven by a laser pulse". *Phys. Rev. Lett.*, 76(14):2495–2498, 1996.

[88] W. P. Leemans, P. Volfbeyn, K.-Z. Guo, S. Chattopadhyay, C. B. Schroeder, B. A. Shadwick, P. B. Lee, J. S. Wurtele, and E. Esarey. "Laser-driven plasma-based accelerators: Wakefield excitation, channel guiding, and laser triggered particle injection". *Phys. Plasmas*, 5(5):1615–1623, 1998.

[89] W. P. Leemans, C. B. Schroeder, P. B. Lee, J. S. Wurtele, and E. Esarey. "Ultrashort x-ray pulse generation using laser driven accelerators". In *Time*

Structure of X-Ray Sources and Its Applications, volume 3451, pages 41–51. SPIE, 1998.

ERNEST ORLANDO LAWRENCE BERKELEY NATIONAL LABORATORY
ONE CYCLOTRON ROAD | BERKELEY, CALIFORNIA 94720

Prepared for the U.S. Department of Energy under Contract No. DE-AC03-76SF00098